UNIVERSITA' DEGLI STUDI DI PADOVA

Dipartimento di Ingegneria Industriale DII

Corso di Laurea Magistrale in Ingegneria Energetica

CFD Chord Analysis In Diffuser Augmented Wind Turbines

Relatore

Prof. Giorgio Pavesi

Studente

Alberto Claudio Alvisi

Matricola 1159868

Anno Accademico 2021/2022

Ai miei genitori

Ignoranti quem portum petat nullus suus ventus est

Non esiste vento favorevole per il marinaio che non sa dove andare

[Lucio Anneo Seneca]

οἷον οἰκοδομοῦντες οἰκοδόμοι γίνονται καὶ κιθαρίζοντες κιθαρισταί

Per esempio, si diventa costruttori costruendo, e citaredi suonando la cedra.

[Aristotele]

Figure 0.1: Van Gogh(1889),*Notte Stellata*

Mediante valutazioni matematiche, si è notato come gli schemi luminosi del dipinto seguano curiosamente dinamiche analoghe ai vortici nei moti turbolenti, sebbene Van Gogh non avesse alcuna nozione in merito.[1]

[1]Aragón, J. L., Naumis, G. G., Bai, M., Torres, M., & Maini, P. K. (2008). Turbulent luminance in impassioned van Gogh paintings. Journal of Mathematical Imaging and Vision, 30(3), 275-283.

Contents

List of Figures

iii

List of Tables

x

Chapter 1

Introduction

A research field that has been strongly developed during the 1980s is the diffuser-augmented wind turbines because of expectations of enhancing over traditional open turbines. The principle behind the ducted turbine is very simple and was already proposed at the dawn of wind technology development at the beginning of the twentieth century. A diffuser wraps all the rotor and creates a depression immediately behind the blades thanks to a shape that has a converging inlet and diverging outlet. The depression requires an acceleration of the flow that crosses the machine, generating more power possible. Obviously, several ways, able to create the back-pressure, have been proposed since the idea was initially proposed by Betz[1] himself. Although the concept is really simple, its optimisation could quickly become quite complicated until an analytic theory of the motion generated by the diffuser is not fully elaborated. Indeed, the diffuser presence perturbs the wind profile in a manner that it is not more possible to apply the same optimization procedure used for bare turbine. Furthermore, since the early researches the DAWT developed has faced another problem: the diffuser requires more raw material respecting the same bare alternatives. Indeed, it can be immediately clear that a framework that has to cover all the blades can not be light and without having structural weaknesses. Moreover, since the 90s the wind sector has decided to go towards turbines with blades bigger and bigger as increasing radius is a method to rise the power production. Consequently, interest in shrouded turbines has been increasingly given to fading up to the recent years. Indeed, even if the ducted turbines can not be implemented in the larger machines, they have their greater advantages for the small and medium power size. Just the dimension that has been recently prominent as the necessity of having a standalone electric supply, often connected to a storage, is rising, e.g. charging electric device. In this perspective, the current work intends to illustrate

---

[1]Albert Betz (1885 - 1968), German physicist known for being one of pioneers in the wind technology

which kind of solution can be adopted to optimise the blade shape for diffuser-augmented turbines. In fact, the lack of improvement for the ducted turbine can also be explained by the fact that there is usually no dedicated design process. In fact, the coupled between diffuser and blades happens without designing the profile taking into account the diffuser effect on motion. Or rather, the blade profile is already fixes and only the diffuser shape is designed in accordance with. The aim of this work is to illustrated which could be the best equation able to provide the optimal twist angle and chord. After providing arguments in favour of Maalawi's formulation, two different blade profiles are generated using GUI BEM software, developed by Padova University. In one case the design velocity will be chosen as usual without considering the coupled diffuser. In the other case, an augmentation of design velocity is proposal following the logic that it is the augmented velocity what the blade really see.

As well as comparing results each other, a comparisons with commercial bare turbines, actually on the marked, is proposed.

The computational work has also required to increase the number of nodes, and therefore its complexity to achieve a worthwhile outcome.

After this preliminary **Ch.1**, **Ch.2** unfolds a brief overview about Earth's atmosphere is presented as a basis for illustrating the opportunities for the wind sector, also in view of the European path toward 2050 targets and the current energy crisis.

The **Ch.3** addresses the theories that describe the aerodynamic of wind turbine: open and ducted. Finally, an optimisation algorithm for shrouded turbine is proposed. In additional, a table of different formulations for the chord length is harvest with a necessary comparison.

The computational work starts in **Ch.4**. As first step, the design procedure is explained. Secondly, the procedure to simulate is described step-by-step. Finally, a critical comparison is proposed.

In the last **Ch.5** illustrates the conclusions of this thesis.

Chapter 2

Wind Sector in Europe

2.1   Why Winds Blow?

Briefly, the circulation of Earth's atmosphere is similar to the dynamics of a fluid subjected to a spinning system and deferentially heated due to its tilting. Obviously, the main energy source comes from the Sun, which emits constantly radiative energy as it was a blackbody with superficial temperature at 6000 K. The Earth, that absorbs much of the incident energy, has a radiative equilibrium temperature, that keeps it warms up and allows to emits radiative energy towards space at the same rate it is received.

The solar power incident on the Earth depends by the constant incoming solar flux[1], $S_0 = 1367 W m^{-2}$, and the cross-sectional area of the Earth intercepted, πR_E^2 [2] and is equal to $S_0 \pi a^2 = 1.74 \times 10^{17}$ W.

As our experience can confirm, only a significant fraction of the incoming energy is absorbed by the Earth, while the left part is naturally reflected thanks to *albedo*, α. The albedo is the ratio between the incoming energy and the amount reflected toward space and varies in relation of the clouds, the type of ground (desert, ice, snow, etc.), but the average value, called *planetary albedo*, is $\alpha_p \simeq 0.30$. Therefore, the solar radiation absorbed by the Earth is $(1 - \alpha_p) S_0 \pi R_E^2 = 1.22 \times 10^{17}$ W.

The Earth absorbs the majority of residual energy and remits at different wavelengths[3]. The atmosphere handles the left part via thermals(conduction and convection) and latent heat. The small residual difference, 0.9 W/m^2, is the net absorbed and causes the global warming effect.

---

[1]In a more precise form, the solar energy flux is not properly constant, but is also correlated to sunspots contributions.

[2]R_E is the Earth's radius.

[3]The wavelengths is strongly dependent from temperature. Therefore, the incoming rays from the Sun have a shorter wavelengths due higher emission temperature, while the Earth emits mainly in the infrared (IR) spectrum

At the radiative equilibrium, the total energy flux radiated by the Earth to space and the total incoming flux by the Sun generates a temperature equilibrium on the Earth's atmosphere. It can be defined the T_e, *emission temperature*, as the temperature that the Earth would emitted outgoing if it had behaviour like a blackbody.

Actually,

$$T_e = \left[\frac{(1 - \alpha_p)S_0}{4\sigma} \right]^{1/4} = 255 \text{ K} \tag{2.1}$$

is considerably below the globally averaged surface temperature, $T_s = 288K$, measured by the instruments. The difference is explained thanks to the presence of greenhouse gases in the atmosphere that have an absorption spectrum close to 255K and so they are able to keep the energy inside the atmosphere. Indeed, a great amount of IR radiation emitted by the ground is absorbed during its passage trough the atmosphere. Unfortunately, the resulting radiative emission from the atmosphere is direct not only spaceward, but also groundward,adding to solar radiation. On one side, this is a positive help for the life on Earth, providing the presence of water at liquid phase on the surface. On the other side, the increase of anthropogenic emissions of greenhouse gases, mainly CO_2, during the last centuries, especially after World War II, has started to yield a warmer world, as well as humanity, has not never seen in the last 12'000 years, and in addition, happened over a short period of time. The shortest time affected by temperature rise is a proof for the anthropogenic origin of global warming because it is generally recognised by the scientific community that no natural forces could be able to change the global temperature so quickly. The atmosphere is the pressurised fluid capable of transferring the heat differences all around the globe. Our atmosphere is conventionally divided into four layers: the lower one is *troposphere*, that contains the 85% of atmosphere mass and almost the entire amount of water vapor, owned to the Clausius-Clapeyron relation[4]. The lower region of troposphere, from the surface up to 1 km, is called atmospheric boundary layer (ABL) and is ruled by turbulence motion. The boundary between the troposphere and the upper layer,*stratosphere*, is the tropopause, generally at the altitude of $8 - 16$ Km, depending on latitude and season. Above stratosphere there are two more layers before free space: *mesosphere* and *thermosphere*.

Convection

The convection happens when a fluid, like air in a free atmosphere, starts an overturning motion if it is warmed from below (or cooled from above). The Fig.2.1represents a sketch of atmosphere where the emission temperature in the atmosphere is lower than the surface temperature because the layer close the ground receives, besides the solar radiation, the downwelling IR radiation from the layers above. The overturning motion starts because the heated air is lighter and moves vertically upward. As the air becomes heavier while it rises, the gravitational forces acts to complete the circular motions. Convection has a key role in the troposphere equilibrium because it balances the troposphere radiative energy budget, proposed by Syukuro Manabe. Indeed, $T(z)$ is an idealized radiative equilibrium temperature profile, that is the theoretic temperature in atmosphere where the thermal radiation incoming is balanced with outcoming part. The Earth's radiative-convective transfer model, published in the 1967 paper 'Thermal Equilibrium of the Atmosphere with a Given Distribution of Relative Humidity'[5] has become the common based for modeling the atmosphere circulation: it solves the energy balance inside the global atmosphere taking into consideration the radiative and convection contributions.
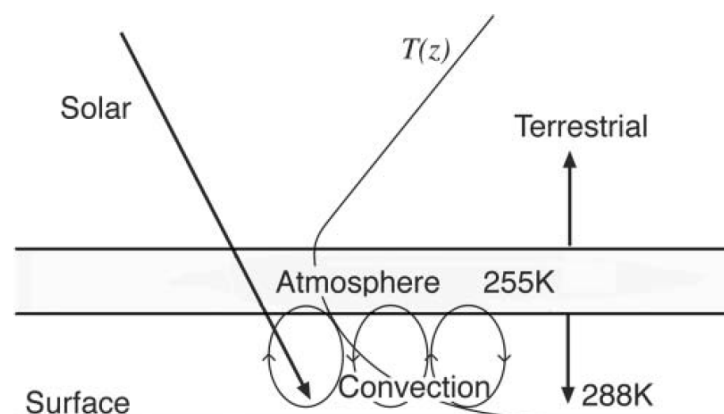
Figure 2.1: Sketch of warming process on surface and the following air mixing owing to convection contribution. Source:(Marshall and Plumb2008)
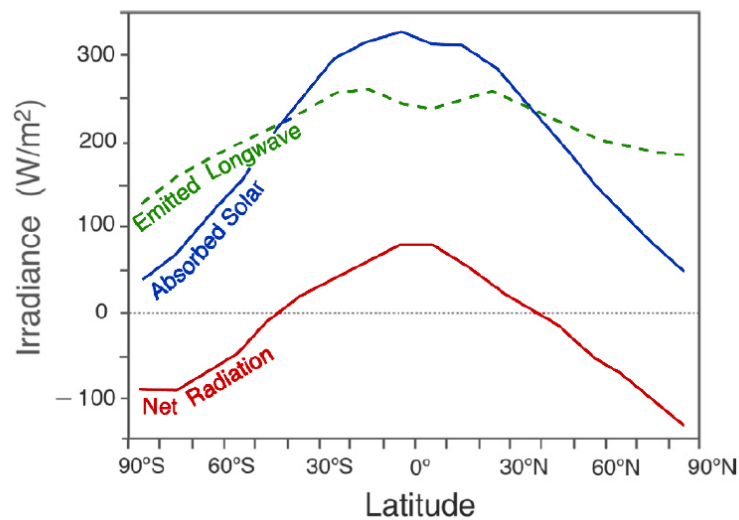
Figure 2.2: Net Radiation respect latitudes. Source:Marshall and Plumb(2008)

The Energy Balance of the Atmosphere

The Fig.2.2shows the net radiative budget through the latitudes and gives
an intuitive cue about the reason behind air movements in the troposphere and,
therefore, the winds. The net radiative is the difference between the emitted
longwave radiation in the IR spectrum and the absorbed solar radiation. The plot
of net radiative suggests a negative contribution in the high latitudes (the poles)
balanced by a positive contribution in the equator area. The areas where the net
radiative has a negative sign (approximately from the poles up to 40° N (40° S) is
equal to the area with positive sign of net radiative. This cannot be seen immedi-
ately because the area covered by pole regions are substantially smaller than the
equator zone. The difference in energy input is owing to Earth's tilting, which
reduces the amount of energy in the poles during the year[6]. Consequently, the
gradients in temperature and pressure among the latitudes must be compensated
by the natural flux inside the atmosphere and the oceans. ERBE[7] can provide an
account of this poleward energy transport shown in Fig.2.3aand computed by the

---

[4]Indeed, the relation shows that the saturation vapor pressure is a function of the temperature.
Consequently, the moisture concentration is higher on the lower layers of atmosphere in corre-
spondence of higher temperatures and decreases exponentially with the temperature reduction
due to the height

[5]Syukuro Manabe received the 2021 Nobel Prize in Physic together with the German oceanog-
rapher Klaus Hasselmann 'for the physical modelling of Earth's climate, quantifying variability
and reliably predicting global warming' (official assessment of Nobel Prize).

[6]Currently, the Earth has a tilted axis of 23.5°, pointed in the direction of the North Stars

[7]Earth Radiation Budget Experiment (ERBE) was a 90s NASA project dedicated to valuate the
energy exchange between the Sun, the Earth and the space using three different satellites.

equation[8]:

$$ET(\varphi) = \int_{-\pi/2}^{\varphi} \int_{0}^{2\pi} \left[(1 - \alpha)E_{sun}(\lambda, \varphi) - E_{IR\uparrow}(\lambda, \varphi) \right] R_E^2 \cos(\varphi) d\lambda d\varphi \qquad (2.2)$$

(a)
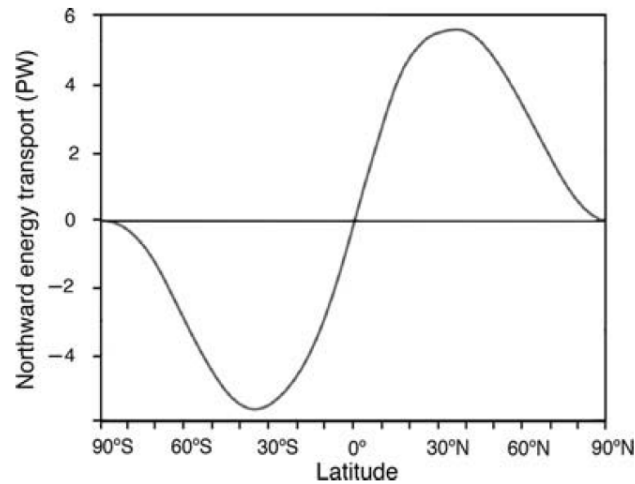
(b)
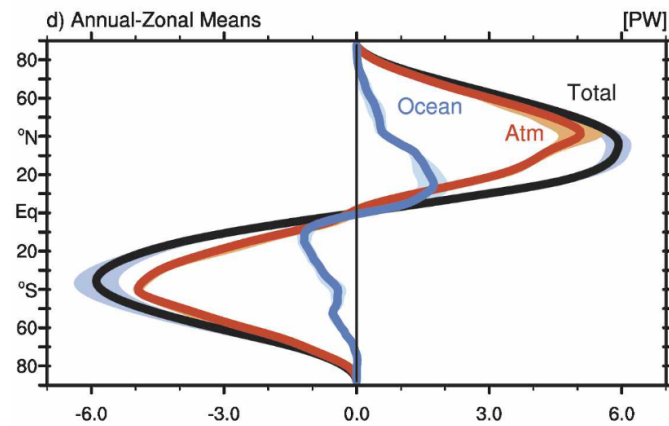
Figure 2.3: (a) 'The northward energy transport deduced by the top of atmosphere measurements of incoming and outgoing solar and terrestrial radiation from the ERBE satellite. The units are in $PW = 10^{15} W$'. Source:Marshall and Plumb(2008). (b)The energy transport split in atmosphere and ocean carrier. Source:(Fasullo and Trenberth 2008))

The necessary energy transport is mediated by the atmosphere and also by the significant contribution of oceans, as the Fig.2.3bindicates. Before going into

---

[8]where λ is the latitude, φ the longitude, R_E the Earth's radius, $(1 - \alpha)E_{sun}$ the incoming radiation and $E_{IR\uparrow}$ the outgoing radiation. The equation integrates radiative difference over the entire globe between the South Pole and latitude λ.

details about how the energy is transferred in the atmosphere and, therefore, the wind circulation, it is useful to recap few basic concepts.

Atmospheric Stability

The hydrostatic balance is the relationship between pressure and density and rules the vertical motion in the free atmosphere.
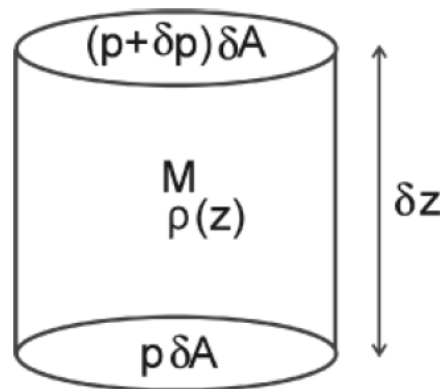
Figure 2.4: Undisturbed vertical air column

Given a vertical column of air, as in Fig.2.4, where the mass M is the result of density $\rho \times \delta A$ (cross-sectional area) $\times \delta z$ (height). It is clear that, in case of unaccelerated air column without others forces except gravity, the vertical forces are (positive sign is upward) if p the pressure on the lower layer, $p + \delta p$ the pressure on the upper layer and δp the change in pressure moving from z to $z + \delta z$, assuming a small δz increment:

- Gravitational force
  $F_G = -gM = -g\rho\delta A\delta$
- Pressure force on the top
  $F_T = -(p + \delta p)\delta A$
- Pressure force on the bottom
  $F_B = p\delta A$

As $F_G + F_T + F_B = 0$ and also $\delta p + g\rho\delta z = 0$, hence:

$$\frac{\partial p}{\partial z} + g\rho = 0 \tag{2.3}$$

To apply Eq.(2.3), the equation of state gives the necessary link between p and ρ to determinate the function $p(z)$ from $\rho(z)$:

$$\frac{\partial p}{\partial z} = -\frac{gp}{RT} \tag{2.4}$$

Even if all of us have a strong familiarity with the concept of temperature, it is not the favourite one in atmospheric science because the temperature does not conserve during adiabatic displacement. Indeed, for example, if an air parcel moves downward adiabatically[9], the temperature increases due to 1st law of thermodynamics[10] Hence, it is useful to speak in terms of *potential temperature*, which is conserved under adiabatic displacement.

$$\theta = T \left(\frac{p_0}{p} \right)^{k} \tag{2.5}$$

where p_0 is the reference pressure, estimated at 1000 $mbar$. In accordance with Eq.(2.5) under adiabatic displacement, it yields:

$$\frac{d\theta}{\theta} = \frac{dT}{T} - k\frac{dp}{p} = 0 \tag{2.6}$$

The Fig. **??** shows that Atmosphere Boundary Layer (ABL)[11] has three different situations, which are defined by the ratio between potential temperature and height. Furthermore, the ABL tends to have a cycle dominated by seasonal conditions.

- **Stable ABL**, that valids if $\frac{\partial\theta}{\partial z} > 0$, occurs in an environment where, if an air parcel ascends upwards, it becomes cooler than the surrounding environment. Therefore, the air parcel is relatively heavier and starts a descending motion due to gravity effect. As the vertical motions are suppressed by buoyancy effect, the atmosphere is stable. This happens foremost in the summer season, where the colder air - higher density, so heavier - is underneath warmer air - lower density, so lighter[12]. Otherwise, one can mention that air with lower potential temperature is underneath air with higher potential temperature.

- **Neutral ABL**, that valids if $\frac{\partial\theta}{\partial z} = 0$, means that if an air parcel ascends upwards keeps the same temperature as its environment. The ascending speed remains constant as long as the air parcel is neutral respect the environment.

- **Unstable ABL**, that valids if $\frac{\partial\theta}{\partial z} < 0$, occurs if an air parcel in ascending motion is pushed further and accelerates as the parcel is surrounded by cooler environments. In this situation, vertical motions are enhanced by

---

[9]The energy is not exchanged with the ambient

[10]As $\delta Q = \delta W + \delta E$ and $\delta Q = 0$, the result of variation in work means a change in energy and therefore in temperature.

[11]In opposition of the other layers, ABL is that part of atmosphere, thick from few meters up to several km in accordance with meteorologic conditions, that directly feels the effect of the Earth's surface and is dominated by the turbulence.

[12]The colder (warmer) air are to be intended in comparative terms.

buoyancy effect. An unstable stratum occurs when warmer air - lower density, so lighter - is underneath colder air - higher density, so heavier. Otherwise, one can mention that air with higher potential temperature is underneath air with lower potential temperature. The unstable ABL is typical during winter seasons.

Geopotential Height

Clearly, the difference in solar radiation among latitudes yields a gradient in air temperature, which means a gradient in height because warmer air occupies more space than colder air. Consequently, it is convenient to use the pressure for measuring the height instead of vice versa. Speaking in term of vertical coordinate $z(p)$, it is equal to think as the height of a pressure surface, defined by the function[13]:

$$z(p) = R_d \int_p^{p_s} \frac{T}{g} \frac{dp}{p} \tag{2.7}$$

Eq. (2.7) defines the *geopotential height* of a surface respect the reference value at p_s, considering $z(p_s) = 0$. The geopotential isolines are lines with constant geopotential height, that draws imaginary pressure surface on the troposphere where is kept constant the same value of pressure respect the reference pressure at sea level.

Geostrophic Wind

In case of rotating body,like the Earth can be assumed, the motion of a fluid parcel[14] in atmosphere follows the equation:

$$\frac{D\mathbf{u}}{Dt} + \frac{1}{\rho}\nabla p + \nabla \phi = -2\Omega \times \mathbf{u} + F \tag{2.8}$$

where:

- $\frac{D\mathbf{u}}{Dt}$ is the total derivative over time of velocity vector $\mathbf{u} = (u, v, w)$ along the direction (x, y, z);
- $\frac{1}{\rho}\nabla p$ is the pressure gradient;
- $\nabla \phi$ is the gravitational potential combined with the centrifugal accelerations in a rotating frame: $\phi = gz - \frac{\Omega^2 r^2}{2}$;
- $-2\Omega \times \mathbf{u}$ is the Coriolis acceleration as the result of the common experience of feeling an acceleration directed rightwards of velocity vector when a parcel is moving in a rotating frame. The Coriolis force is defined by the Coriolis

---

[13]Where $z(p_s) = 0$ by definition and R_d is the ideal gas constant
[14]The viscosity is neglected to simplicity

parameter $f = 2\Omega sin(\varphi)$, which varies with the latitude. Following the sinus function, it is null at the equator and maximum at the poles;

- F is the frictional force per unit of mass.

In the free atmosphere with large-scale motion, Eq.(2.8) may be rewritten as a balance between pressure gradient and Coriolis term:

$$f\hat{\mathbf{z}} \times \mathbf{u} = -\frac{1}{\rho}\nabla p \qquad (2.9)$$

The Eq.(2.9) represents the motion of wind if the Coriolis force is correctly balanced by the gradient of pressure. In this circumstance, the wind speed becomes:

$$\mathbf{u}_g = \frac{1}{f\rho}\hat{\mathbf{z}} \times \nabla p \qquad (2.10)$$

By Fig.2.5, you can see how this balance can develop around a centre of low (high) pressure. The wind direction is normal to pressure gradient as the result that the Coriolis force is balanced by the pressure gradient force in the opposite site.
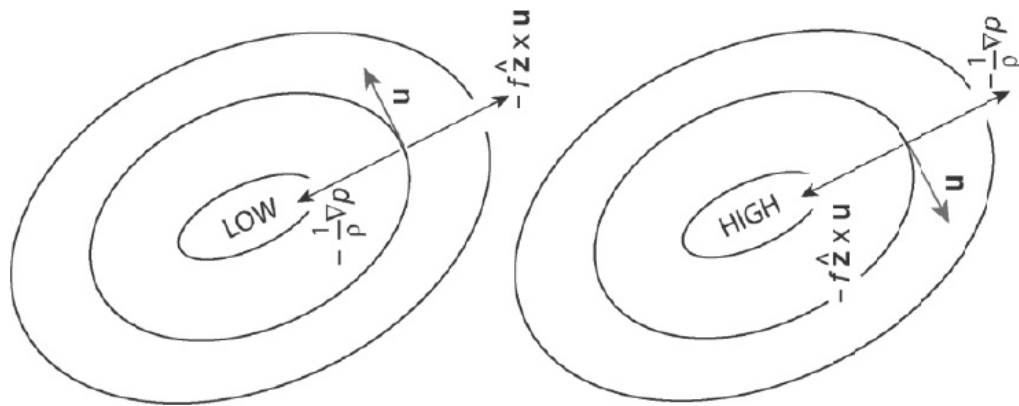
Figure 2.5: Geostrophic winds motion. Source:(Marshall and Plumb2008)

Barotropic Stability and Baroclinic Instability

In the tropics, usually the atmosphere faces a *barotropic stability*, namely the potential temperature θ isolines does not cross the geopotential isolines: a configuration where the energy of the system is at the lowest level. In the midlatitudes[15], the atmosphere suits a *baroclinic instability*, namely the potential temperature θ

---

[15]The midlatitudes, that are settled between 30°-60° N (S) and also correspond to the Europe latitudes, have meteorological conditions, particularly well tailored for wind energy production.

isolines cross the geopotential isolines: a configuration where the energy of the system is not at the lowest level and therefore regularly the atmosphere pushes to move itself toward a barotropic situation.[16] In the midlatitudes, the natural shift towards barotropic stability is opposed by two independent factors which are not present in tropic regions:

- A stronger Coriolis force that curbs the circulation between latitudes.
- In the north (south) hemisphere, the equator acts as well as a hot source that transports continuously warmer air from the south (north) side, while the pole acts as well as a cold source moving continuously colder air from the north (south) side.

Hadley Circulation

In the region where the barotropic stability is present, e.g. in the tropics, the main wind thrust is the gradient pressure from a higher-pressure spot to one with lower pressure. The gradient difference acts horizontally and also vertically. On the Equator, the air is warmer than on the Poles. Consequently, the column of air at the Pole has a lower height respect the column at same pressure, placed at the Equator, generating a tilting on the pressure surface between the Pole and the Equator.

Looking at the sketch in Fig.2.6, in a tropical region, the layers of the atmosphere occupy more vertical space because they are warmer with respect to pole layers, which are colder and, thereby, denser. Therefore, the tilting is revolved by winds that moves the mass of air polewards. Also, the tilted pressure surfaces show that wind speed strength rises with altitude. Hadley [17] suggested that in a non-rotating Earth, air would be able to move directly from the equator to the poles, but we cannot observe this kind of circulation because of the Earth's rotation. Indeed, in a rotating Earth, the conservation of angular momentum ($L = I\Omega$) must be preserved. On the Equator, the angular rotation Ω is smaller because of the Earth's radius, R, and thereby the moment of inertia, I, has a greater weight. Moving polewards, R decreases and consequently, Ω rises. In accordance with the Fig.2.7, in an idealized Hadley cell, the air has to accelerate westerly [18] to conserve the angular momentum.

The acceleration on a rotating frame generates a Coriolis force, which becomes

---

[16](Marshall and Plumb2008) uses this concept to summarise :"In a 'baroclinic" fluid, $\rho = \rho(p, T)$, there can be gradients of density (and therefore of temperature) along pressure surfaces. This should be contrasted to a 'barotropic' fluid [$\rho = \rho(p)$] in which no such gradients exist

[17]George Hadley (1685-1768) was a British lawyer and an amateur meteorologist. In 1735, he was the first to introduce a general model of atmospheric circulation.

[18]More precisely, the acceleration has the same direction of Earth's spin rotation.h westerly is the same rotation direction, whereby the Earth rotates.
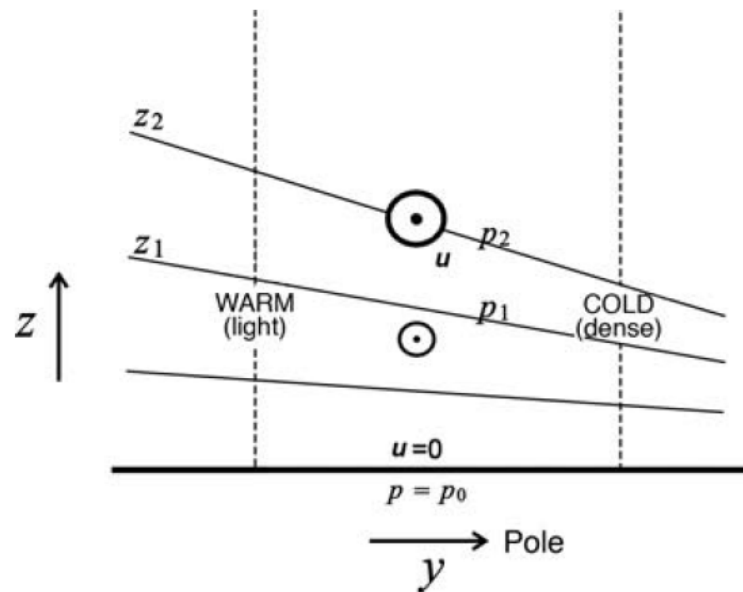
Figure 2.6: The pressure surface are tilted towards the poles; indeed,. Source: (Marshall and Plumb2008)
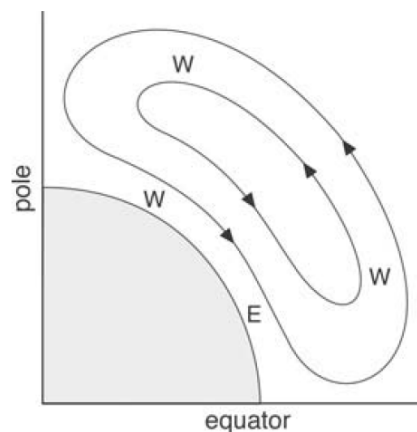
Figure 2.7: The Hadley circulation straight from equator to pole in one giant cell. (W) and (E) marks the hypothetical region with westerly and easterly winds. Source: (Marshall and Plumb2008)

greater as the air moves away from the equator: the Coriolis force can be seen as a barrier for the Hadley circulation that needs to close the loop near to 23°-25° of latitudes in South and North directions.

In fig.2.8, the air circulation in the tropical and subtropical regions is sketched. Above the equator, the strong radiation warms the air that moves upward due to convection up to the tropopause. The air starts to move poleward and lose energy due to radiation. At the same time, the air moves westerly to conserve the angular momentum. Due to Coriolis forces, the air starts a downwilling movement in the

subtropics. After that, the easterly winds[19] at a lower altitude close the cell.
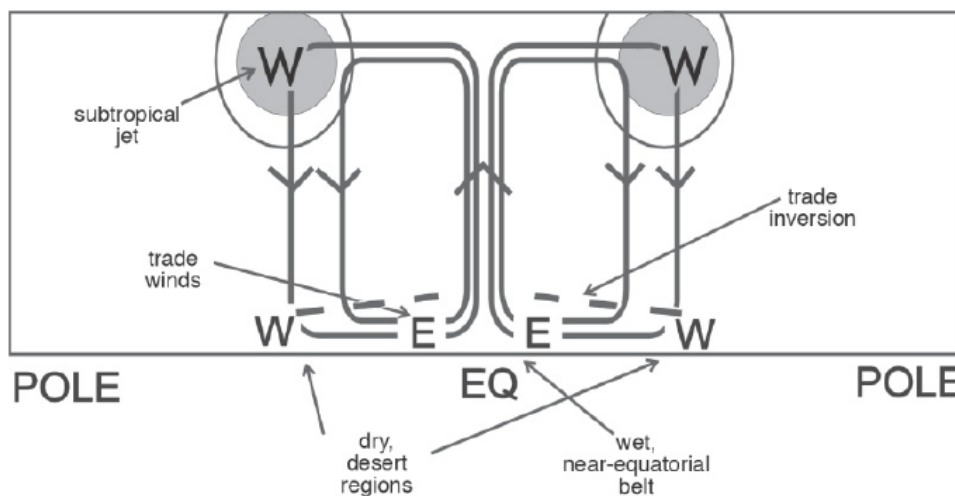
Figure 2.8: General air movement above the tropics region. Source: (Marshall and Plumb 2008)

In Fig.2.9a Python plot is illustrated: the meridional [20] cross-section of annual average overturning circulation The red (blue) circulation over the Equator in the North Hemisphere (South Hemisphere) describes the Hadley cell. The cell on its right (left) side of the red (blue) Hadley cell is named Ferrel cell: its scope is to complete the circulation at the mid-latitudes, compensating the movement of the Hadley cell.[21]

Eddies

After describing the wind circulation in the tropics, the attention is to illustrate how the heat surplus is finally exchanged from the mid-latitudes to the poles, where a heat deficit is collocated and the baroclinic instability is presented. In the midlatitudes, the Hadley circulation does not work anymore due to Coriolis's effect, while at the same time, the necessity to transport energy polewards keeps being relevant. The natural solution is the eddies generation. Eddies are are extremely strong in the midlatitudes. The heat exchanged through eddies at midlatitudes is also enhanced by the Ferrell cell that works in opposition respect Handly cell, carrying heat to the equator.

The **eddies** are defined as 'fluid current whose flow direction differs from

---

[19]The easterly winds are usually called tradewinds because they have been helpful for the trade routes between Europe and North America since the modern age.

[20]A wind in northward (southward) direction from the equator.

[21]The necessity of Ferrel cell for closing the loop is more complex than expressed above. Briefly, the Ferrell cell is thermal indirect circulation that moves cold air from the poles equatorwards, balancing the thermal direct circulation provided by Hadley cells.
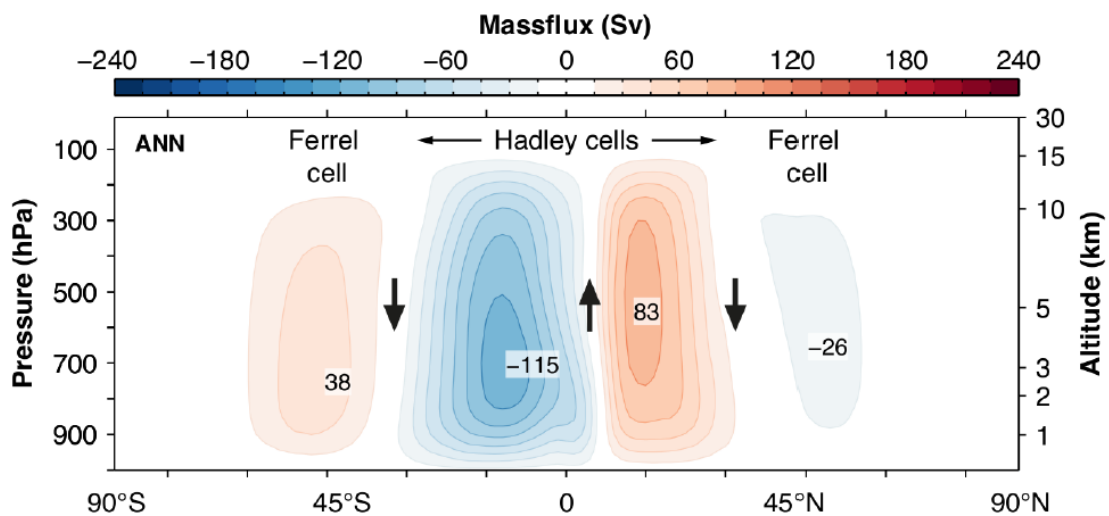
Figure 2.9: Air mass flux in Sverdrup [1 Sv = 1million m^3/s] respect South-North section. Source: Lectures of Physic of the Climate System of Prof. Fabien Maussion at the Innsbruck University.
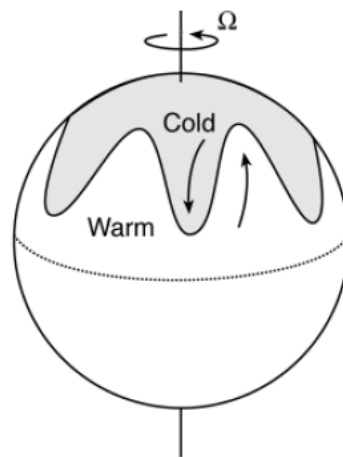
Figure 2.10: Eddies heat exchanged. This mean the presence of stronger wind at mid latitudes useful for wind energy production. Source:(Marshall and Plumb2008)

that of the general flow; the motion of the whole fluid is the net result of the movements of the eddies that compose it'.[22] The eddies are divided in:

- **Stationary eddies** are characterized by persistent zonal asymmetries in atmospheric variables, like Azores High or Icelandic Low.
- **Transient eddies or storms** are characterized by departures from the time mean flow at a particular location.

---

[22]https://www.britannica.com/science/eddy-fluid-mechanics

(a)

(b)
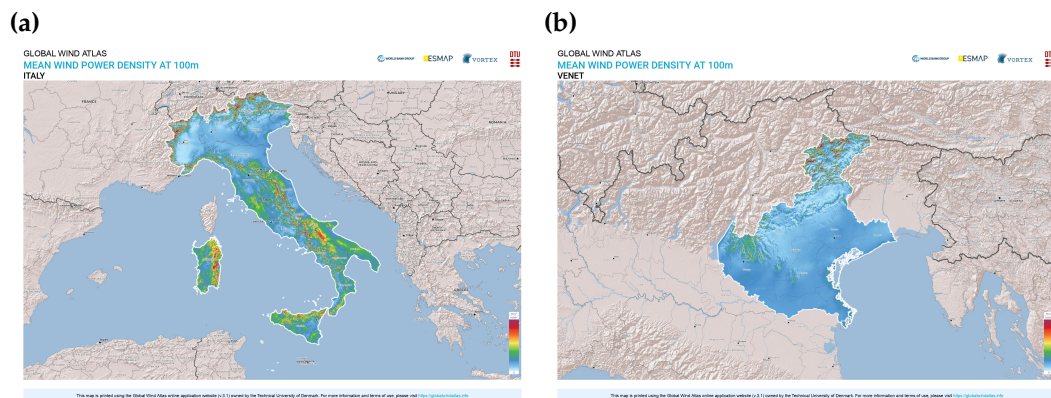
Figure 2.11: (a) Wind Power Density at 100m in Italy. (b)Wind Power Density at 100m in Veneto. Source: https://globalwindatlas.info/.

Wind Energy Available

This brief, and necessarily synthetic, presentation about Earth's atmospheric circulation can be helpful to understand why at the European latitudes, between 30°-60° N, there are very good and powerful locations for installing wind farms (offshore and onshore), e.g. North and Baltic Seas regions and the countries surroundings, thanks to the constant and persistent contributions of stationary and transient eddies. A lesser-known advantage for the offshore is that the sea surface is smoother compared to land surface where the friction from surface has a directly influence on wind turbulence, reducing the potentialities.

Regarding onshore, Italy has disadvantages owing to the Alps barrier, although there are still validated spots, mainly in Sardinia, in Sicily and along the Apennines hills, as Fig.2.11ashows: the *Mean Wind Power Density*[23] is overlapped to Italy boundaries.[24] In Veneto, Fig.2.11b, the situation is not optimal as a single glimpse can confirm, although there are relevant places in the alpine area thanks to valley winds. A valley wind blows along the axis of a valley. In upvalley direction during the daytime and in downvalley direction during the night. The main valley wind-driven is the pressure differences in the horizontal direction that arise from horizontal temperature differences between the atmosphere inside the valley and the layers over the nearby plains. The valley winds can be found sufficiently strong and steady during the year to be interesting for wind production.

---

[23]Mean wind power density (WPD) is an indicator about the wind energy available in one location and is the mean annual power available per square meter of swept area of a turbine, calculated for different heights above ground

[24]Paying attention to offshore wind turbine there are also relevant spots in the Adriatic in front of Emilia-Romagna cost or Puglia shoreline and also close to Sicily.
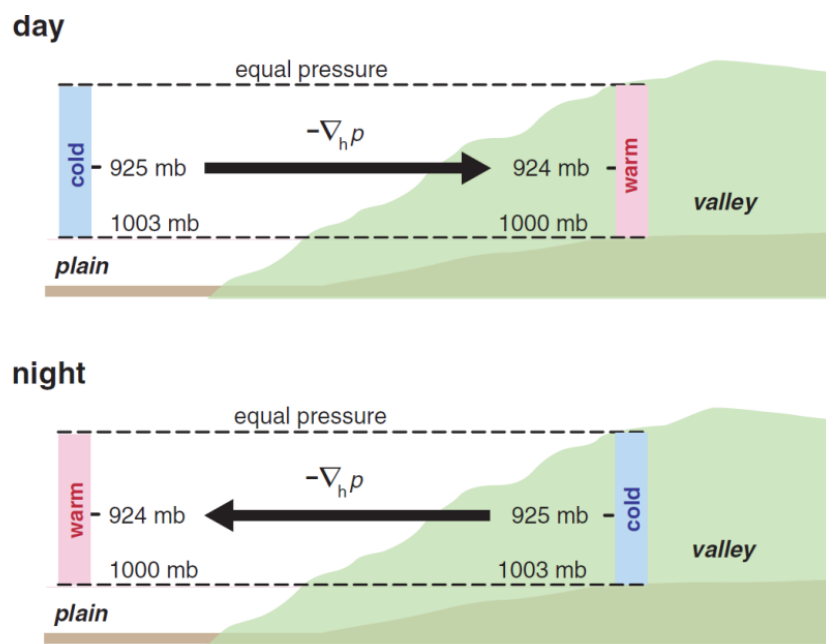
Figure 2.12: Illustration about valley winds driver in daytime (upvalley) and nightime (downvalley). Source:(Markowski and Richardson2010)

2.2 European Policy Concerning Climate Change

In December 2015, the COP[25] 21 reached the so-called Paris Agreement among 196 countries that pursues the goal of 'holding the increase in the global average temperature to well below 2° C above pre-industrial levels and pursuing efforts to limit the temperature increase to 1.5° C above pre-industrial levels, recognizing that this would significantly reduce the risks and impacts of climate change'.[26] In November 2018, aiming to achieve this goal, the European Union settled the 2050 Long Term Strategy that foresees the climate-neutrality by 2050 and announced to implement of an energy transition in the European economy with a constant reduction of fossil fuels in favour of renewable sources. The intermediate step for the European Commission within 2030 is settled to increase the target of CO_2 reduction, compared with the 1990 level, from 40% to 55% .[27] Simultaneously, the European Commission raised the renewable energy production target from 32% to $38 - 40\%$ according to the latest European Commission's Renewable Energy Directive. In the wind energy sector, this means an expansion up to $433 - 452$ GW of wind energy before 2030 from 172 GW in 2021. To put it in another way, the

---

[25]The Conference of the Parties are the annual meeting of the supreme making-decision body under the United Nations Framework Convention on Climate Change (UNFCCC), drafted in 1992 and signed by 154 states, that oversights all the process to combat 'dangerous human interference with the climate system', as its established treaty enunciates

[26]Art. 2 (b) of Paris Agreement to the United Nations Framework Convention on Climate Change, Dec. 12, 2015.

[27]The EU 2030 Climate & Energy Framework is also called 'fit for 55%'.

55% target means that the new wind installation should be at least equal to 27 GW annually: unfortunately, e.g. WindEurope[28] foresees that the wind installation will be only 15 GW per year in the period 2021-2025.

This narrow path cannot be only on the shoulders of the European Commission, but also the Members State have to collaborate through their national energy and climate plans following the Regulation on the Governance of the Energy Union and Climate Action (EU/2018/1999).

The EU Commission requires to settle the strategy for a span of 10 years with regular updates. Over the period 2020-2029, Italy needs to increase the wind capacity from 11 GW up to $40 - 50$ GW in accordance with its own plan. The wind power currently installed is close to 11 GW, which is obtained at 95% by 493 plants with a capacity greater than 1 MW. In the remaining 5%, there are more than 4000 functional plants below 200 kW.

In the small and micro turbines, the diffuser technology can show the most promising developments. Indeed, the best suit for DAWT application is in the urban environments where local winds, enhanced by turbulence conditions, can give a reasonable contribution, especially going towards a decentralized energy system.[29].

Over the last three decades, the energy transition has increasingly become central to national and international policies, hand in hand with the awareness pf the anthropogenic component of global warming, that could potentially become harmless for the mankind thanks to the development and the market penetration of new technologies. At the same time, people miss the perception of how little time is left before the critical tipping point is reached.

The chart on next page can help to illustrate how narrow the path is at this point. In fact, Fig.2.13, provided by IPCC[30] AR6 report (2021), shows the amount of CO_2 that can still be emitted during the energy transition period to keep the expected temperature increase below the Paris Agreement goals. Indeed, the grey segment is the sum of CO2 emitted since 1850. Luckily, the trend has a near-linear relationship between the cumulative CO_2 emission and the resulting global warming. Therefore, the remain carbon budget responds to the question

---

[28] Formerly, European Wind Energy Association (EWEA) is the largest wind industry association in Europe.

[29] The policies are rethinking our energy system in term of bringing energy production facilities closer to the site of energy consumption. Following this view, the buildings are no longer viewed only as loads for the electricity grid, but can also become generators useful for aiding heat pumps or charging electric vehicles. The main driver is obviously the photovoltaic cell, but the micro wind turbines can give their contribution.

[30] The Intergovernmental Panel on Climate Change (IPCC) was created in 1988 by the World Meteorological Organization (WMO) and the United Nations Environment Programme (UNEP) for assessing the science related to climate change and provide scientific information that can be used by policymakers to develop climate policies: https://www.ipcc.ch/about/

about how much CO_2 can be still emitted to keep the temperature rise below 2° C. The remain carbon budget is the difference between CO_2 emitted under a specific scenario and what we have already emitted (fixed amount). Scenarios SSP-8.5, called "business as usual" because no relevant policies against global warming are implemented, yields a temperature rise of at least over 1.5° C by 2050, but the level of uncertain is great: more than half of outcome is over 2° C. Naturally, in this case, the humanity allows itself to use more than 2500 $GtCO_2$ before 2050. On the opposite side, the most environment-friendly scenario, SSP1-1.9, gives
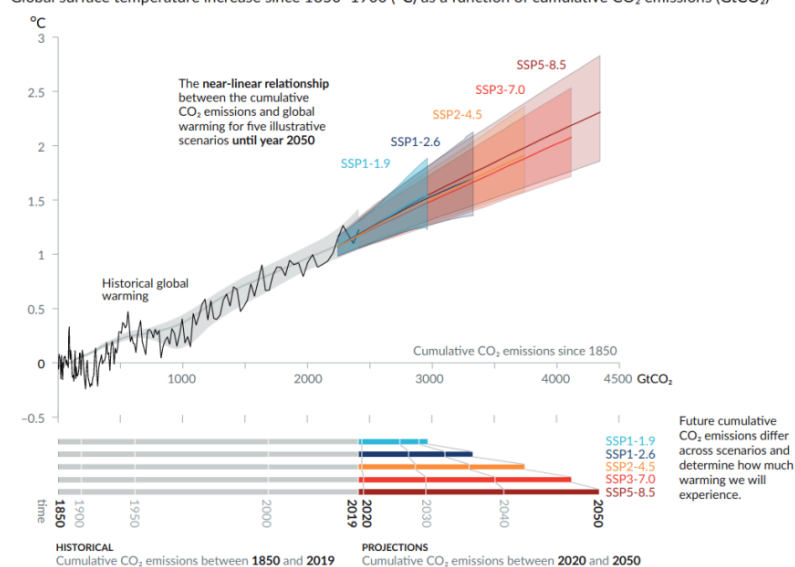
Figure 2.13: Expected temperature increase respect the amount of CO_2 could be emitted in accordance of several scenarios. Source:IPCC AR6

limited time, and therefore limited CO_2 allowed, to keep the trend below 1.5° C if not even below 2° C:[31] less than 1000 $GtCO_2$. This chart should be taken as reference for defining the necessary energy policies and the timing left for phasing out fossil fuels. In any scenario, IPCC stresses the need to develop CO_2 removal technologies from the atmosphere by 2050 to curb CO_2 ppm in the air and keep global warming below 2° C.

On the 24th of February 2022, the Russian Federation started a war against Ukraine, bringing the entire world into a new phase of international relations. Without undermining the human pain owing to the war, but keeping focus on energy challenges, the European Union, as well as Italy, heavy dependence on Russian gas yield it an asset for political influence. Before the war outbreak, polit-

---

[31]The Paris Agreement targets is stated in accordance with scientific studies that 1.5° C is a 'tipping point', beyond that the Earth system capacity to stabilise the temperature starts waning, pushing towards enhancing warming.

ical intentions were addressed to use the gas market between Europe and Russia as a commercial link between nations, helpful to avoid disruptive choices from both side. Unfortunately, this strategic position did not pay in terms of avoiding the war return on European soil After the outbreak, the erosion of relations between Western Europe and Russia will speed up the EU process towards renewable energy sources, notably solar and wind, curtailing the transition phase backed by natural gas. At the same time, an unexpected comeback of electricity production by coal, especially in German, which is reluctant to modify its nuclear phase-out schedule, is also possible, but in the long term view the renewable sources should increase the market penetration as a consequence that are more independent by foreign countries. Additional, the Hydrogen technology as energy storage system from renewable could find new investments as the necessary infrastructure is partially overlapping with the existing gas network.

2.3   Round-up History Of Diffuser Augmented Wind Turbines

Although already in 1926, Albert Betz[32] provided the first presentation of augmented wind turbine concept - his keystone idea was to raise the outcome power thanks to a diffuser that reduces the pressure in front of the rotor -, the nomenclature continues not to be standardised because the manner in which the augmentation can be obtained has been developed in so many different ways. Likely, this has happened until now because this technology has not yet had a commercial market that pushes toward standard classification and naming. However, the diffuser technology follows the same categories used by traditional wind turbine, slicing the group by type of rotor, scale, axis of rotation (vertical or horizontal), onshore or offshore deployment. Fig.2.14shows a short diagram about classification. Moreover, the ongoing research level, where this technology currently states, entails that it's unclear which features are more hopeful to improve the performances. Therefore different diffuser designs are proposed. Fig.2.15 harvests the last ones and most commons.

The *simple diffuser*, Fig.2.15(a), shapes a converging inlet coupled with a diverging outlet and places the rotor in the narrowest diameter.

In the group *brim and flange technology*, Fig.2.15(b), (Ohya and Karasudani 2010) proposed a competitive new class called 'Wind Lens'. The strength of this technology is the autonomous control when wind changes direction, thanks to the

---

[32]Albert Betz (1885 - 1968), German physicist known for being one of pioneers in wind technology field
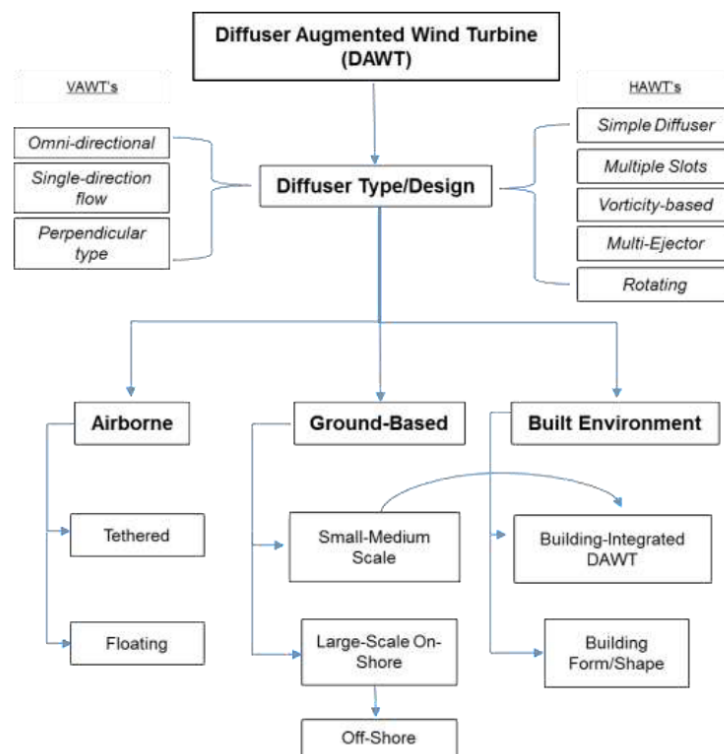
Figure 2.14: Classification of wind turbine based on augmented concepts. Source:(Agha et al.2018)

brim-based yam control. The success of this approach derives from having a more compact size. In opposition of flange solution, (Agha et al.2018) summarises from supplementary studies that 'in the downstream region at exit, vortex structures rapidly deteriorated for the flanged-diffuser system but this was observed further downstream in the bare wind turbine.'

The *multiple slotted diffuser*, Fig.2.15(c), aims to increase the amount of mass inlet supplying additional air flow into the wake of the turbine with a supplemental diffuser. The new configuration enables the creation of a lower back pressure useful to obtain a greater mass flow through the rotor.

Since the 80s, it has been thought to increase the pressure differential before and after the rotor, reducing the pressure on the wake side via vorticity[33] The *Vorticity Based Turbines*,2.15(d), have a wide-angle diffuser able to provide a circumferential velocity component. Early studies tried to work with an open angle of 16°. The best outcome was a generic reduction of 60 % in the total diffuser losses, but 'above this threshold, the creation of a re-circulating zone leads to further dissipative losses'[34].

The DAWT's group, based on the opportunity to add ejectors (single or

---

[33]A short explanation about vorticity is set in Subsection:3.4.

[34](Agha et al.2018)
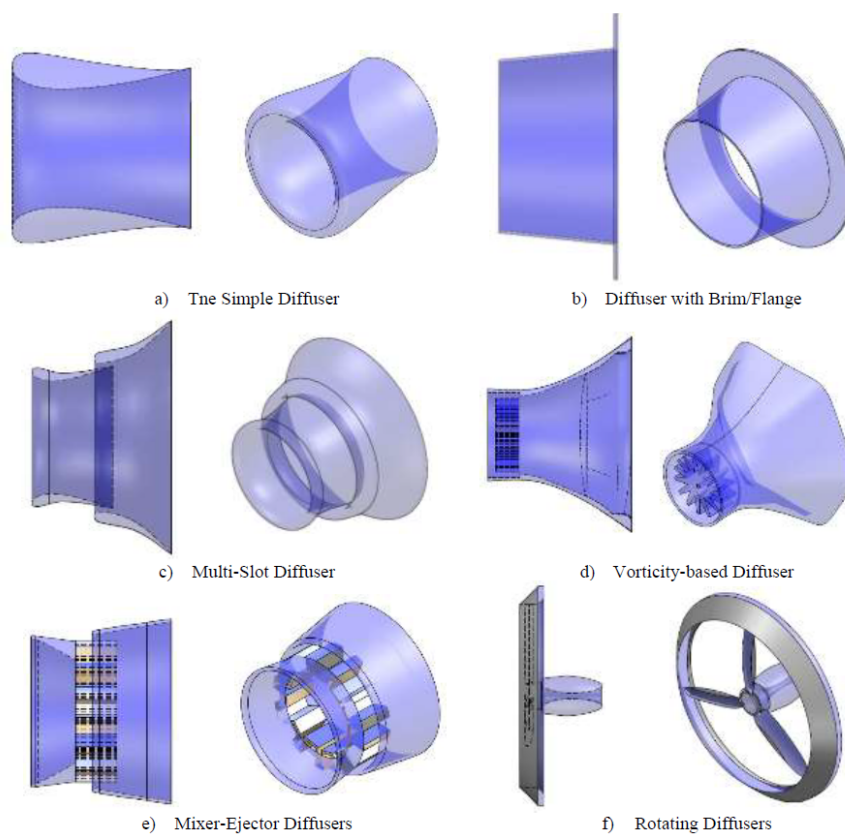
Figure 2.15: The main type of diffuser, developed over time. Source(Agha et al.2018)

multiple-stage), is named *Mixer Ejector Wind Turbine*, Fig.2.15(e).

The wind manufacturing FloDesign[35], registered a US patent thanks to the work of (Presz and Werle2009), illustrated how the ejectors should work coupled to a shrouded wind turbine.

The last type of DAWT, *Rotation Diffuser* in Fig.2.15(e), also called dynamics diffuser,allows the diffuser to rotate around the horizontal rotor axis. Hence, the diffuser rotation happens coupled to the rotor because the blades are fixed directly to diffuser framework, reducing, therefore, the structural stress on the blades. Per contra, (Agha et al.2018) notices that 'it is not clear the effects of the rotating diffuser in the aerodynamic drag of the turbine and whether this reduces the rotor rpm'.

Ducted Turbine Naming

Although the concept of ducted turbines has already almost one century of live, still nowadays the nomenclature continues not to be standardised. Indeed, already in 1926[36], Albert Betz provided the first presentation of augmented wind

---

[35]Nowadays acquired by Ogin Technology Company
[36]see (Betz1926)'publication

turbine concept: his keystone idea was to raise the outcome power thanks to a diffuser that reduces the pressure in front of the rotor and, therefore pressure after the rotor. However, despite the varieties of technologies, to refer to a wind turbine able to increase its mass flow due to back pressure, the denomination of diffuser augmented wind turbine or, shortened, DAWT, is the most common. Sometimes, in case of a micro power plan, DAMWT, is also prevailing. Other denominations, e.g. ducted or shrouded wind turbines, are less frequent but refer to the same type of machines.

Chapter 3

Overview Of Wind Turbine Theories

Historically, three different approaches have been developed since the beginning of rotor aerodynamic research in the XIX century.

1. The Blade Element Theory (BET) and the Momentum Theory: both of which have been merged into the Blade Momentum Theory (BEM)
2. Vortex Theory
3. The Computational Fluid Dynamics (CFD) [1]

The **BET**, originally elaborated by ([Froude1878](#)) and ([Drzewiecki1892](#)) to effectuate load calculation on rotors, 'provides the loads in the blade based on: the blade geometry (chord length and oriented span-line of the blade), the 2D foil performance at each span-wise position (i.e. C_l,C_d,C_m) and the flow velocity at the rotor. The flow is usually determined using another theory, such as momentum theory. The combination of the BET with the Momentum Theory yields the Blade Element Momentum Method.'[2] The BET associated to the case of a ducted turbine has been developed by ([Fletcher1981](#)) for the first time, starting from classical BET, a contribution owing to ([Glauert1935](#)). Fletcher's work took in consideration wake rotation effects and blade Reynolds number effect and proposed "two empirical parameters: the *exit pressure coefficient* and *the diffuser efficient*, to incorporate the influence of the diffuser into the analysis".[3]

The **Vortex Theory** considers substituting each of the rotor blades with "a lifting line and a vortex sheet is continuously shed from the trailing edge"[4]

The **CFD** simulates fluid motion thanks computational elaboration of Naiver-Stokes equations, that need to be implemented by numerical methods because

---

[1] Obviously, CFD is the latest one that has been developed because only since few years computers have been able to solve enough calculations to achieve a rewarding analysis. Consequently, now CFD can take advantage of the results acquired from the other theories. Also, a deeper development of vortex theory can be obtained by raising the computation power.

[2] ([Branlard2017](#))

[3] ([Tavares Dias do Rio Vaz et al.2014](#))

[4] ([Vaz and Wood2016](#))

an analytic solution can be found only in case of simple geometry and laminar flow. The Navier-Stokes equation for a turbulent flow can be resolved using a numerical method, like Finite Element Method (FEM) or Finite Volume Method (FVM),discretising differential equations. While CFD is noted for its being more time-consuming before obtaining relevant results, it is usually coupled with optimisation methods based on experimental or mathematical models.

3.1 Wind Turbine Classic Theory

3.1.1 Actuator Disc Theory

The Actuator Disc Theory (ADT), nowadays known as classic theory, was developed by Albert Betz around the 1930s. The actuator disc approach is based on the assumption that 'the rotor consists of an infinite number of blades since the actuator disk can be thought of as an infinite number of lifting lines distributed over the azimuth.'[5]
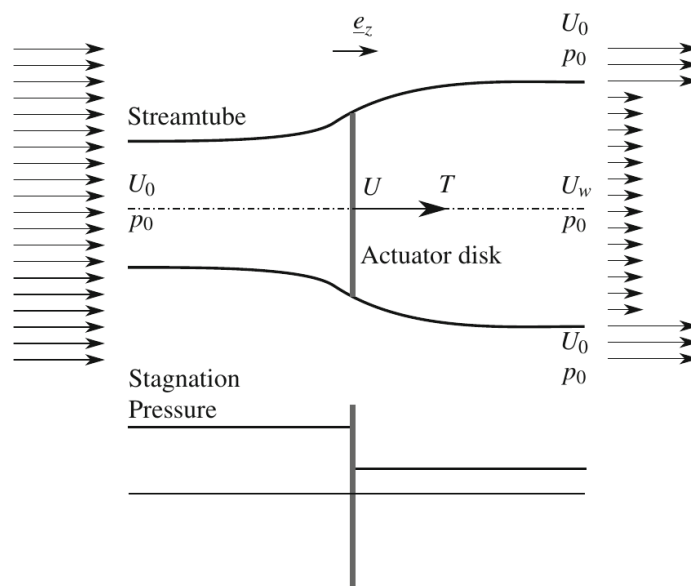
Figure 3.1: Actuator Disc model, image from (Branlard2017). The stagnation pressure drop is in line with the actuator disc.

As Fig.3.1illustrates,the wind turbine is represented by a uniform and continuous disc, through which the air flows. Betz did some basic assumptions for the simplify model[6]:

- homogeneous incompressible steady state flow

---

[5](Branlard2017).

[6](Pavesi2013)

- no friction drag
- uniform thrust over the disk or rotor area
- no rotating wake
- the state pressure far upstream and far downstream of the rotor is equal to the undisturbed ambient static pressure
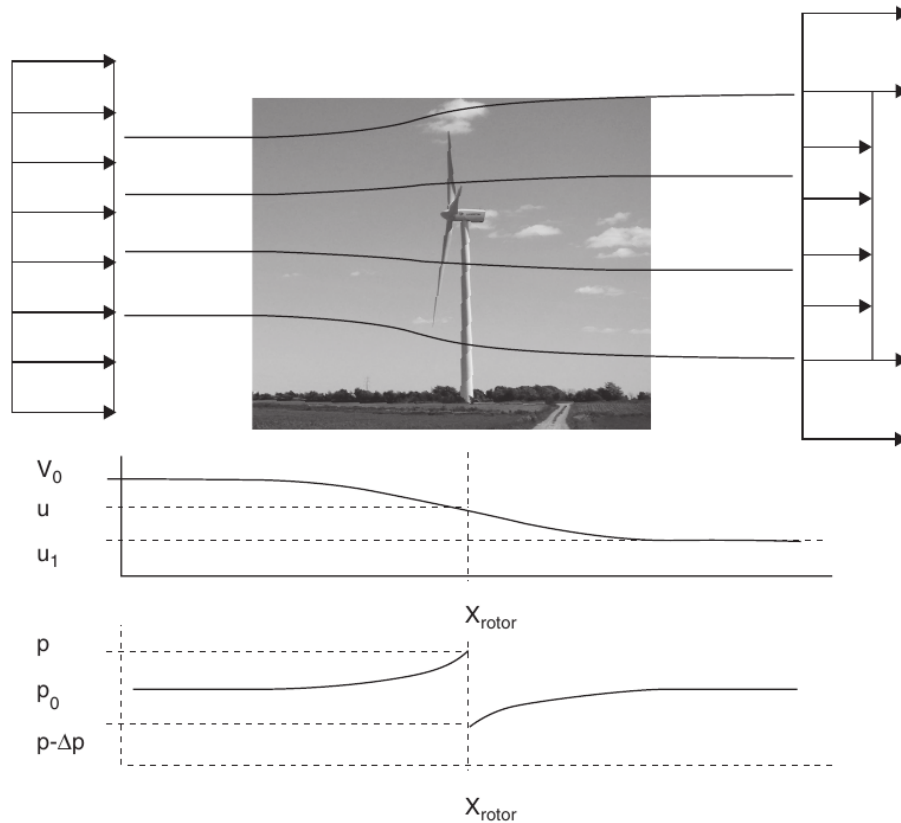
Figure 3.2: Sketch of flow around the ideal wind turbine rotor, from (Bak2013) (*Source:* Photo: Vestas V80 at Tjæreborg Enge, Denmark, by Christian Bak, DTU Wind Energy

The sketch in Fig.3.2allows us to visualise better which is the greatest effect on the wind flow due to disc presence, i.e. the extraction of kinetic energy from the wind means a reduction of absolute pressure. Indeed, far downstream to the rotor, the static pressure returns to ambient value, but the kinetic energy is reduced as consequence of turbine conversion.

Defining *a* as *axial induction factor*, the induced wind velocity[7] on the disc and on the wake can be written as:

$$\begin{cases} U_\infty - u = U_{disc} = (1-a)U_\infty \\ U_\infty - u_1 = U_w = (1-2a)U_\infty \end{cases} \tag{3.1}$$

---

[7]The wind speed is always indicated with the U letter, although some other reference can be found in the following figures.

Where U_∞ is the undisturbed flow velocity before the disc.

In this way, the *actuator disc velocity* $U_{disc} = aU_\infty$ and *wake velocity* $U_w = 2aU_\infty$ can be easily expressed.

Those velocities are characterised by the axial induction factor defined as:

$$a = \frac{U_\infty - U_{disc}}{U_\infty} \tag{3.2}$$

As Fig.3.2 shows, the cross-sectional area becomes wider in front of the disc as well as the mass flow decreases in accordance with the mass continuity equation applied in three different spots: in front of the disc, on its line and downstream of the disc.

$$\dot{m} = \rho A_\infty U_\infty = \rho A_{disc} U_{disc} = \rho A_w U_w \tag{3.3}$$

Therefore, the cross-sectional area in front of the turbine is smaller than the swept area. Hence, an evident physical limit happens. This correlation is true when the fluid is considered incompressible like the air.

As also discussed further, the key idea beyond ducted turbines is to decrease the back pressure thanks to a diffuser. In such a way, the mass flow rate upstream is larger with respect to what a wind turbine of the same rotor length can handle. In this way, researchers usually intend that DAWTs are able to obtain a C_p value higher than Betz limit in reference to the same rotor size. However, Bussel(2007) observes that in a ducted turbine 'the amount of energy extracted per unit of volume is identical to the amount of energy for an unaugmented turbine' because air mass upstream of the disc is increased by a factor correlated to the back pressure downstream.

The force acting on the disc depends entirely to the rate of change of momentum that is equal to the overall change of velocity times the mass flow rate. The force also is equal to the difference of pressure across the actuator disc Δp[8]:

$$F = \Delta p A_d = (U_\infty - U_W)\rho A_d U_d = (U_\infty - U_W)\rho A_d U_\infty(1 - a) \tag{3.4}$$

The force expression can be arranged as:

$$F = 2\rho A_d U_\infty^2(1 - a)a \tag{3.5}$$

The next step is to calculate the power P from F as function of $U_d F$:

$$P = FU_d = 2\rho A_d U_\infty^3 a(1 - a)^2 \tag{3.6}$$

---

[8]The value of Δp can be calculated applying Bernoulli's equation ($1/2\rho U^2 + p + \rho gh = cost$ upstream and downstream the disc.)

It is remarkable the cubic correlation between the power and the undisturbed velocity and therefore the impact of limited wind speed increment with the feasible power output.

The key performance parameters are:

- *Power Coefficient*[9]

$$C_P = \frac{P}{1/2\,\rho A U_\infty^3} = 4a(1-a)^2 \tag{3.7}$$

- *Thrust Coefficient*

$$C_T = \frac{P}{1/2\rho A U_\infty^2} = 4a(1-a) \tag{3.8}$$

Betz found the well-known literature Betz limit, while he was looked for the optimum value of power coefficient. Indeed, looking for the optimum of (3.7)

$$\frac{dC_p}{da} = 4(1-a)(1-3a) = 0 \tag{3.9}$$

the optimum value is obtained at $a = 1/3$ where $C_p^{max} = 16/27$. A turbine can extract the maximum of 59.3% by the entire amount of wind energy available. This is a physical limit depending by the mass conservation equation and it is not correlated to the efficiency of the turbine.

3.1.2   DAWT Classical Theory

The development of DAWT classical theory has taken many years, starting since (Fletcher1981). Noteworthy are the contributions of (Hansen et al.2000) and (Tavares Dias do Rio Vaz et al.2014).

The hypothesis beyond this approach is to just extend the classic theory, taking into consideration the losses through the diffuser.

In the early 1980s, (Fletcher1981) illustrated the power coefficient can be written as:

$$C_{p,d} = \epsilon\left[1 - \left(\frac{U_w}{U_\infty}\right)^2 - (1-n_d)(1-\beta^2)\epsilon^2\right] \tag{3.10}$$

where $\epsilon = U_{disc}/U_\infty$ is the speed-up ratio between the axial disc velocity and the undistributed wind velocity, $\beta = A/A_3$ is ratio between the rotor area A and the diffuser exit-area A_3. Finally, n_d is the *diffuser efficiency*, defined by

$$n_d = \frac{p_3 - p_2}{\frac{1}{2}\rho(U_{disc}^2 - U_3^2)} \tag{3.11}$$

---

[9]P is the power output of the turbine without considering mechanical and electrical efficiency of the rotor and the generator, respectively. Therefore, P is smaller than the real output achievable.
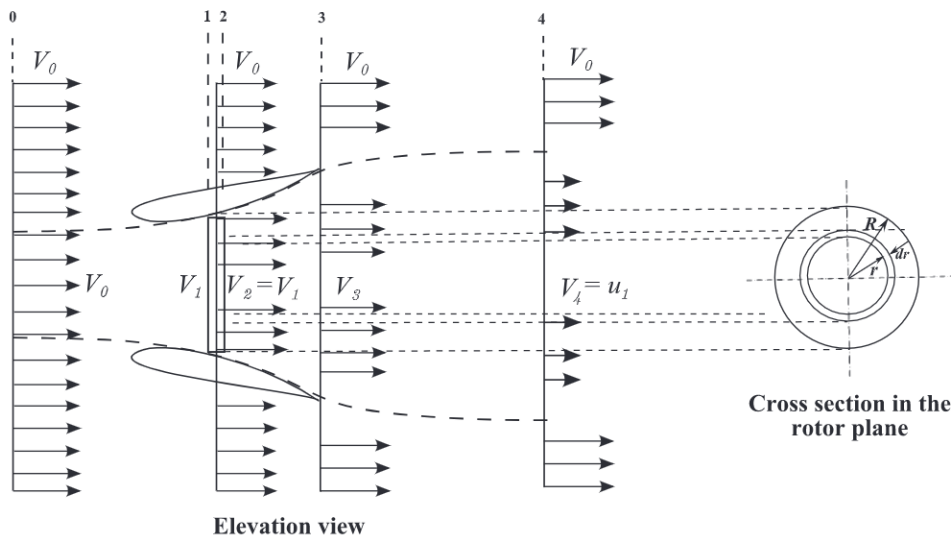
Figure 3.3: Actuator disc model with a diffuser, data from (Tavares Dias do Rio Vaz et al. 2014). Here, the annotations mean: $V_0 = U_\infty$, $V_1 = U_{disc}$, $V_3 = U_3$, $V_4 = U_w$. The dotted lines indicates the control volume boarders.

If we define Cp_3 as the pressure coefficient at the diffuser exit - assuming it's independent of radius:

$$Cp_3 = \frac{p_3 - p_0}{\frac{1}{2}\rho U_\infty^2} \tag{3.12}$$

Substituting Eq. (3.12) in (3.10), we can write:

$$C_{p,d} = \epsilon(1 - Cp_3) + \epsilon^3[n_d(1 - \beta^2) - 1] \tag{3.13}$$

At this point, we make a strong hypothesis in order to explicit U_w from the equation:

$$\left(\frac{U_w}{U_\infty}\right)^2 = \beta^2\epsilon^2 + cp_3 \tag{3.14}$$

Indeed, we assume to apply the same conditions for the output of a typical wind turbine at the exit of the diffuser; thus, no extra back pressure is pondered. The hypothesis is made to obtain as close as possible equivalence to momentum relations in case of bare wind turbine, as illustrated by (Bussel1999), which yields

$$U_w = (1 - 2a_d)U_\infty \tag{3.15}$$

where a_d is the *axial induction factor* considering the diffuser effect.

The main advantage of a diffuser is to increase the mass flow rate through the disc plane due to a back pressure drop in the downstream flow created by the diffuser. The consequence is a speed up of the wind velocity before the air intersects the rotor, see Fig.3.4.
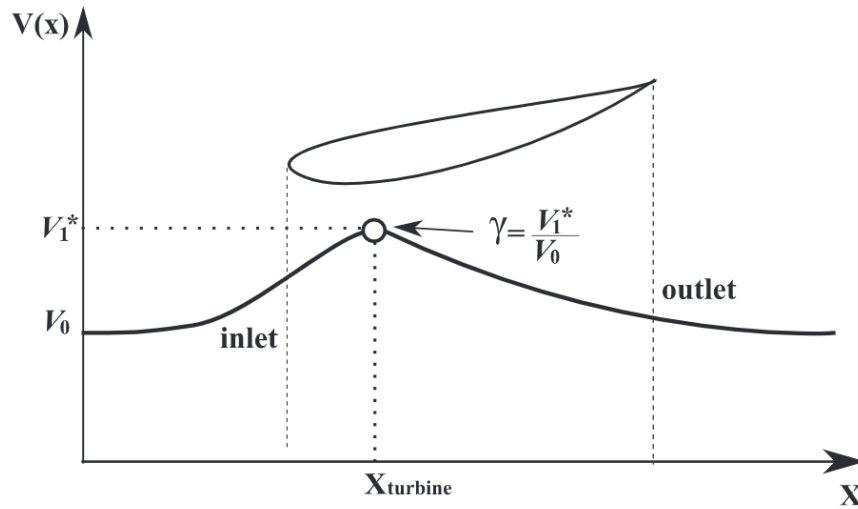
Figure 3.4: Illustration of the axial velocity profile on the symmetry axis of a diffuser without turbine(Tavares Dias do Rio Vaz et al.2014)

The dimensionless parameter γ, called *maximum speed-up ratio*, is defined as the ratio of the maximum axial velocity of flow in the diffuser, U_{disc}^{max}[10] , by the undisturbed wind speed.

$$\gamma = \frac{U_{disc}^{max}}{U_\infty} \tag{3.16}$$

Following this definition, the expression for the flow velocity on disc plane is clearly:

$$U_{disc}^{max} = \gamma(1 - a_d)U_\infty \tag{3.17}$$

Recalling the previous ϵ definition, γ is equal:

$$\epsilon = \frac{U_{disc}}{U_\infty} = \gamma(1 - a_d) \tag{3.18}$$

Consequently, Eq.3.12and Eq.3.13become:

$$C_{p3} = (1 - \beta^2\gamma^2)(1 - a_d)^2 + a_d(3a_d - 2) \tag{3.19}$$

$$C_{p,d} = \gamma(1 - a_d)^2[4a_d + \gamma^2(1 - a_d)(1 - \beta^2)(\eta_d - 1)] \tag{3.20}$$

Eq.(3.20) can be simplified if the diffuser losses are neglected, assessing $\eta_d = 1$:

$$C_{p,d} = \gamma 4a_d(1 - a_d)^2 \tag{3.21}$$

In case the value of γ is equal to 1, Eq. (3.21) is analogue for a bare turbine.

---

[10]In the Fig.3.4, U_{disc}^{max} is indicated with V_1^*.

The thrust coefficient $C_{T,d}$ is the result of applying the energy balance equation likewise to the classical theory and using the control volume, delimited inside the dotted lines in Fig.3.3:

$$C_{T,d} = \frac{T_d}{\frac{1}{2}\rho A U_\infty^2} = \frac{\frac{1}{2}\rho A (U_\infty^2 - U_w^2)}{\frac{1}{2}\rho A U_\infty^2} = 4a_d(1 - a_d) \tag{3.22}$$

From Eqs.(3.21) and (3.22), $C_{p,d}$ is:

$$C_{p,d} = \frac{P_d}{\frac{1}{2}\rho A U_\infty^3} = \frac{U_{disc} T_d}{\frac{1}{2}\rho A U_\infty^3} = \epsilon C_{T,d} \tag{3.23}$$

Similarly to the case of a free actuator disc, $C_{p,d}$ has the maximum value when $\alpha_{opt} = 1/3$ and is equal to:

$$C_{p,d}^{max} = \gamma \frac{16}{27} \tag{3.24}$$

Eq. (3.24) is a relevant result. It means, as (Tavares Dias do Rio Vaz et al. 2014) noticed, that the 'theoretical limit for a DAWT is a function of a diffuser geometry'. Other authors, like (Hansen et al.2000) and (Bussel2007) reached the same outcome. For example, (Bussel2007) writes 'that power augmentation is proportional to the mass flow increase generated at the nozzle of the DAWT'. In other words,' without extra back pressure at the diffuser exit this means that the maximum power coefficient related to the exit area is equal to Betz maximum 16/273'.[11]

Starting from this conclusion, (Tavares Dias do Rio Vaz et al.2014) noticed: 'The significance of this result is that, mathematically, the thrust on the rotor is similar to the actuator disc theory, but the response is different, because the axial induction factor at the rotor plane is influenced by the diffuser'.

As of Eq.(3.20) in case the fluid is ducted by a diffuser towards the turbine, the research of a_{opt} when $dC_{p,d}/da = 0$ gives the result:

$$a_{opt} = \frac{4 + 3\gamma^2(\eta_d - 1)(\beta^2 - 1)}{12 + 3\gamma^2(\eta_d - 1)(\beta^2 - 1)} \tag{3.25}$$

Therefore, $C_{p,d}^{max}$ becomes

$$C_{p,d}^{max} = \frac{256\gamma}{27[4 + \gamma^2(\eta_d - 1)(\beta^2 - 1)^2]} \tag{3.26}$$

The latter Eq. (3.26) is the Betz limit in case of a ducted turbine[12].

---

[11](Bussel2007)

[12]Indeed, setting $\gamma = \eta_d = 1$, you can immediately obtain $a_{opt} = 1/3$ and $c_p^{max} = 16/27$.
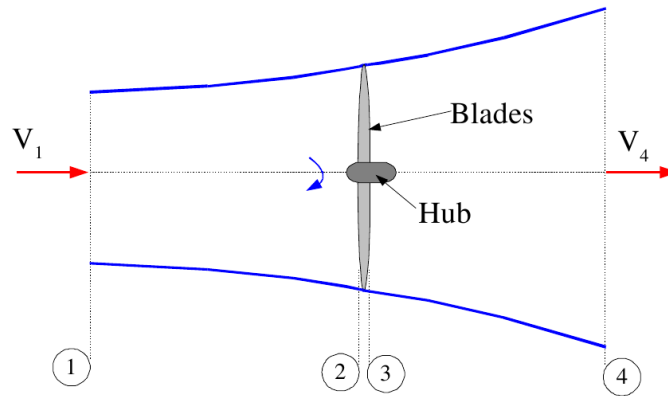
Figure 3.5: Flow Stream around a wind turbine. Source:(Ingram2011)

3.2 Wind Turbine Blade Element Momentum Theory

The Momentum Theory applies the conservation laws for a flow considered steady-state, incompressible and axisymmetric. The fluid is assumed homogeneous and inviscid.

Axial Force in Momentum Theory

Given a frictionless stream tube, illustrated in Fig.3.5and considering $p_1 = p_2$ and therefore $U_2 = U_3$,the already mentioned Bernoulli's equation has the expression:

$$p_2 - p_3 = \frac{1}{2}\rho(U_1^2 - U_4^2) \tag{3.27}$$

Considering that the pressure divided by an area is a force, Eq.3.27can be rearranged as:

$$dF_x = (p_2 - p_3)dA \longrightarrow dF_x = \frac{1}{2}\rho(U_1^2 - U_4^2)dA \tag{3.28}$$

The velocity on disc plane and the far wake velocity can be described with the axial induction factor; therefore a new formulation of dF_x is:

$$dF_x = 4\pi\rho U_\infty^2 a(1 - a)rdr \tag{3.29}$$

Tangential Force in Momentum Theory

Due to the conservation of angular momentum, the spin in the rotor wake must have the opposite sign to the rotor direction. The energy, needed to create the spin motion inside the fluid, reduces the amount of mechanical energy available. Consequently, a theory that takes also into account the rotating wake obtains power coefficient smaller than classic theory.

If ω is the *wake angular velocity* and the letter Ω is associated to *rotor angular speed*, the expression of the torque into an annular[13] is the result of the following thought process. Indeed, the elemental torque generated by an annular corresponds to the rate of change of angular momentum of the fluid, crossing the annular.

$$
\boxed{\text{Moment of an annular: } I = mr^2}
$$
$$
\boxed{\text{Angular Moment: } L = I\Omega}
$$
$$
\boxed{\text{Torque: } Q = \frac{dL}{dt}}
$$

Therefore,

$$
Q = \frac{dI\omega}{dt} = \frac{d(mr^2\omega)}{dt} = \frac{dm}{dt}r^2\omega = d\dot{m}\omega r^2 \tag{3.30}
$$

Explicating the swept area in the mass flow rate definition $d\dot{m} = \rho A U_d$, $d\dot{m}$ isi equal to $\rho U_d dA$ and therefore,

$$
dQ = \rho\omega r^2 U_d dA \tag{3.31}
$$

It's time to recall the definition of *angular induction factor* a':

$$
a' = \frac{\omega}{2\Omega} \tag{3.32}
$$

. Giving the correlation between U_d and U_∞ from Eq.(3.1),

$$
dQ = 2a'(1-a)U_\infty\rho\omega r^2 dA \tag{3.33}
$$

.

Eventually, the power calculated on a differential annular is:

$$
dP = \Omega dQ = \frac{1}{2}\rho A U_\infty^3\frac{8}{\lambda^2}a'(1-a)\lambda_r^3 d\lambda_r \tag{3.34}
$$

where λ, a fundamental parameter, means:

- *Tip Speed Ratio* $\lambda = \frac{\Omega R}{U_\infty}$

- *Local Speed Ratio* $\lambda_r = \frac{\Omega r}{U_\infty}$

3.2.1   Blade Element Theory

The theory considers to split the blade into several annular elements; each one is segregated respect the neighbours. The force equilibrium, calculated on

---

[13]Annular is a ring section of radius dr,that wraps the disc: see Fig.3.7.

one element, does not have effect for the calculation regarding the surrounding elements. Each element is nothing more than a section of the wind blade. The blades are generated extruding an airfoil into a wing from a hub up to the tip. The flow that interacts with the blade has two stagnation points: the leading edge upstream and the trailing edge downstream. In the stagnation point, the fluid has the local velocity equal to zero, and therefore the static pressure reaches the maximum value.

Each element is unique identify by its assigned radius r from the hub, its chord length c and its twist angle θ. Moreover, it is not required to assume the same shape of airfoil for all the elements, but the designer can choice for each part the airfoil able to perform well[14]. Fig.3.7indicates easily the meaning to divide the blade in differential element of thickness dr.

Lift and Drag coefficients

From Fig.3.8, the reacting force F acting on the blade from the flow can be decomposed into two components respect the direction of U_∞:

- **Lift**:   Perpendicular to U_∞

$$L = \frac{C_L}{1/2\rho U_{rel}^2 cR} \qquad [N/m] \qquad (3.35)$$

- **Drag**:   Parallel to U_∞

$$D = \frac{C_D}{1/2\rho U_{rel}^2 cR} \qquad [N/m] \qquad (3.36)$$

In the definition of lift and drag,the two respective coefficients appear: C_L and C_D. The c expresses the length of the airfoil, identified by the chord. Usually on the chord line at at $c/4$, the moment M[15] is collocated and evaluated by:

$$M = \frac{C_M}{1/2\rho U_{rel}^2 c} \qquad (3.37)$$

In fig.3.8, it is represented that only the Lift and the Drag acting on the blade are considered in the present analysis. Those forces are the aerodynamic characteristic of the airfoil. Also, in the Fig.3.8, the blade pitch angle θ defines the angle between the airfoil chord section at radius r and the plane of rotation. The angle θ is one of the three angles defined by the velocity axis and the chord axis:

---

[14]Usually, a blade is composed by numerous different types of airfoil, i.e. up to more than 20 airfoils for the bigger ones.

[15]The moment M has a positive sign if push for a blade rotation in clockwise direction.

- Flow angle φ;
- Angle of attach α;
- Twist angle θ.

The relation between the angles is:

$$\varphi = \alpha + \theta \tag{3.38}$$

In addition, the flow angle is bound to the axial velocity U_n and the tangential velocity U_t:

$$\tan(\varphi) = \frac{U_n}{U_t} = \frac{U_\infty(1-a)}{\Omega r(1+a')} = \frac{(1-a)}{(1+a')\lambda_r} \tag{3.39}$$

From Eq.(3.39), a new relation between a and a' is evident:

$$a = a'\lambda_r\cot(\varphi) \tag{3.40}$$

Therefore, it is also true that the relative velocity, called U_{rel}, between U_n and U_t is equal to:

$$U_{rel} = \frac{U_\infty(1-a)}{\cos(\phi)} \tag{3.41}$$

Airfoils The airfoil literature is very wide[16] because the characteristics of the airfoil have a straightforward impact on lift. Indeed, as shown in Fig.3.6, C_l rises linearly for a small angle of attack, while C_d remains close to zero. In this region, the ratio C_l/C_d keeps getting higher.[17] Approximately above the angle of attack is greater than $10°$, α is so large than a standstill happened a short distance from the trailing edge, bringing about flow reversal and boundary layer separation. Consequently, the blade enters in stall conditions, generating a lift drop and a drag rise. The maximum ratio is reached close to stall region. Hence, the turbines need working close to the stall region to have the maximum lift contribution, without going voluntary into the stall zone unless the power control system imposes a stall condition with the purpose of reducing the output.

The most common airfoil profiles are S822 and S823, which are also useful in shrouded cases. The coefficients C_L, C_D and C_M are functions of angle of

---

[16]Currently, the airfoils database contains more than 1600 shapes and is listed in accordance with NACA nomenclature. Source: http://airfoiltools.com/(last access: 1 August 2022)

[17]Ideally, C_L proceeds with a linear gradient equal to $2\pi/rad$ up to a maximum in correspondence of a determinate value of α.
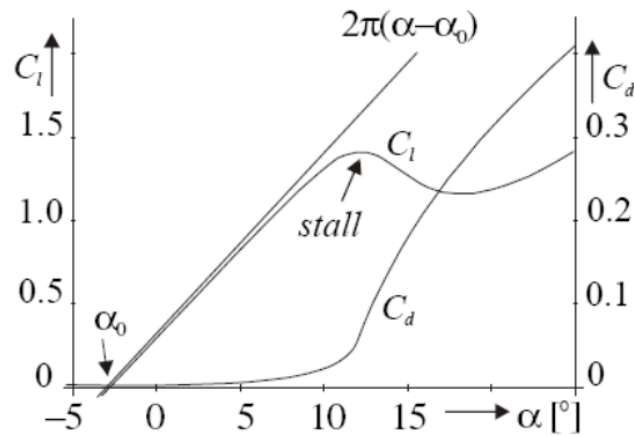
Figure 3.6: c_l and c_d behaviour for a generic airfoil respect angle of attach α. Source: (Pavesi2013)

attach,α, Reynolds number,Re, and Mach number Ma.[18] The Reynolds number[19] for a wind turbine is evaluated as:

$$Re = \frac{c\rho U_\infty}{\mu} \tag{3.42}$$

It is immediately clear the strictly connection between the chord length and the velocity and, via Re, the lift feasible by the blade.

The BET is valid under the following assumptions:

- There is no aerodynamic interaction between contiguous blade elements;
- the overall loads can be determined only by taking into account lift, drag and moment coefficients evaluated in the radial position;
- The coefficients are calculated using a two-dimensional model.

From Fig.3.8, one can extract C_n and C_t, respectively the normal and tangential coefficient[20]:

$$C_n = L\cos(\varphi) + D\sin(\varphi) \qquad C_t = L\sin(\varphi) - D\cos(\varphi) \tag{3.43}$$

The Fig.3.9can help to understand :

- The overall *Thrust* T generated on the blade is the result of the integral:

---

[18]Mach number is the ratio of the velocity respect sound velocity. The reduction of maximum lift coefficients is experimentally noted correlated to an increase of Mach number. The reason is attributed to the separation of the boundary layer for smaller α. Anyway in case of subcritical Mach number, typical for wind turbine, the correlation is so weakness that no mistakes are taken if it is neglected.

[19]a more extensive focus on Re is carried out in Subsection:4.2.2.

[20]In the figure, P_n indicates the normal coefficient and P_t represents the tangential coefficient.

Figure 3.7: Sketch of the division of a wind turbine rotor into annular elements, from (Bak 2013) (*Source:* NM80 photo at Tjæreborg Enge, Denmark by Christian Bak, DTU Wind Energy.)

$$p_n = L\cos\phi + D\sin\phi$$
$$p_t = L\sin\phi - D\cos\phi$$
$$U_t = \Omega r(1+a')$$
$$U_n = U_0(1-a)$$
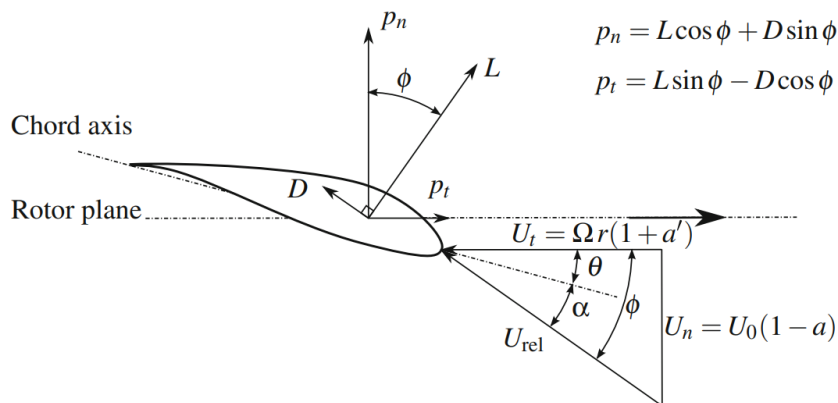
Figure 3.8: Blade velocity triangle and resulting aerodynamics forces. Source:Branlard (2017)

$\int_{r_{hub}}^{R} dC_n\, dr$ [21]

- The overall *Torque* Q generated on the blade is the result of the integral:
$\int_{r_{hub}}^{R} dC_t r\, dr$

Therefore, the trust T and the torque Q of each element can be derived from its

---

[21]The hub, occupied the lowest part of the turbine with a radius r_{hub} and doesn't give a contribution to the energy production
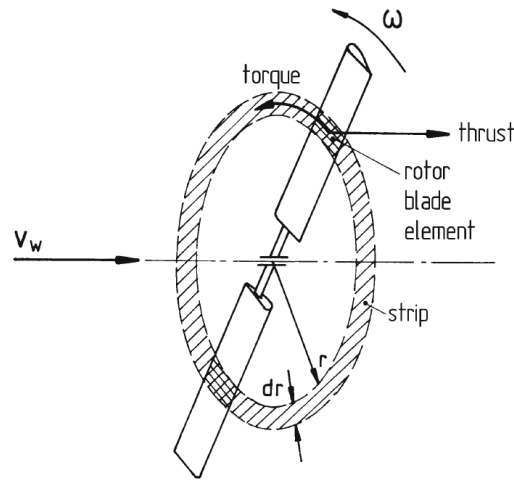
Figure 3.9: Thrust and Torque on single blade element. Source: (Hau2013)

characteristic C_L and C_D depending by the airfoil and the angle of attach α, the relative velocity U_{rel}, which is also dependent on α through its connection with the speed triangle and the chord length c.

If n_b is the number of blade, the aforementioned relationships can be harvests in the following equations:

$$dT = \frac{1}{2}n_b \rho U_{rel}^2 [C_L \sin(\varphi) + C_D \cos(\varphi)]c\,dr \tag{3.44}$$

$$dQ = \frac{1}{2}n_b \rho U_{rel}^2 [C_L \cos(\varphi) + C_D \cos(\varphi)]c r\,dr \tag{3.45}$$

Using the definition of solidity:

$$\sigma = \frac{n_b c}{2\pi r} \tag{3.46}$$

and the relation between flow angle φ and U_{rel} by Eqs.(3.39)-(3.41):

$$dT = \sigma\pi\rho\frac{U_\infty^2(1-a)^2}{\sin^2(\varphi)}[C_L \sin(\varphi) + C_D \cos(\varphi)]r\,dr \tag{3.47}$$

$$dQ = \sigma\pi\rho\frac{U_\infty^2(1-a)^2}{\sin^2(\varphi)}[C_L \sin(\varphi) + C_D \cos(\varphi)]r^2\,dr \tag{3.48}$$

3.2.2 Blade Momentum Theory

The BEM is the most likely tool that engineers aim to use for designing wind turbines, although it is often mitigated with some corrections to consider the losses on the tip and on the hub. The theory gives radial and tangential equations of overall forces acting on the blade. The blade is divided into several segregated

elements of finite radius lengths, shown in Fig.3.9. In each element, there is the momentum balance of forces acting on the blade due to interaction with the wind, on one side of the equations, and on the other side, the overall forces created by lift and drag coefficients along the several sections of the blade. Those equations can be solved with an iterative process.[22]

As (Okda2015) remarks, 'the BEM theory is quite simple yet it gives considerable accurate results. However, due to its assumption, it cannot model some aerodynamic effects on wind turbine rotor. Correction are usually needed for effects such as (...) blade hub and tip losses (...).' The main limit of the Actuator Disc Theory is to neglect the wake rotation. Hence, it is unable to give an output about the torque. Although the Momentum Theory resolves this issue, it does not consider the effects derived by the blade geometry as the chord length and the twist angle as well as n_b of the turbines. For those reasons, BET helps by coming to the same conclusions about thrust and torque through aerodynamic studies. Eventually, the Momentum Theory and the BET can be merged to evaluate the behaviour along the blade.

Describing this through mathematical formulas means equalising:

- Eq.(3.29) and Eq.(3.47):

$$dT \implies \frac{a}{1-a} = \sigma C_L \frac{\cos(\varphi)}{4\sin^2(\varphi)}\left[1 + \frac{C_D}{C_L}\tan(\varphi)\right] \qquad (3.49)$$

- Eq.(3.33) and Eq.(3.45):

$$dQ \implies \frac{a'}{1-a} = \sigma C_L \frac{1}{4\lambda_r \sin(\varphi)}\left[1 - \frac{C_D}{C_L}\cot(\varphi)\right] \qquad (3.50)$$

The glide ratio, C_L/C_D, has a maximum for the optimal angle of attach, correspondent to the maximum torque. It is useful to consider that C_D may be set equal to zero in the design conditions because $C_L \gg C_D$, comparing the highest value of C_L and the lowest value of C_D. In this way, the Eqs.(3.49)-(3.50) can be simplified.

Solving Eqs.(3.49)-(3.50) for a and a' and remembering the definition of normal and tangential force coefficients in Eq.(3.43):

$$a = \frac{1}{1 + \frac{4\sin^2(\varphi)}{\sigma C_n}} \qquad (3.51)$$

$$a' = \frac{1}{\frac{4\sin(\varphi)\cos(\varphi)}{\sigma P_t} - 1} \qquad (3.52)$$

---

[22]An example is provided by GUI BEM tool in Section:4.1.2.

In design condition, $C_D \approx 0$ and Eqs. (3.51) - (3.52) can be rewritten:

$$a = \frac{1}{1 + \frac{4sin^2(\varphi)}{\sigma C_L cos(\varphi)}} \tag{3.53}$$

$$a' = \frac{1}{\frac{4cos(\varphi)}{\sigma C_L} - 1} \tag{3.54}$$

Recalling the relation between a and a' in Eq.(3.40) and thanks to Eqs.(3.53)-(3.54), C_L can be express as a function of λ_r, φ and σ:

$$C_L = \frac{4sin(\varphi)[cos(\varphi) - \lambda_r sin(\varphi)]cos)}{\sigma[sin(\varphi + \lambda_r cos(\varphi))]} \tag{3.55}$$

Power

The power output provides from each element is:

$$dP = \Omega dQ \tag{3.56}$$

Integrating along the whole blade:

$$P = \int_{r_{hub}}^{R} \Omega dQ \tag{3.57}$$

Hence,

$$C_p = \frac{P_{output}}{P_{wind}} = \frac{\int_{r_{hub}}^{R} \Omega dQ}{\frac{1}{2}\rho A U_\infty^3} \tag{3.58}$$

Using the Eq.(3.50), the C_p gets the formulation:

$$C_p = \frac{8}{\lambda^2} \int_{\lambda_{hub}}^{\lambda} \lambda_r^3 a'(1 - a)\left[1 - \frac{C_D}{C_L}cot(\varphi)\right]d\lambda_r \tag{3.59}$$

3.2.3 Schmitz's Formulas

Schmitz's formulas are useful to determine the optimum flow angle and the optimum chord length. Those formulations are really important for further work because the best methods for chord length distribution take their cue from Schmitz. Moreover, the whole research on design methods of HAWT rotor blade, elaborated by (Okda2015), concludes that 'Schmitz methods for optimum flow angle and chord distribution are found to be the simplest and most straightforward result from BEM optimization analysis'[23].

---

[23]summarized by (Batu and Lemu2020)

The equations derived by BEM theory, in particular from the axial induction factor Eq:(3.51) and the lift coefficient Eq: (3.55), that are arranged by (Duran2005) and (Manwell et al.2009) in combination with the power coefficient Eq: (3.59) to lead:

$$C_P = \frac{8}{\lambda^2} \int_{\lambda_{hub}}^{\lambda} \sin^2\varphi(\cos\varphi - \lambda_r\sin\varphi)(\sin\varphi + \lambda_r\cos\varphi)\left[1 - \frac{C_D}{C_L}\cot\varphi\right]d\lambda_r \quad (3.60)$$

Neglecting the drag part, the partial derivative respect the flow angle is set equal to zero to look for the maximum value of φ and c:

$$\frac{\partial}{\partial\varphi}[\sin^2\varphi(\cos\varphi - \lambda_r\sin\varphi)(\sin\varphi + \lambda_r\cos\varphi)] = 0 \quad (3.61)$$

Hence,

$$\lambda_r = \frac{\sin\varphi(2\cos\varphi - 1)}{(1 - \cos\varphi)(2\cos\varphi + 1)} \quad (3.62)$$

After expanding the fraction, and remembering the trigonometric relations,

$$\begin{cases} \sin(2x) = 2\sin(x)\cos(x) \\ \cos(2x) = 2\cos^2(x - 1) \\ \sin(x) - \cos(y) = 2\cos(\frac{x+y}{2})\sin(\frac{x-y}{2}) \\ \cos(x) - \cos(y) = 2\sin(\frac{x+y}{2})\sin(\frac{y-x}{2}) \end{cases} \quad (3.63)$$

the expression to evaluate the optimum for fluid angle and chord length are:

$$\varphi_{opt} = 2/3 \tan^{-1}(\lambda_r^{-1}) \quad (3.64)$$

$$c_{opt} = \frac{8\pi r}{n_b C_L}(1 - \cos\varphi) \quad (3.65)$$

Albeit it is not essential to detail here the different ways in which Schmitz's formulas are derived, (Okda2015) observes that the 'Schmitz equation for optimum flow angle and optimum chord length gained significant attention in the literature and was used by many authors.'

3.2.4   Glauert Correction

The Fig.3.10illustrates the axial induction starts to deviate for data more than 0.4 and becomes invalid from 0.5 forward. Indeed, what happens is that the assumptions of the momentum theory ceases to be valid for $a > 0.5$. In fact, as the wake velocity U_w is a function of $(1 - 2a)U_\infty$, it becomes zero if $a = 0.5$. This is physically impossible as it requires the storage of the flow exactly on the rotor
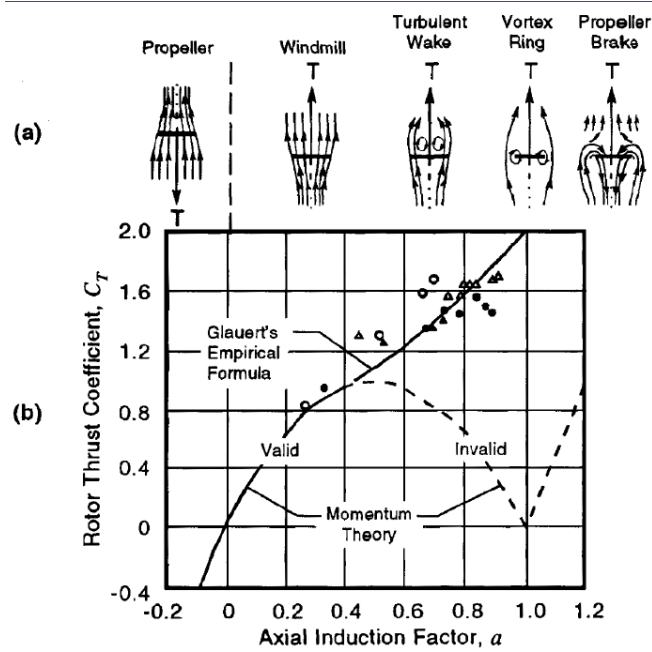
Figure 3.10: Correlation in a rotor among axial induction, flow state and thrust. Source: (Spera2009). The figure shows how the momentum theory diverges from experimental data with a greater than 0.4.

line, as the air has no more forward movement. What actually happens is that the momentum theory ceases to have meaning because at high wind a turbulent wake appears, thereby, a recirculation behind the rotor occurs. Usually empirical relationship between C_T and a comes in force in the region where experience contrasts with the momentum theory. (Glauert1926) proposed his empirical formula that gives a very good approximation with the experimental data, as Fig.3.10confirms.

In the Glauert's empirical formula a has the expression:

$$a = \frac{1}{F}\left[0.143 + \sqrt{0.0203 - 0.6427(0.889 - C_T)}\right] \tag{3.66}$$

where F is the Prandtl's loss factor and its meaning is discussed in Section3.2.5. Besides, C_T derives from:

$$C_T = \frac{F\sigma(1-a)^2 C_n}{\sin^2(\varphi)} \tag{3.67}$$

Another empirical correction is provided by (Spera2009). Thanks to interpolate experimental data from Lock *et al.* 1926, Wilson *et al.* 1976 and Eggleston and Stoddard 1987 from testing wind turbines and helicopters, he proposed a equation valid for the entire range of a, below and above the value of 0.4, as the
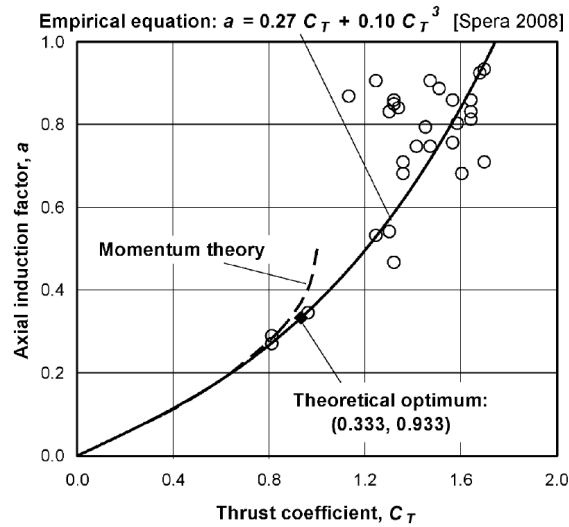
Figure 3.11: Empirical equation derived for calculating an axial induction factor from the rotor thrust coefficient. Source: (Spera2009)

Fig.3.11can show:

$$a = 0.27C_T + 0.10C_T^3 \tag{3.68}$$

where the thrust coefficient C_T has the normalised formulation indicated by (Eggleston and Stoddard 1987):

$$C_T = \frac{T}{\frac{1}{2}\rho A U_\infty^3} \tag{3.69}$$

In Fig.3.11, the 'theoretical optimum' is indicated in correspondence of $(a, C_T) = (0.333, 0.9333)$.

In any case, (Okda2015) notes that 'Spera correction seems to better match the experimental results than the other methods. However, no results are reported in literature for the application of Spera correction in the analysis of the turbine blade performance.' Although other methods have been developed during the last two decades, the Glauret empirical correction keeps to be a valid choice and useful for the scope of this study because it is the most acceptable model in literature.

3.2.5   Tip Losses

The BEM theory needs to be adjusted close to the boundaries as it does not take into account the vortex shifts on the edges.

Fig.3.12shows what happens on the tip vortex moving from Betz's ADT **(a)**, in which the radial flow and the wake expansion are not considered because the rotational component is neglected, towards a limited n_b,**(b)-(d)**. Thanks to the reduction of n_b, the flow tries to jump from one side to the other of the blade as
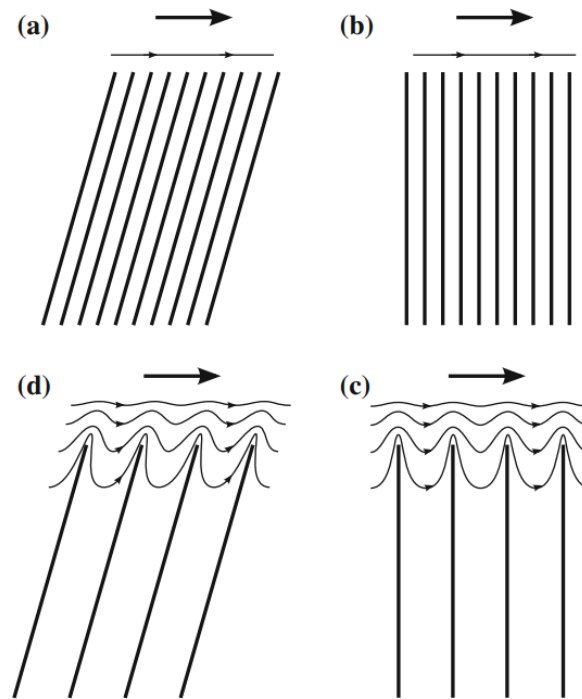
Figure 3.12: Sketch of **(a)** rigid-wake for ideal actuator disc, **(b)** Prandtl's concept reducing the number of blades up to limited order, **(c)**. In **(d)**, explanation of wake perturbation in radial direction along the blade. Source:(Branlard2017)

any more material support are present to confine the flow. Indeed, between the two sides, a pressure difference ΔP is created by the shape of the airfoil: on the top of the blade, there is P_{min} value, and the maximum of relative velocity and vice versa happens below the airfoil. Therefore, in the absence of material, the high pressure side perturbs the low pressure. The axial velocity is affected by a radial component, not foreseen by the BEM theory. Usually, the perturbation involves only the last 10% of the blade radius from the tip. However, it greatly affects the power production as this latter is directly connected to the radius. This effect is denominated *tip losses*.

For the scope of this work, the methods to reduce the tip losses by drawing the shape of the blades differently (e.g. shark blade) have not been considered, preferring to focus on the method developed by Prandtl to 'approximate the radial flow effect near the blade tip which is sufficiently accurate for high tip speed ratios for turbines with two or more blades'[24].

Calling with Γ the bound circulation of a definite n_b, the tip-loss factor F is the ratio:

$$F = \frac{\Gamma}{\Gamma_\infty} \tag{3.70}$$

---

[24](McCosker2012)

where Γ_∞ is the bound circulation in case with an infinity number of blades.

Citing (Spera2009), 'In Prandtl's tip-loss model, the vortex sheets generated by the blades are replaced (for purposes of analysis) with a series of parallel planes at a uniform spacing equal to the normal distance between successive vortex sheets at the slipstream boundary.' Given the definition of Δz as:

$$\Delta z = \frac{2\pi R}{n_b} sin(\varphi) \tag{3.71}$$

where Δz is the axial spacing between planes representing vortex sheets, the tip-losses factor is:

$$F = \frac{2}{\pi} cos^{-1}\left(exp\left[\underbrace{-\frac{n_b(R-r)}{2r sin(\varphi)}}_{f} \right] \right) \tag{3.72}$$

(Spera2009) suggests that 'In the absence of test data on local flow quantities near HAWT blade tips, the Prandtl tip-loss model is recommended. This recommendation is based on the following:

- The Prandtl model predicts a continuous change in circulation, in qualitative agreement with the behaviour of wind turbine rotors.
- Calculations of rotor power and thrust made with the Prandtl model are in good agreement with test data.
- Strip theory[25] calculations made with the Prandtl model show good agreement with calculations made with free wake vortex theory.
- The Prandtl model is easier to program and use.'

3.3   DAWT Blade Element Momentum Theory

Finally, the most common theoretical approach used to design and apply in case of ducted turbines can be properly discussed, reconsidering the example proposed in DAWT classic theory Subsection 3.1.2 after having unveiling the Blade Element Momentum theory, in the previous Section: 3.2.

In fig. 3.13, it is presented the speed triangle on a DAWT and the resulting forces. The main difference respect of bare case is the additional speed-up ratio γ that intensify the normal velocity component.

$$U_{disc} = \gamma(1-a)U_\infty \tag{3.73}$$

---

[25] Also called Blade Element Theory
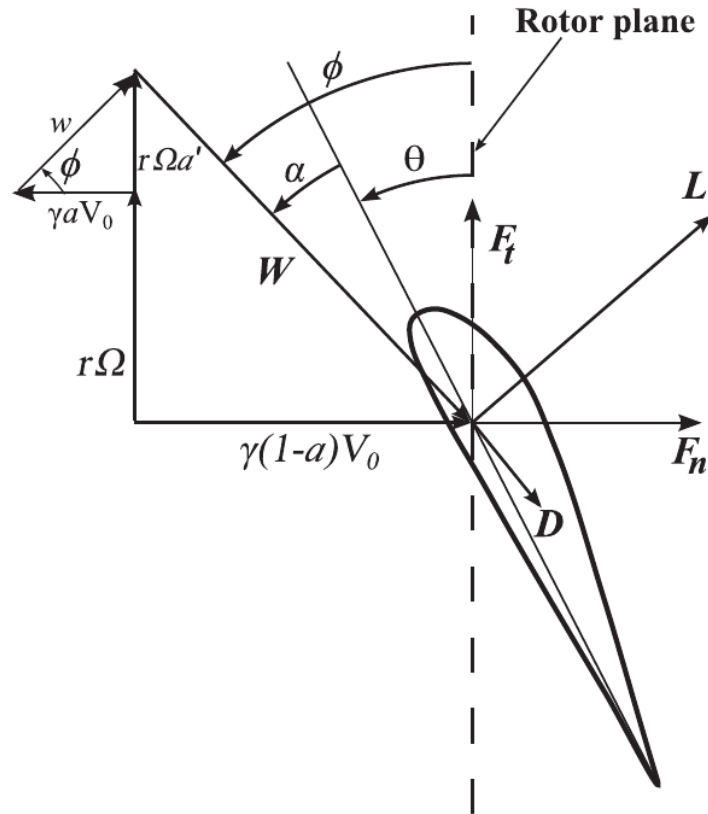
Figure 3.13: Speed triangle in a section of a blade coupled with a diffuser. Source: (Vaz and Wood2016)

Also, U_3, the velocity at the outlet of diffuser[26] is affected by this parameter:

$$U_3 = \beta U_{disc} = \beta \gamma (1 - a) U_\infty \tag{3.74}$$

After the speed analysis, the wake rotation, that has been neglected in Classical Model (see Subsection:3.1.2, but covers a crucial role for power generation, yields to an evaluation of elemental torque - dQ_d, starting from angular momentum equation applied to an infinitesimal area $dA = 2\pi r dr$:

$$dQ_d = 2\gamma a'_d (1 - a_d) U_\infty \rho \Omega r^2 dA \tag{3.75}$$

Where a_d and a'_d are respectively *ducted axial induction factor* and *ducted angular induction factor*.

The similarity respect the bare turbine expression - Eq.(3.33) - can be noticed.

---

[26]U_3 can be visualised in Fig.3.3.

Consequently the torque coefficient, $C_{Q,d}$ can be evaluted as:

$$C_{Q,d} = \frac{dQ_d}{1/2\rho U_\infty^2 dA} = \frac{4\gamma a'_d(1 - a_d)\Omega r^2}{U_\infty} \tag{3.76}$$

Likewise as done for open turbine, the elemental power is computed as:

$$dP_d = \Omega dQ_d = 2\rho\gamma a'_d(1 - a_d)U_\infty\Omega^2 r^2 dA \tag{3.77}$$

Finally, the expression of C_p is deduced as:

$$C_{p,d} = \frac{8}{\lambda^2} \int_{\lambda_{hub}}^{\lambda} \gamma a'_d(1 - a_d)\lambda_r^3 d\lambda_r \tag{3.78}$$

From Fig.3.13, the normal and tangential coefficients can be easily expressed as the result of combinations between lift and drag coefficients in a way that is very similar to the one used before in Section3.2.1.

$$C_{nor,d} = \frac{F_n}{\frac{1}{2}\rho U_{rel}c} = C_l\cos(\varphi) + C_d\sin(\varphi) \tag{3.79}$$

$$C_{tan,d} = \frac{F_t}{\frac{1}{2}\rho U_{rel}c} = C_l\sin(\varphi) - C_d\cos(\varphi) \tag{3.80}$$

In this situation, the flow angle φ is equal to:

$$\varphi = \tan^{-1}\left[\gamma\frac{(1 - a_d)U_\infty}{(1 + a'_d)\Omega r}\right] \tag{3.81}$$

The two ducted induction factors - a_d and a'_d - can be obtained combining different expressions of trust and torque coefficients.

Indeed, the ducted axial induction factor is derivable from $C_{T,d}$ in the Diffuser Classic Theory (see Eq. (3.22)) and $C_{T,d}$ from DAWT BET theory:

$$C_{T,d} = \gamma^2(1 - a_d)\frac{\sigma C_{nor,d}}{\sin^2(\varphi)} \tag{3.82}$$

where $\sigma = \frac{n_b c}{2\pi r}$ is the solidity.

Therefore, a is the solution of:

$$\frac{a_d}{1 - a_d} = \gamma^2\frac{n_b c C_{nor,d}}{8\pi r\sin^2(\varphi)} \tag{3.83}$$

Analogously, the diffuser tangential factor derives from the torque coefficient calculated by the angular momentum (see Eq. (3.76) and the same value expressed

via DAWT BET theory:

$$C_{Q,d} = \frac{\gamma(1 - a_d)(1 + a'_d)r\Omega}{U_\infty} \frac{\sigma C_{tan,d}}{\sin(\varphi)\cos(\varphi)} \tag{3.84}$$

.

Hence, a'_d derives by:

$$\frac{a_d}{1 + a'_d} = \frac{n_b c C_{tan,d}}{8\,\pi\,r\,\sin(\varphi)\,\cos(\varphi)} \tag{3.85}$$

3.3.1 DAWT Glauert Correction

Similar to the bare turbine, the DAWT optimisation can not be properly resolved without applying the Glauert correction to BEM equations. For example, (Liu and Yoshida2015) reports in Fig.3.14that a relevant divergence emerges at $C_{T,d} = 0.6$ between theoretic expectation and CFD results, obtaining by (Hansen et al.2000) simulations. To evaluate this discrepancy, the **effective diffuser efficiency**, $\eta_{efc,d}$ has been used. In his own paper,Jamieson(2008) has applied the ADT approach for a more generic case of a ducted wind turbine, developing the Generalised Actuator Disc Theory (GADT). As it can been considered an extensive case of ADT, the present work does not discuss it in detail, but mentions the efficiency parameters able to indicate how close is a real diffuser machine respect the ideal case. Indeed, $\eta_{efc,d}$ is the ratio between the real diffuser trust coefficient $C_{T,d}$, measured as

$$C_{T,d} = \frac{2\Delta P}{\rho U_\infty^2} \tag{3.86}$$

and $C_{T,d}^{opt}$, valuated by GADT. Obviously, $C_{T,d}^{opt}$ can be considered the theoretical optimum value for a DAWT. Mathematically, the effective diffuser efficiency is:

$$\eta_{efc,d}(a) = \frac{C_{T,d}(a)}{C_{T,d}^{opt}} \tag{3.87}$$

The ratio is function of a_d, as GADT shows that the diffuser trust coefficient - $C_{T,d}$ - is correlated to $f(a_d)(2 - f(a_d))$, where $f(a, d)$ is the unknown function of axial induction function in the far wake. Although $f(a)$ is unknown, three conditions restrict its possible values:

- $f(a_d) = 0$ and $a_d = a_{d,0}$ if no extraction device is installed.[27]
- $C_{T,d} = 0$ and $a_d = 1$, for a full blocked flow.
- $f(a_d) > 0$ and $a_d > 0$ in presence of extraction device that reduces the kinetic energy in the far wake below the ambient level.

---

[27] $a_{d,0}$ is the value in absence of extraction device, accounting only the diffuser geometry.

Therefore, by given to $f(a)$ the formulation $2(a_d - a_{d,0})/(1 - a_{d,0})$, the $C_{T,d}$ becomes:

$$C_{T,d} = \frac{4(a_d - a_{d,0})(1 - a_d)}{(1 - a_{d,0})^2} \tag{3.88}$$

Consequently, the diffuser power coefficient is expressed by:

$$C_{p,d} = \frac{4(a_d - a_{d,0})(1 - a_d)^2}{(1 - a_{d,0})^2} \tag{3.89}$$

as its relationship: $C_{p,d} = (1 - a_d)C_{T,d}$.

In conclusion, the $C_{T,d}^{max}$ in correspondence of $C_{p,d}^{max}$ is equal to 8/9. This value is used as reference in order to determine $\eta_{efc,d}$.
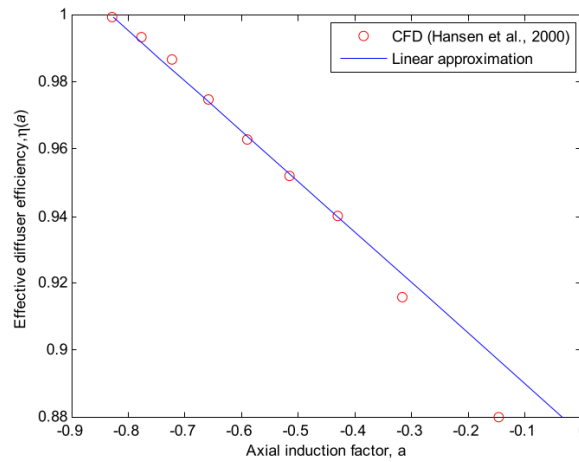
Figure 3.14: Comparison of axial induction factor a_d respect the effective diffuser efficiency $\eta_{d,efc}(a)$, using the GADT by (Jamieson2008) and DAWT CFD simulation, provided by (Hansen et al.2000). Source:(Liu and Yoshida2015).

In reality, as the case described in Fig.3.14indicates, the effective diffuser efficiency is not independent by a_d:

$$\eta_{efc,d}(a) = \frac{C_{T,d}(a_d)}{C_{T,d}^{opt}} \tag{3.90}$$

and, as (Jamieson2008) highlights,'the costant effective diffuser is strictly valid only at the critical condition where $C_{p,d}$ is maximum'.[28]

Lastly, a way to indicate the ratio of mass flow passing through diffuser and open turbine is:

$$\frac{C_{p,d}}{C_{p,o}} = \frac{\dot{m}_d}{\dot{m}_o} = (1 - a_d)\eta(a_d) \tag{3.91}$$

(Liu and Yoshida2015) reaches the conclusion that for the shrouded turbine

---

[28](Liu and Yoshida2015)

'the half far wake induction b (...) can be used as a basic variable for Glauert correction to a in the open flow ADT'. In his own paper, (Liu and Yoshida2015) indicates with b: $a_d - a_{d,0}/1 - a_{d,0}$

Therefore, if the definition of b is substituted into $C_{T,d}$ expression - $4b(1 - b)$ - considering a general case with an effective diffuser efficiency for a DAWT valuated, the new expression of $C_{T,d}$ with the effect of $\eta_{T,efc}$ is:

$$C_{T,d} = \frac{4[a - a_0\eta_{d,efc}(a)][1 - a + [\eta_{d,efc}(a) - 1]a_0]}{(1 - a_0)^2} \quad (3.92)$$

Fig.3.15displays the error, occurring if $\eta_{T,d}$ is neglected. The DAWT Glauert
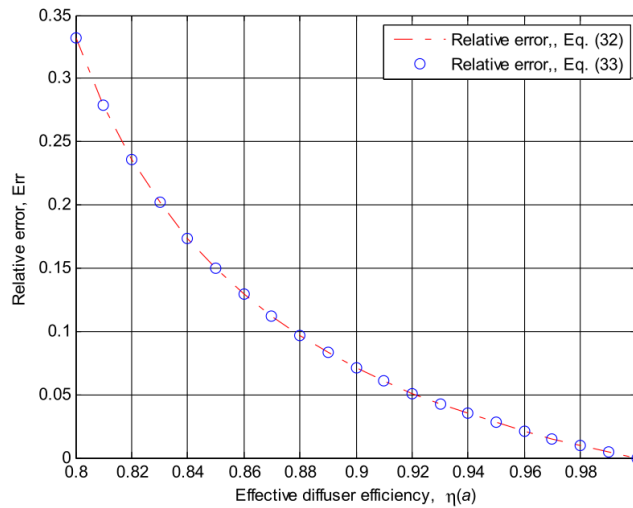
Figure 3.15: Error estimation considering $\eta_{d,efc}$ contribution in C_T

correction, that would be applied, takes, in general, the shape of polynomial function of any order, but first order is the favored by engineers. In the the linear regression, the values at the optimal point (b_{pmax}, $C_{T,d^{pmax}}$) and the cut-off point (b_c, $C_{T,d}^c$) are choosen connected by linear equation:

$$C_{T,d}(b) - C_{T,d}(pmax) = \frac{C_{T,d}(pmax) - C_{T,d}(c)}{b_{pmax} - b_c}(b_{pmax} - b_c) \quad (3.93)$$

where $b_{pmax} = (a_{pmax} - a_0\eta_{pmax})/(1 - a_0)$ and $b_c = (a_c - a_0\eta_c)/(1 - a_0)$[29]. Thus, this conduces to:

$$C_{T,d}(a) = \begin{cases} 4\left[\frac{a - a_0\eta(a)}{1 - a_0}\right]\left[1 - \frac{a - a_0\eta(a)}{1 - a_0}\right] & \text{for } a_0 \leqslant a \leqslant a_o + 0.2(1 - a_0) \\ 0.3504 + 1.4482\left[\frac{a - a_0\eta(a)}{1 - a_0}\right] & \text{for } a_o + 0.2(1 - a_0) \leqslant a \leqslant 1 \end{cases} \quad (3.94)$$

---

[29]$pmax$ represents the point at maximum power and η_c is discrepancy point between the ordinary C_T equation and the Glauert correction

In literature, it is also possible find a quadratic polynomials for turbulent state, see (Liu and Yoshida2015).

3.3.2 DAWT Tip Losses
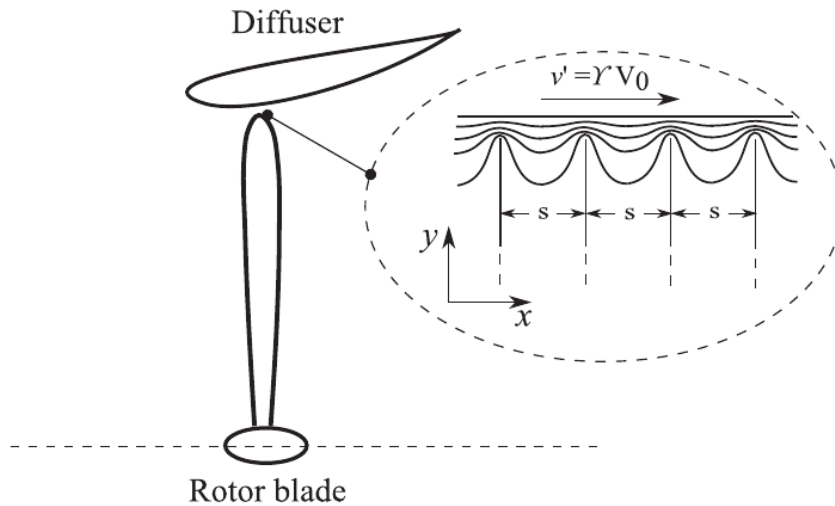
Figure 3.16: Illustration of two-dimensional velocity field around the vortex lines, from: (Vaz and Wood2016)

The Fig.3.16is the starting point to illustrate how the Prandtl's tip losses factor, F, can be reevaluated in case of a rotor coupled diffuser, which clearly reshapes the fluid underneath and the vortex pattern. In accordance with (Vaz and Wood 2016)'s work, it is defined an external velocity between the blade tips and the diffuser, that follows the law $v' = \gamma U_\infty$ [30]. It is worth emphasising that v' depends to speed up ratio,γ.

(Wald2006) dissertation has previously that, in case of same velocity for all fluid standing around the foils, the circulation would be $v's$. The distance between the foils is indicated with s. The perturbation, that involves the vortex, produces a reduction proportional to $2v'(s/pi)\arccos(e^{-\pi\Delta r/s})$. Dividing by $v's$, F can be expressed by:

$$F = \frac{2}{\pi}\arccos(e^{-f}) \tag{3.95}$$

.

The parameter f means $\pi\Delta r/s$, where $\Delta R = r - R$ is the distance between the generic radius r and the blade tip R.

---

[30]In Fig.3.16, U_∞ is indicated with V_0.

The last step is made considering from Fig.3.13that

$$\sin(\varphi) = \gamma(1 - a_d)\frac{U_\infty}{U_{rel}} \tag{3.96}$$

and, therefore, f in case of DAWT can be rewritten as:

$$f = \frac{n_b}{2}\frac{U_{rel}(R - r)}{r\gamma(1 - a_d)U_\infty} \tag{3.97}$$

Eventually, (Vaz and Wood2016) notes two relevant observations for the Prandtl's tip losses factor applied to DAWTs: 'First, the diffuser is assumed to induce a circumferentially uniform axial flow, but no azimuthal flow, through the rotor. This axial flow should reduce the tip loss, as should the proximity of the blade tip to the diffuser wall, in a way that is not possible to incorporate into f as defined above. Second, there should be different tip loss factors for the axial and circumferential motion.'

3.3.3 DAWT Optimisation Algorithm

As in the optimisation process, the goal is to work as close as possible with values of $C_d \approx 0$. Although the design point is near the stall condition, in the first approximation, the drag contribution can be neglected, preferring to start the process with Eq.(3.78). Therefore, the optimisation means maximising $\gamma a'(1 - a)$. In accordance with (Vaz and Wood2016), this leads:

$$\frac{d}{da_d}[\gamma a'_d(1 - a_d)] = \gamma\left[(1 - a_d)\frac{da'_d}{da_d} - a'_d\right] = 0 \tag{3.98}$$

The expression can be simplified, considering $\gamma \neq 0$ and also γ is an independent variable respect a and a'[31]:

$$(1 - a_d)\frac{da'_d}{da_d} = a'_d \tag{3.99}$$

When the turbine works in stall condition, Eq.(3.98) becomes worthless as the C_d cannot be neglected anymore.

In case of open turbine, to apply this optimisation procedure, (Wood2015) noticed that it is required that λ is greater than 1, otherwise 'the behaviour of the induced velocity field seems to be heavily dependent on the radius'[32]. Hence, when $\lambda > 1$, a_d and a'_d have their optimum bond if:

---

[31]This equation is also correct with open turbine
[32](Vaz and Wood2016)

$$a'_d = \frac{(1 - 3a_d)}{(4a_d - 1)} \tag{3.100}$$

This relationship is obtained by Eq.(3.81) rewritten after the derivation from φ:

$$\lambda^2 a'_d (1 + a'_d) = \gamma^2 a_d (1 - a_d) \tag{3.101}$$

If you differentiate the latter one equation with respect to a_d:

$$(1 + 2a'_d) \frac{da'_d}{da_d} \left(\frac{\lambda}{\gamma}\right)^2 = (1 - 2a_d) \tag{3.102}$$

The Eq.(3.101), already presented by (Glauert1983) in open turbine case, is obtained by combining Eqs.(3.99),(3.102) and (3.101).

As last step, studying the DAWTs, the optimum relationship between λ and a_d is reached applying Eq.(3.101) together with (3.100):

$$16a_d^3 - 24a_d^2 + \left[9 - 3\left(\frac{\lambda}{\gamma}\right)^2\right]a_d + \left(\frac{\lambda^2}{\gamma}\right) - 1 = 0 \tag{3.103}$$

When λ is greater, $a_d \to 1/3$ by Eq.(3.103).

The algorithm, described underneath, is workable only when the lift and drag coefficients of the blade are available, it needs those input:

- Number of section N_s: the algorithm starts from the tip section and works up to cover the last hub section.
- Operating Condition: $U_{\infty|design}, \lambda_{|design}$.
- Blade and diffuser geometry: r, γ
- Airfoil coefficients: $C_{L|(\alpha_{opt})}, C_{D|(\alpha_{opt})}$

in addition to the initial values for a_d and a'_d: i.e. $a_d = 1/3$ and $a'_d = 0$ to compute iteratively the chord and twist angle distributions.

Algorithm 1 DAWT optimisation

---
  for $i = 1 \rightarrow N_s$ **do**
    while $error > TOLERANCE$ **do**
      $iter = iter + 1$
      Compute φ, by Eq.(3.81);
      Compute C_n and C_t, by Eqs.(3.79) and (**??**);
      Compute the optimum values for a_d and a'_d, by Eqs.(3.101) and (3.103);
      Compute the optimum cord c, by Eq.(**??**);
      Compute the optimum twist angle $\theta = \phi - \alpha$;
      Compute the new value for φ, by Eq. (3.81)
      Compute $error = |\varphi_{iter+1} - \varphi_{iter}|$
    end while
  end for

3.4 Vortex Theory

The vortex wake method uses the Kutta-Joukowsky theorem and the Biot-Savart law to elaborate the local thrust and the local torque. In the Vortex theory, 'each of the rotor blades is replaced by a lifting line about which the circulation is associated with the bound vorticity, and a vortex sheet is continuously shed from the trailing edge'[33], see Fig.3.17.
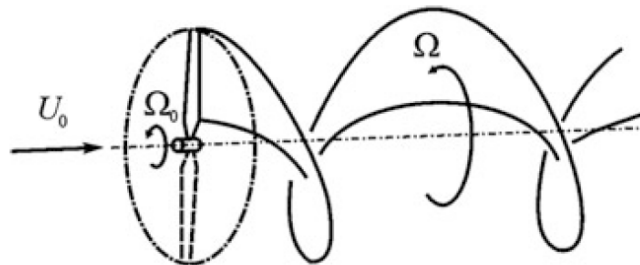
Figure 3.17: Sketch of helican screw surface corrisponding to the ideal wake behind a rotor blade. Annotation: Ω_0 is the rotational speed of the blades, Ω is the angular speed of the wake vortex. Source (Sørensen2016)

In accordance with the vortex theory, the local lift acting on the blades has produced by the bound vorticity. The mathematical vorticity definition is $\omega = \nabla \cdot U$, that, if it is integrated around a surface S or over a close curve C, allows to evaluate the total vorticity or circulation Γ:

$$\Gamma = \oint_S \omega \cdot ds = \oint_C U \cdot dC \tag{3.104}$$

---

[33](Sørensen2016)
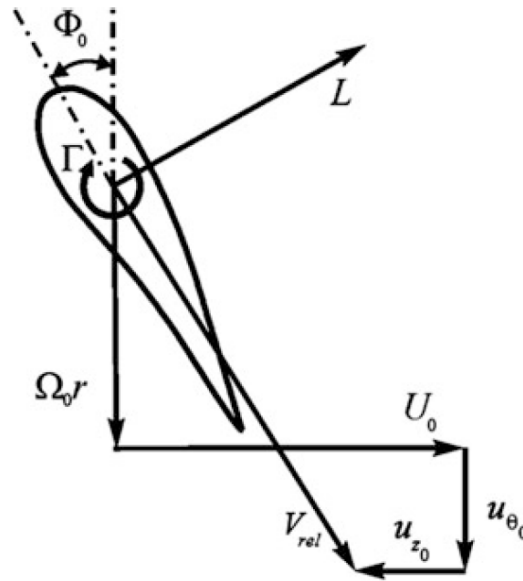
Figure 3.18: Vorticity and speed triangle on the rotor plane. Annotation: $u_{\theta_0} = U_n$ and $u_{z_0} = U_t$. Source:Sørensen(2016)

Stokes' theorem provides the equivalence between the two integral loops. Whereas the vorticity is a flow characteristics characteristics, the circulation is an integral property.

Using the Kutta-Joukowsky theorem, the lift force per unit of length on a blade element is triggered by the inlet velocity and the bound vorticity around the blade in accordance with:

$$L = \rho \left(U_{rel} \times \Gamma \right) \tag{3.105}$$

Proceeding in similar way respect the others theory, the induced velocity can be divided in a radial - U_n and tangential - U_t - components.

Hence, thanks to the support of Fig.3.8, the local trust - dT - and the local torque - dQ - are:

$$dT = \rho\Gamma(\Omega_0 r + U_n)dr \tag{3.106}$$

$$dQ = \rho\Gamma(U_0 r - U_t)rdr \tag{3.107}$$

The overall thrust and torque expressions come out from the sum of the integral along each blade:

$$T = n_b\rho \int_r^R \Gamma(\Omega_0 r + U_n)dr \tag{3.108}$$

$$Q = n_b \rho \int_r^R \Gamma(U_0 r - U_t) r \, dr \qquad (3.109)$$

The optimisation process is made looking for the optimal Γ and the induced velocity components in the wake. The consequent system of lifting lines on the wake are resolved through the Biot-Savart law.

In fig.**??**, the vortex downstream the blades are represented around the rotating wake. This approach is usually divided into three models:

- Rigid wake;
- Prescribed wake;
- Free wake model.

The first is the less accurate as it does not consider the wake spread downstream. Therefore, the prescribed wake model increases the correctness thanks to experimental support. The latter one, the free wake, gives the highest quality results computing the whole flow field at the price of greatly increasing the amount of calculations to be carried out, as is usually the trade-off in such a study. According to (Wang2012), 'Vortex wake methods are reckoned to be more accurate than BEM method and should play a major role in future engineering applications with the increase of computer power'. Specific texts on this subject can be consulted for a deeper understanding of the vortex theory, while the thesis intends to be focused on BEM methods and the following CFD analysis.

Table 3.1: List of Chord Length Distributions

No.	Equation
1	$C(r) = \dfrac{R}{n_b C_L \lambda}\left(1.868 + \dfrac{5.957}{\lambda_r} - \dfrac{3.1}{\lambda_r^2} + \dfrac{0.54330}{\lambda_r^3} - \dfrac{0.2917}{\lambda_r^4}\right)$
2	$C(r) = \dfrac{8\pi r \cos(\varphi)}{3 n_b}$
3	$C(r) = \dfrac{8R}{9\lambda_{0.8}}\left(2 - \dfrac{\lambda}{\lambda_{0.8}}\right)\dfrac{2\pi}{C_L \lambda n_b}, \ \lambda_{0.8} = \lambda_r$ at $r = 0.8R$
4	$C(r) = \dfrac{16\pi R^2}{9 n_b C_{L\mid design}\lambda^2 r}$
5	$C(r) = \dfrac{2\pi r}{9 n_b}\dfrac{8}{C_L}\dfrac{U_\infty}{U_{rel}}$
6	$C(r)_{opt} = \dfrac{8 a r \sin^2(\varphi)}{(1-a) n_b C_n}$
7	$C(r) = \dfrac{8\pi r}{n_b C_L}$
8	$C(r) = \dfrac{8\pi r \sin(\phi)}{3 n_b C_L \lambda_r}$
9	$C(r) = \dfrac{16\pi R}{9 n_b C_{L\mid design}\frac{1}{\lambda\sqrt{\lambda_r^2+4/9}}}$
10	$C(r) = \dfrac{16\pi r}{n_b C_L}\sin^2(\tfrac{1}{3}\tan^{-1}\tfrac{1}{\lambda_r})$
12	$C(r) = \dfrac{8\pi r F \sin(\varphi)}{n_b C_L\left(\frac{\lambda_r+\tan(\varphi)}{1-\lambda_r\tan(\varphi)}C_D/C_L\right)}$

The Table 3.1 harvests eleven different calculation methods to valuate the optimum twist angle and chord length distribution. The list is set by (Batu and Lemu 2020) and is collected up to 19 methods, but the first 11 are enough to argue for this thesis. (Batu and Lemu 2020) proposes a comparison taking in account the following design criteria for a HAWT blade:

- Design wind speed $U_\infty = 12.62$ [m/s]
- Blade twist angle fixed at $\theta = -2°$
- Rotor radius $R = 4.95$ [m]
- Hub radius $r = 0.15$ [m]
- Number of blade $n_b = 3$
- Design tip speed ratio $\lambda = 7$
- Airfoil NACA 4415, selected because of a maximum of ratio C_L/C_D for each radial segment of the blade
- Using Qblade software[34] the optimum angle α is at $7°$, by whom the optimum coefficients: $C_{L|opt}(7°) = 1.20423$ and $C_{D|opt}(7°) = 0.01162$

According to (Okda 2015), the following considerations can be expressed for the aforementioned formulas:

(No.1): Developed by (Raju 2011) and (Edon 2007) without proof about how has been obtained, it doesn't consider the drag effect;

(No.2): (Ingram 2011) proposes the equation starting by the design case of ideal blade with a flow angle calculated thanks to

$$\varphi = 2/3 \tan^{-1}(1/\lambda_r) \tag{3.110}$$

(No.3): (Burton et al. 2011) suggests a method to calculate directly the chord linear distribution and also the flow angle equal to

$$\varphi = \tan^{-1}\left(\frac{(1 - \frac{1}{3})}{1 + \frac{2}{3\lambda_r^2}} \frac{1}{\lambda_r}\right) \tag{3.111}$$

where the 1/3 indicates the $a_{|opt}$ as ADT predicts;

(No.4): (Jamieson 2011) produces an expression of optimum chord when C_L is set at the design condition;

(No.5): (Hau 2013) and also (Schubel and Crossley 2012) give a formula without considering the wake rotation neglecting the tangential component;

---

[34]Qblade is an open-source tool developed by the Berlin Institute of Technology, using by (Batu and Lemu 2020) to simulate the design output of each forumula.

(**No.6**): (Hansen2008) provides a solution as function of the optimum value of a and a'. C_n is always the normal force coefficient: $C_n = C_L \cos(\varphi) + C_D \sin(\varphi)$;

(**No.7**): Following the assumptions of Schimitz's formula including the tangential component. Unless this,(Duran2005) and (Manwell et al.2009) prefer to keep a constant at $1/3$ and express the optimum flow angle

$$\varphi = 2/3 \, \tan^{-1}(\lambda_r^{-1}) \tag{3.112}$$

(**No.8**): Besides, (Manwell et al.2009) presents an expression without wake rotation;

(**No.9**): (Gundtoft2009), backed by ADT for $a = 1/3$, shows a flow angle equal to what expressed in Eq. (3.112);

(**No.10**): (Schaarup and Krogh2001) from the Wind Energy Department in Risø, Denmark is based on Schimitz's work, including tangential componenet and valid for optimal φ, calculated with Eq. (3.112);

(**No.11**): Eventually, (Maalawi and Badawy2001) proposed a solution starting from Glauert's correction without omitting the drag aspect and including the tip losses parameter F:

$$F = 2/\pi \, \cos^{-1}\left(\exp\left(-\frac{n_b(R-r)}{2r\sin(\phi)}\right)\right) \tag{3.113}$$

Even if this solution has great advantages to incorporate F and C_D, it also increases the manufacturing cost due to three reasons, all of which are caused by the high chord lengths near the hub: $r/R \leqslant 0.2$. The first is the complicated shape required by the mould used to realise the blades. Second, the additional weight is not justified by an increase in the power produced, which is limited to $0.1 \leqslant r/R \geqslant 0.4$. Eventually, the weight increase affects the cost of all the other components of a turbine (i.e., shaft, gearbox, etc.) and all this has to be matched by more power achieved, which is hard to get near the hub.

3.4.1 Equations Comparison

As already known, a and a' have optimal values at $1/3$ and $1/4$, respectively. These optimum values are kept constant along the blade - greatly facilitating the study -, but the simplification doesn't consider the effect of the diffuser and γ that create perturbation radially. Of course, the radial effect makes a stronger effect in off-design. The chord optimisation is strictly connected to optimise the twist

angle, which is easily calculated through Eq.(3.112) valid for each local speed ratio, depending on the radius and U_∞ in design condition[35]. Firstly, it is necessary to clarify that the comparison between the methods, recapped in Table3.1, come out considering the values of the inducted factors[36] are kept constant at the optimum as described in the previous sections (see3.2.1, or rather 1/3 for a and 1/4 for a' respectively.

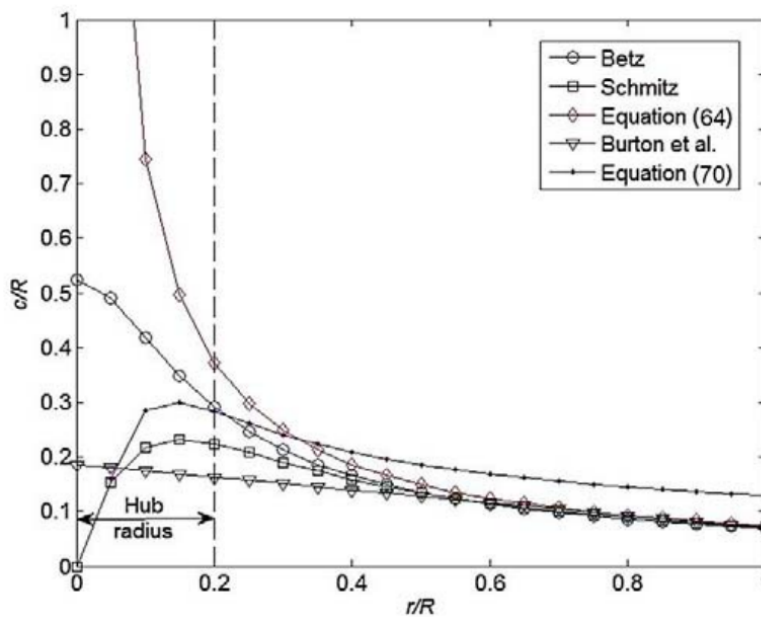The comparison was made by (Okda2015) by numerical calculation.

Figure 3.19: Comparison of chord distribution calculated by five methods for n_b = 3, λ = 5,α = 7° and $C_{D|design}$ = 1. Annotation: In Tab.3.1, Equation (64) refers to (Jamieson2011) [4], Burton et al. refers to [3] and Equation(70) refers to (Raju2011) [1]. On x-axis r/R represents the ratio between the radius and tip radius, while on y-axis c/R is the ratio between the chord length and tip radius. Source: (Okda2015).

In Fig.3.19, five different formulas from Tab.3.1are compared by calculating the chord distribution for a specific blade. In fact, on the x-axis, the r/R ratio normalises the radius of the blade with respect to the tip radius, while on the y-axis, the ratio between c and R corresponds to a specific point along the blade. It is immediately evident that the output described by Equation (64) of (Jamieson 2011)[4] increases the manufacturing cost due to the greater chord size at the root of the blade. However, its behaviour is similar to that of the others close to the tip. The solution provided by (Raju2011) [1] - called Equation (70) on the charts - shows a significant divergence with respect to the other, especially near the hub region, where the chord is larger compared to the other methods.

---

[35]In the speed ratio, there is also the contribution of the rotational speed, ω:it can be considered constant, especially if the control system belongs to fix speed group.

[36]i.e.,a and a'

Even in the range $1 \leqslant r/R \geqslant 0.4$, Betz and Schmitz have similar characteristics, but, in general, Schmitz gives better performance. The advantages of Schmitz's formula result in taking into account wake rotation without the approximation that (Burton et al.2011) otherwise prefers. Moreover, the chord output at the hub radius is compatible with limited-cost production.
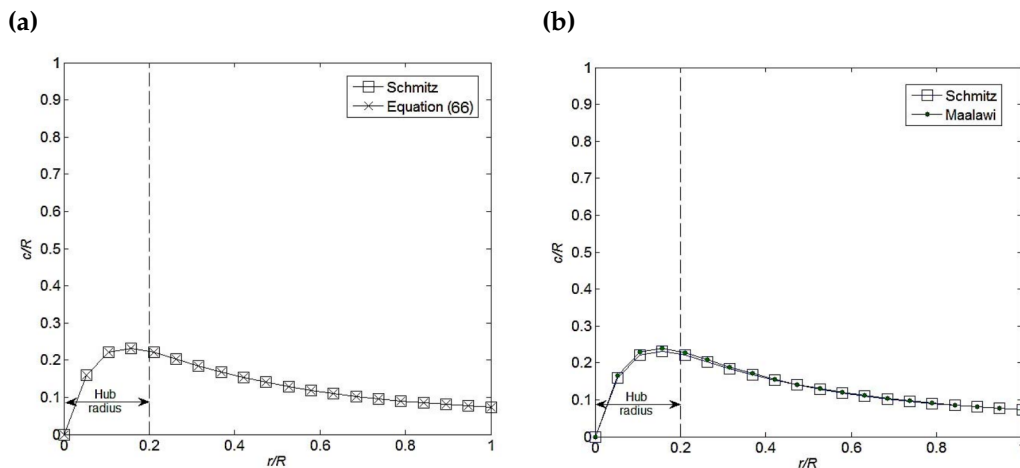

Figure 3.20: (a) Comparison of the chord distribution calculated using the Schmitz method and Kulunk equation(3.114) (annotation: called Equation (66) on the graph) for $n_b = 3$, $\lambda = 5, \alpha = 7°$ and $C_{D|design} = 1$ using the optimal flow angle according to Eq.(3.112). Source:(Okda2015). (b) Comparison under the same conditions between Schmitz's formula and Maalawi's equation [11]. The drag is considered with a glide ratio $C_L/C_D = 10$. Source:(Okda2015)

The comparative benefit in (Burton et al.2011)'s proposal is a consequence of the reduction of material in the root region. All of this comparison is more valuable in terms of production costs. If one looks at the power production, which mainly involves the upper part of the blade, the differences between the various formulations become thinner.

(Kulunk2011) obtained a formulation similar to the Maalawi equation [11] [37] omitting the drag aspect.

$$C(R) = \frac{8\pi r F sin\varphi_{opt}(cos\varphi_{opt} - \lambda_r sin\varphi_{opt})}{n_b C_{L|design}(sin\varphi_{opt} + \lambda_r cos\varphi_{opt})} \qquad (3.114)$$

where φ_{opt} is the optimal flow angle from Eq.(3.112), $C_{L|design}$ is the lift coefficient under the design condition and the ratio C_L/C_D is the maximum.

When comparing the plotsa, where drag is omitted, andb, no visible difference can be seen near the tip and is almost negligible close to the hub. However, Maalawi's formula is competitive with respect to Schmitz's equation, even with a

---

[37]In reference to the Tab.3.1

'glide ratio of as low as 10 which is one order of magnitude less than actual values encountered in practice'[38].

A good summary of the conclusion for this comparison is condensed by (Okda2015): 'The blade geometry obtained from Schmitz method is not only an optimum one, but it produces a good compromise between performance and stiffness at the inboard of the blade'. The optimisation via BEM theory is firstly a flow angle optimisation and, by that, a chord length optimisation. Hence, the optimum flow angle at certain radius allows one to optimise the chord length at the same radius.

---

[38]Okda(2015)

Chapter 4

DAWT CFD Analysis

4.1 DAWT Design

4.1.1 CFD Objective

The present Chapter is focused on how the chord distribution sways influences the performance of ducted turbines, highlighting the connection between the chord distribution and the augmented velocity, and, therefore, the relevance to take into account the augmentation during the DAWT design process. The effect can be demonstrated comparing different design choices thanks to a computational analysis and confronting the outputs with respect to a well-thought selection of wind turbines on the market. Also, the comparison aims to consider the possibility of a reduction of machine size keeping similar, or even better, power output. Unfortunately, as already mentioned, nowadays there aren't DAWT on sale, but it is possible to look at wind turbines, that operates in the same range as the turbines under CFD analysis. After a research about which kind of open turbines are currently on the market, the power curve[1], that should be overlapped by the present study is obtained, keeping fixed the maximum diameter at $R = 0.4m$. Also, the diffuser shape is kept fixed and uses the geometry, called Ellipsis 135, provided by Prof. Pavesi's research group. The diffuser rendering is presented in Fig.4.10b

Getting started, the design work consists of developing the blade shape through the software GUI BEM specifying the boundary conditions, one of which is the design wind velocity, namely the undisturbed wind speed, U_∞. As the exact augmentation of wind speed between the diffuser inlet and the rotor is initially unknown, two different values of U_∞, $U_\infty^8 = 8$ m/s and $U_\infty^{10} = 8$ m/s, have been selected based on the following reasoning. Indeed, the wind velocity,

---

[1] The power curve for wind turbines lays out the wind speed on x axis and the power output on y axis.

Figure 4.1: Rendering of diffuser Ellipsis 135

set for design work, is decided after a probabilistic study of wind distribution, specifically adapted for the location where the machine should be installed. The design velocity is chosen as the velocity with the highest probability to maximize the energy output over one year, but, off course, in case of open turbine the choice is made only thanks to wind data without other consideration. Contrarily, designing a ducted turbine, it is relevant for better optimisation, considering the back pressure contribution.

The wind velocity has only the axial direction before interacting with the diffuser, that modifies the velocity orientation, generating also tangential components, which have not been computed analytically prior to computational analysis. Consequently, in first approximation, the velocity vector at the inlet is indicate in module and direction only with axial component, letting to computational simulation the development of the other velocity components.

The major decision that has to be taken for designing a DAWT is how to consider the diffuser presence. Two approaches are possible:

- **Distinct Design**: it is the most often adopted approach. The blade design is made neglecting interaction with the diffuser. Its presence becomes relevant only during the CFD phase, where the interaction between blades an diffuser

is simulated. In this way, the diffuser influence cannot properly spread its advantage by designing a blade specific target for the velocity speeding up, specifically close to the tip.

- **Integrate Design**: the diffuser and the blades are developed together thanks to an integrated design. In this case, the cross-section velocity profile in front of the blade needs to be evaluated in accordance with the flow acceleration along with the radial component. Following this approach and using the same equation to calculate the chord length distribution, the cord shape could be larger close to the tip as the inflow velocity is higher.

In the *distinct design*, the undisturbed input velocity is decided to be U_∞^8, looking only at positioning the turbine in the best range to produce energy based on probabilistic studies about where the machine should operate.

In contrast, for the integrated design, the second undisturbed input velocity is set at U_∞^{10} as a way to take into account the speed-up contribution (solely in axial direction) already during the design procedure. This choice has effect to the chord distribution due to the aforementioned interconnections between parameters. The design procedure follows the optimisation algorithm aligned with BEM theory and using Maalawi's formulation for the chord distribution, that is influenced by U_∞ via Re definition.

Therefore, the simulations, which are presented, have taken into consideration wind turbines assembled applying both approaches described. All the three key parts (hub, blade, diffuser) are merged in one single mesh to run CFD simulation. Although the computational workflow is identical, the input files are different due to distinctive design approaches. After the design work has been finalised for both selections, a CFD workflow of blades profiles has been developed, via ANSYS suite. The CFD results has been compared with BEM results providing considerations about enhancing of inlet velocity.

In this research, the chord distribution has derived from Maalawi's formula because it give more confidence than the others formulation to improve the turbine performance, as illustrated in Sec.**??**. The role of chord distribution is emphasised under this kind of comparison as the other parameters are kept constant. One goal is to show that the paring between turbine and diffuser provides same performance or even better comparing to machines that have equal or greater radius. It is clear that the comparison is made referring to blades radius without considering the diffuser size. Obtain experimental acknowledgement can allow to build wind turbines smaller able to sustain the same loads of those that are currently marketed.

On the market, there are already some available products, that work at the same operational range without having a shrouded around the blades. The fol-

lowing list presents three of micro wind turbine, that present work aim to match and possibly improve. Operationally, the rated power target is $400 - 500$ kW, covered by the micro wind turbine described in the following list:

- Rutland 1200[2] is produced by the UK company Marlec and have a clear application in supplying standalone energy on boats.

Figure 4.2: Image of Rutland 1200 wind turbine. Source: Marlec website (see note[2])

- Air X Marine [3] by the USA company Primus Wind Power. For example, It can be used to provide energy to telecommunications hub.

Figure 4.3: Image of Air Marine X wind turbine. Source: Primus Wind Power website (see note[3])

- HY 400[4] by the Chinese company HY ENERGY. Useful as electric source for public lighting.

In the table below the interesting features of selected turbines:

Besides, the charts below shows their power curve:

---

[2]https://www.marlec.co.uk (last access: 1 August 2022)
[3]https://www.primuswindpower.com (last access: 1 August 2022)
[4]http://www.hyenergy.com.cn (last access: 1 August 2022))

Figure 4.4: Image of HY 400 wind turbine. Source: HY Energy website (see note[4]

Table 4.1: Commercial Wind Turbines Features

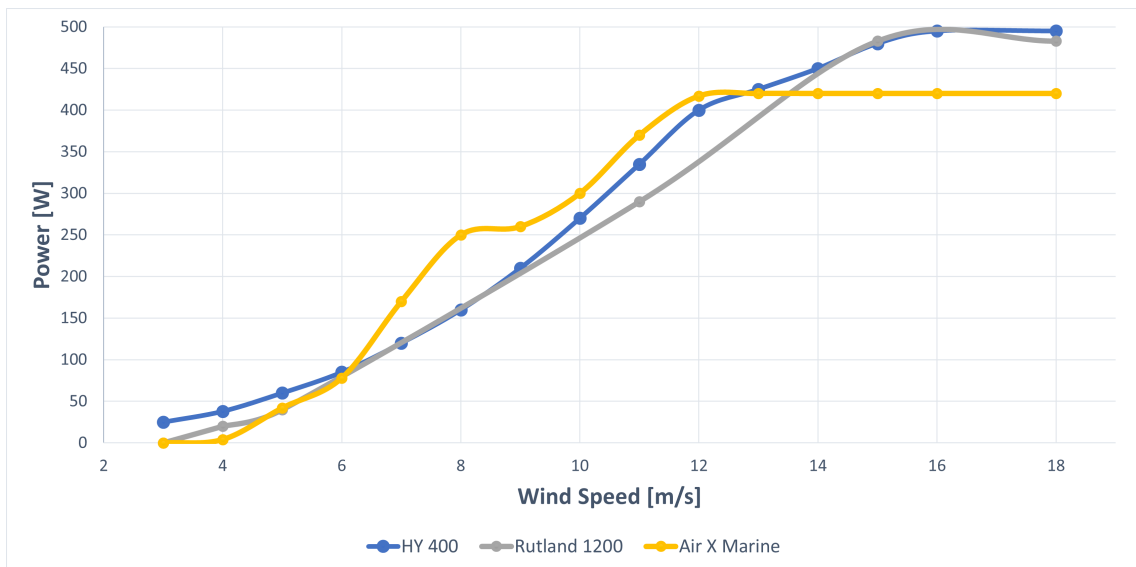| Turbine Features	Rutland 1200	Air X Marine	HY 400
Radius [m]	0.62	0.585	0.775
Swept Area [m^2]	1.2	1.08	1.89
Net Weight [kg]	7.8	6	22
Blades	3	3	5
Cut-in [m/s]	2.5	3.6	2.5
Cut-out [m/s]	>15	~50	~50
Rated Velocity [m/s]	15	12.5	12
Rated Ω [rpm]	500	500	750
Rated Power [W]	483	400	400

Figure 4.5: Selection commercial turbines power curve

Some marked wind speeds have been selected for CFD simulation to to limited constrains in CFD time consuming. The results have been used to extrapolate the entire turbines power curves and compare with the commercial alternatives. Therefore, both configurations have been tested via CFD in the entire operability range from cut-in velocity (4 m/s) to cut-off velocity (16 m/s) for the following U$_\infty$

Table 4.2: Velocity Range

| 4 m/s | 5 m/s | 6 m/s | 8 m/s | 10 m/s | 12 m/s | 14 m/s | 16 m/s |

inlet:

Another purpose behind conducting simulations is to look at the accordance between the algorithm and the simulations. Hence, the areas where the blade doesn't perform as expected, especially in terms of pressure, can be individuated to suggest how to improve the chord distribution.

4.1.2 Design via GUI BEM

GUI BEM is an executable application running on MATLAB interface and developed by Turbomachinery and Energy Systems Group (TES)[5] at the Department of Industrial Engineering of the University of Padova and is supervised by Prof. Giorgio Pavesi. The group is currently conducting research in the following fields:

- Encourage the integration of renewables through extension of the hydraulic turbine operating range to provide electrical power system flexibility and stability;
- Numerical tool to study cavitation, especially in Kaplan turbines;
- Electrical Energy Storage Technology
- Power Plant Dynamic Modelling and Live Cycle Assessment;
- Development of Shrouded Wind Turbines with Wind-Lens Technology.

The GUI BEM objective is to elaborate the blade coordinates for an optimal design configuration of bare or shrouded HAWT, optionally starting from a wind analysis of the site where the wind data have been collected through a specific instrument like ultrasonic anemometer. In an apposite section, the wind data set[6] is computed to evaluate the Weibull wind and energy probability density functions, that yield to individuate the optimal design velocity,U_∞. The design velocity has to be in line with the wind speed that gives the highest probability of extracting the utmost energy at that specific site and is clearly very often shifted with respect to the highest measured wind speed. In fact, the correct choice of U_∞ is given by the combination of probability curve and power curve to answer the question of which is the wind speed that lasts for as long as possible and, at the same time, is likely to provide the greatest amount of energy.

---

[5]https://research.dii.unipd.it/tes/(last access: 1 August 2022)

[6]Often the wind data corresponds to the measurement of wind speed and wind direction taken over an entire year with a frequency no shorter than 1 minute.
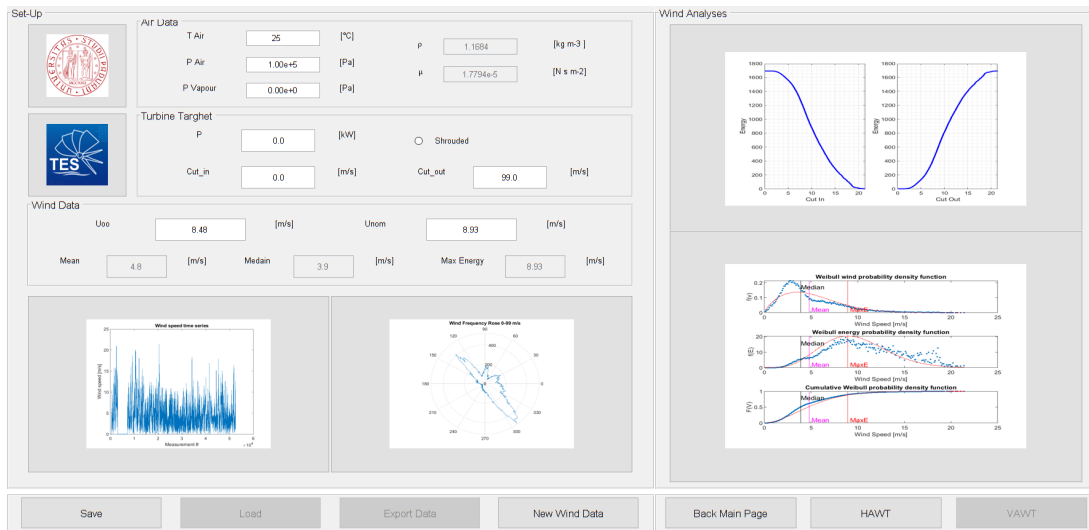
Figure 4.6: GUI BEM wind analysis about measurements of a generic site. The core information of Weibull functions is on the left. The Max Energy red line indicates the wind speed associated with the maximal energy production.

Figure 4.7: Screen of HAWT GUI BEM interface

Fig.4.6shows the wind analysis output, which could be directly transferred to the next section about HAWT configuration.

The HAWT configuration, in Fig.4.7, is the heart of GUI BEM tool: a user interface where the operator can set up all the parameters to initialise the algorithm. The interface is organised in parts with the following features:

- *Air Data*: Information about air properties like temperature, pressure and vapor.
- *Wind Data* of U_∞ - the undisturbed wind speed - and U_{nom}, the selected design velocity in accordance with wind analysis previous done.
- *Turbine Target* explicit the rated turbine power.

- *Turbine Pre-Data* is the set of initial values that characterise the turbine: C_p,λ,ω - rotational speed in Hr and in rpm.
- *Tip Losses* part indicates how the algorithm have to handle the tip losses. The easier solution is, of course, not to consider them at all. For a more precise analysis, a Prandtl correction (see Eq. (3.72)) can be imposed. This selection has been the preferred in this thesis, although other options, like Glauert or Shen Correction are available.
- *Hub Losses* allows taking into account the losses that occur in hub region.
- *Brake Correction* is a set of 1D equations capable of evaluating turbine performance in terms of a and a'
- *3D Correction* is a model for a solution of a simplified form of the 3D boundary layer equations on a rotation blade.
- *Geometry* defines the turbine size and all geometry parameters, including the method for calculating the chord distribution.
    - *Turbine Data* sets the hub and tip radius together with the number of blades. A new interface, specific for the ducted turbine (displayed in Fig.4.8), can be loaded for developing a shrouded solution. The *tip_gap* button defines the distance between the tip of the blade and the diffuser:
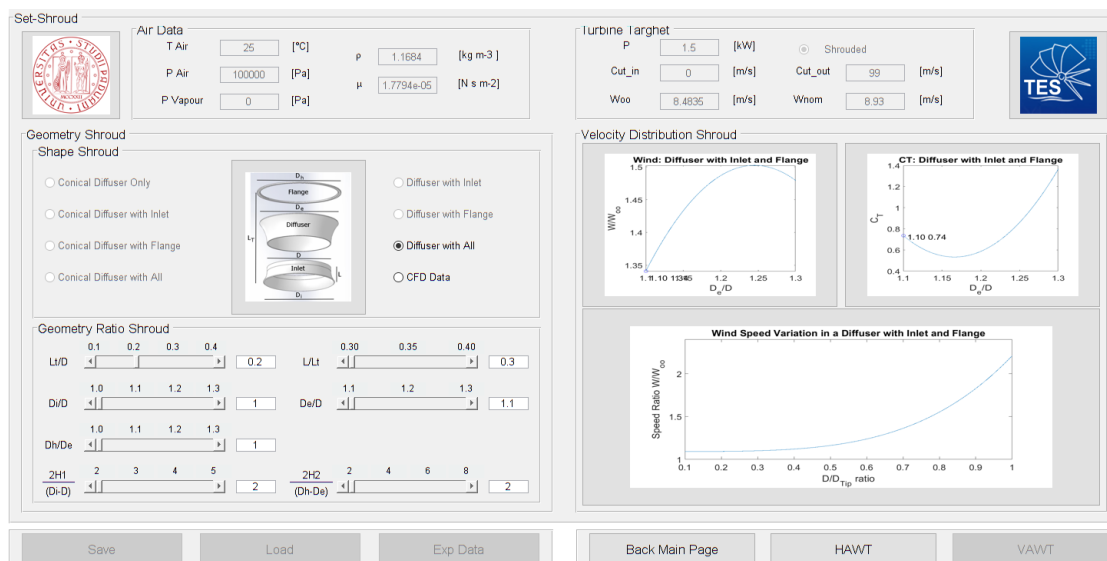

Figure 4.8: Screen of DAWT GUI BEM interface

- ∗ ***Geometry Shroud*** set the shape of the diffuser, essentially due to the layout of the ratios between sizes: D_i inlet diameter, D_e exit diameter, D diameter, L diffuser length. Alternatively, CFD data can be imported.
- ∗ After changing the ratios, the expected results inside the diffuser, in terms of speed ratio and C_T, are displayed in the ***Velocity Dis-***

>> *tribution Shroud* charts.

- – *Wing Profile Type* selects the type of airfoil the solver has to use for shaping the blade. A specific parenthesis about airfoil is here:3.2.1.
- – *Chord Distribution* defines the method to select the optimum chord length for each radius, a very interesting features for the present work. Examining in further detail:

  * *Betz* is the simplest and is in accordance with No. 5 of Tab.3.1: $c_{opt} = \frac{2\pi r}{n_b} \frac{8}{9C_l} \frac{U_\infty}{\lambda U_{rel}}$. The Betz methods are good mainly when drag region and tip losses can be neglected;
  * *Schimitz*'s formula is equal to No. 10 of the Tab.3.1;
  * *Lakshini* corresponds to No. 4 of the Tab.3.1;
  * *Maalawi* uses equation No. 11 of the Tab.3.1;
  * *Raju* applies formula No. 1 of Tab.3.1;
  * *Linear* approaches the problem through a simple linearisation.
  * *GP* specifically development by Prof. Giorgio Pavesi;
  * *Data Input* allows one to directly upload the cord coordinates.

- – *Output Geometry* defines the output format of the coordinate point on the Cartesian plan of the blade profile in each section. The number of blade section can be regulate in *Set-Up*. It is set to Solid Edge by default.
- – *Simulation* defines the goal, which means the optimum design.

Obviously, the algorithm individuates the optimum values of a, a' and c for each blade section using the BEM theory, applying some corrections, if activated, as above described. The logic scheme of GUI BEM algorithm is illustrated underneath: The algorithm uses an iterative approach running-up to the latest values of a, a' and c as long as the previous ones diverge less than ϵ, previously determinate. Using the first attempts values, the entry U_{rel} value is calculated and by one branch, ϕ angle is resolved using velocity triangle, by the other branch the values of C_l and C_d are obtained. Given a rate to solidity, the BET equations of thrust and torque are solved with new values of a, a' and c'. The algorithm works as time as the system doesn't converge.

In this thesis, the law used by GUI BEM to define the optimum chord lengths distribution is the Maalawi's method, that corresponds to No. 11 of Tab.3.1.

The sections of the blades, where the profile are computed, have the following marked radius:

0.039	0.04	0.043	0.048	0.055	0.063	0.073	0.085	0.099	0.113
0.039	0.04	0.043	0.048	0.055	0.063	0.073	0.085	0.099	0.113
0.326	0.340	0.540	0.366	0.376	0.384	0.391	0.396	0.399	0.400

When BEM running process is over, an excel file that includes all the Carte-
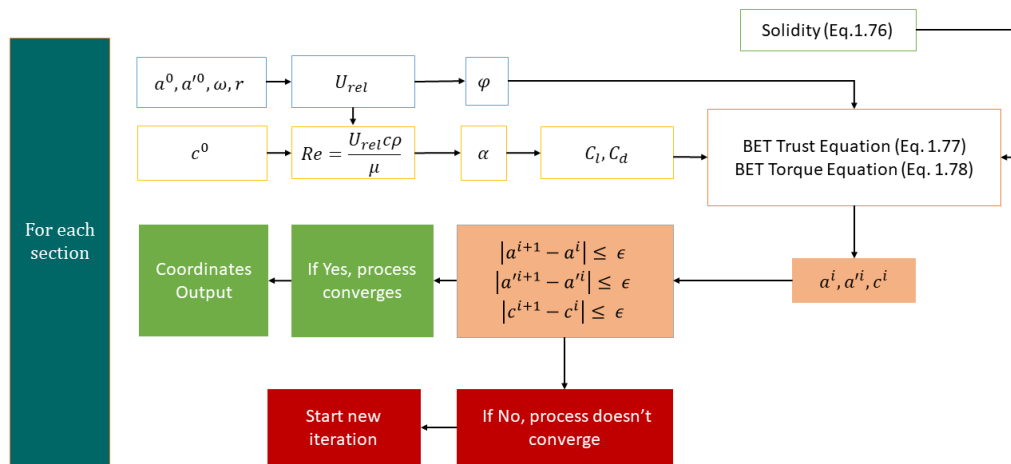
Figure 4.9: Scheme of GUI BEM algorithm

sian's coordinates of blade profile in correspondence of the marked radius is saved. The coordinates are merged, via a 3D CAD software, usually Solid Edge, to draw the correspondence blade surfaces. Also the leading and trailing edges is drawn to close the surfaces and lastly to create a solid body. The result is assembled with the hub and the diffuser to have a unique block body. So, the output is workable for ANSYS.

As the input wind speed is different between the two cases, the following chord distributions have distinct shapes: in particularly, from U_∞^8 is generated a slimmer line, particularly close the tip. Otherwise, U_∞^{10} produces a larger chord in the upper blade sections.

4.2   Simulation via ANSYS FLUENT

4.2.1   ANSYS Introduction

ANSYS FLUENT is a software suite for Computational Fluid Dynamic (CFD) applied in the field of thermal-fluid dynamics, created mainly for engineering scopes. The purpose of CFD is to solve wide-ranging fluid flow problems without building real models, which are a more expensive solution. The suite resolves the Navier-Stokes equations, even in three dimensions. Unfortunately, nowadays, an analytic solution has not yet been discovered, and thus the solver proceeds with a numerical approximation. Although Ordinary Differential Equations (ODE) and also Partial Differential Equations (PDE) have unique solutions, locally and globally, given initial values according to several theorems (see, i.e. Peano and
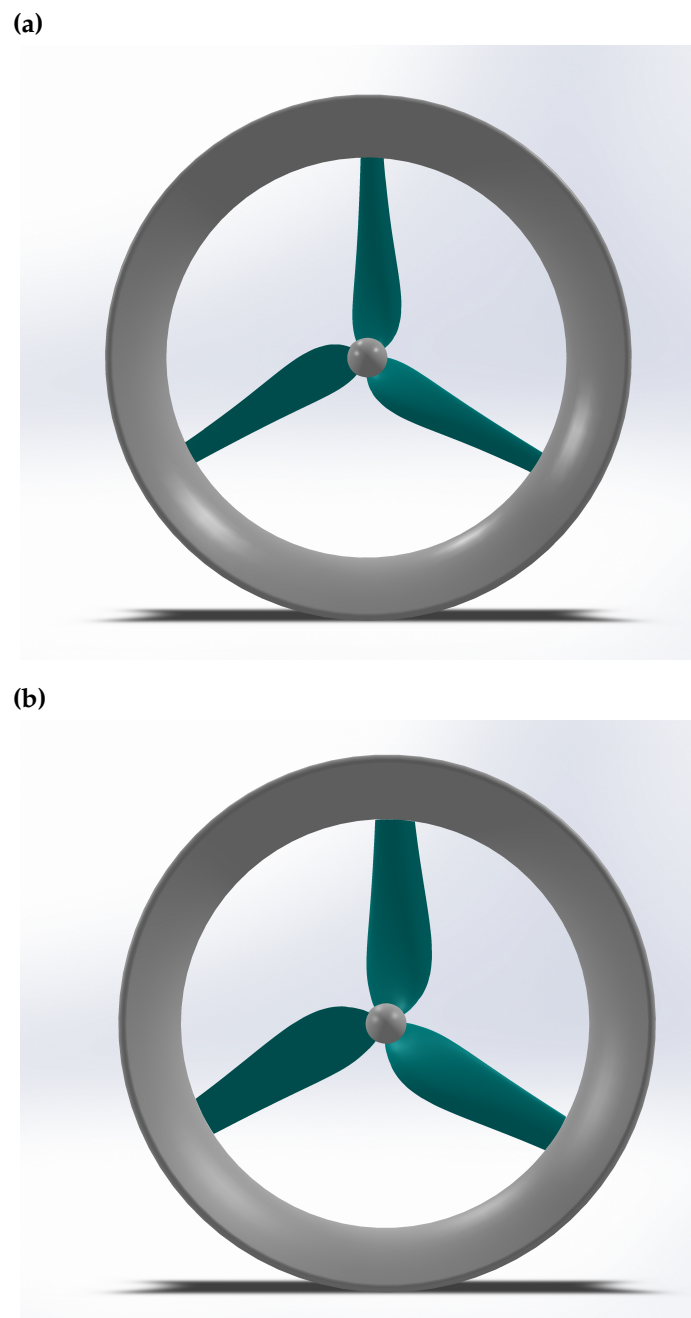
(a)

(b)

Figure 4.10: DAWT rendering without support at: (a) U_∞^8m/s and (b) $U_\infty^1$0m/s. In the latter, it is evident the thicker profile, especially on tips.

Picard-Lindelöf), only in few cases the software can elaborate on them to reach an exact and closed solution.

More often, the software uses a numerical approach, like the finite element method (FEM), transferring PDE in the form of algebraic equations linearising a discrete portion of geometry (see Fig.4.12). Whatever methods are used, the problem is moved from a continuous domain to a discrete domain, and the solution is proposed via discretisation (temporal and spatial). The small volume portion is
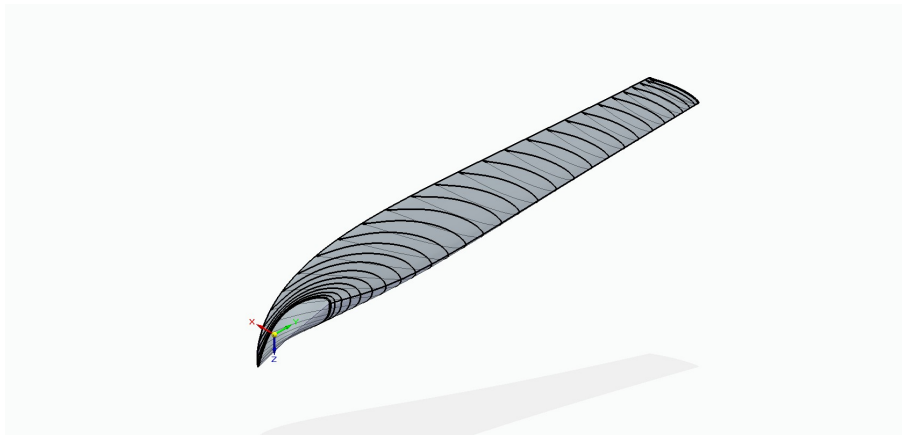
Figure 4.11: Solid Edge capture of $U_\infty^8 m/s$ design with Maalawi's chord length distribution without considering the presence of diffuser

called mesh, surrounded by mesh nodes. The linear system equation is resolved in the nodes at the center of the mesh, with the assumption that the solution is also the same for the entire volume of the mesh. Using an Input/Output approach, the solution obtained corresponds to the boundary conditions for the adjacent nodes. It is immediately evident that the solution is strongly correlated with the quality of the mesh, which can be evaluated by the following characteristics:

- Mesh type
- Mesh quality
- Number of nodes

Consequently, discretisation choices play a crucial role in numerical computation. Two topological elements are possible: the tetrahedron and the hexahedron. However, it is crucial to identify in which domain there is a computational advantage for building structured meshes[7]. Alternatively, it is preferable to keep the unstructured mesh[8]. The unstructured grid has irregular connectivity with a mixture of elements. It is autonomously generated via software and essentially depends on the number of nodes that are needed to individuate an acceptable solution. Meshing in a structured way is highly space-efficient because of regular connectivity amongst the grid. The best approach is to develop a hybrid grid that contains a mixture of structured and unstructured parts following the principle of increasing the quality of the mesh only in the domains where it is crucial to obtain the maximum possible accuracy. It is an approach direct to curb the time spent for resolving the system. For example, increasing the resolution close to the boundary layer or in the proximity of relevant components (i.e., blades) enhances accuracy. Another advantage is the reduction of error propagation among close

---

[7]Generally, the structured meshes are composed by hexahedron elements
[8]Unstructured meshes are mixtures of tetrahedron and hexahedron elements

meshes. Unfortunately, the creation of a structured mesh requires a larger amount of time than building an unstructured mesh. Therefore, it is recommended to create an unstructured mesh in the area where the resolution can be low (i.e., the ambient volume far away from the blades). As the structured meshes need more time consuming and generate a lot of more stress to the operator, they are used only for the domain where it worthwhile as, for example, greater ambient volume, that is not directly involved in the perturbations close the rotor.
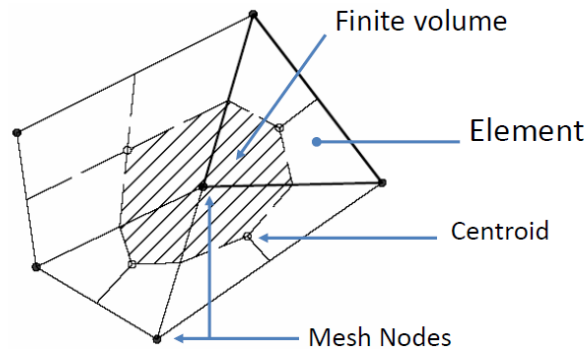
Figure 4.12: Single grid element

4.2.2 Turbulence

In 1932, one of the pioneers of turbulence research, the British physicist, Sir Horace Lamb, at the end of his life, has playfully expressed the challenges faced to find an analytic solution for a chaotic flow,that is ruled by turbulence:'... when I die and I go to Heaven, there are two matters on which I hope for enlightenment. One is Quantum Electrodynamics, and the other is the turbulent motion of fluid. And about the former I am really optimistic.'[9] Keeping this fun fact in mind, the following discussion is rather concise and focuses on ANSYS models of turbulence perturbation.

The fluid motion are broken down in two states: laminar or turbulent. Each state is essentially a property of the flow and not the fluid. Therefore, in theory, each fluid can flow turbulently, if the external conditions allow to develop this pattern.

In the laminar flow, the streamlines usually do not cross and each property (e.g., velocity profile) does not change from one instant to the another. Besides that, although the laminar flow can be affected by the external influences (e.g., forces acting on the fluid, with a positive derivative respect time), but the force variation is slow in comparison with the time has been required to establish the current state. On the other side, the turbulent flow needs to be dominated

---

[9](Goldstein1969)

by a chaotic disorder. Additional, a series of conditions need to be completely developed before the turbulence become the motion driven:

- **Movement** Turbulence is a property of the flow not the fluid and hence no property of the fluid material. The material fluid can only influence how much more or less easily a flow become turbulent. In any case, having motion is a prerequisite for turbulence.
- **Irregularity** Turbulence is an example of deterministic chaos: even if the flow follows the conservation equations, that are deterministic as all other natural laws, at the same time the dependence on the initial conditions is so strictly that become impossible to determine its exact future, beyond a generic level of forecasting.
- **Mixing** Turbulence flow has a mixing greater than laminar, exchanging better momentum, heat and mass between layers. The turbulent flow allows a strong mixing (10^6 times stronger than laminar flow) as the mixing is driven by turbulent diffusion and is proportional to dimension of domain.
- **Vorticity/Rotation** Turbulence involves all three spatial axes being rotational. Hence, a three-dimensional approach can be avoided.
- **Dissipation** A continuous energy input from external is need to keep the turbulent status as the turbulence quickly ends due to dissipation
- **Continuum** In a fully turbulent flows, turbulent eddies of all spatial scales can be individuated, even if, tedentially there is at least one preferred eddy sizes.
- **Configuration** The turbulence problems are always problems about boundary conditions as the flow state can not be isolated by its environment.
- **Non-linearity** The reverse flow mechanism are always coupled with a turbulent motion. Consequently, turbulent flows have a tremendous non-linear behaviour.

When a flow becomes turbulent all those characteristics become present. The Fig.4.13 shows how the turbulent features affect a flow regime inside a tube.

The first deep research about the transition from laminar to turbulent flows was made by Reynolds.[10] Reynolds hypothesis is that the transition is owned to the ratio between the external forces acting on the fluid and the internal forces.

The external forces tend to make the flow unstable as the disturbance can grow, while the internal forces tries to wipe out the instability thanks to strong inner bonding owned to fluid viscosity, ν. Naming U_* as the characteristic velocity scale and L_* as the characteristic length scale for the turbulence under consideration:

---

[10]Osborne Reynolds (1842 - 1912) is an English physicist known for his fluid-dynamics studies.
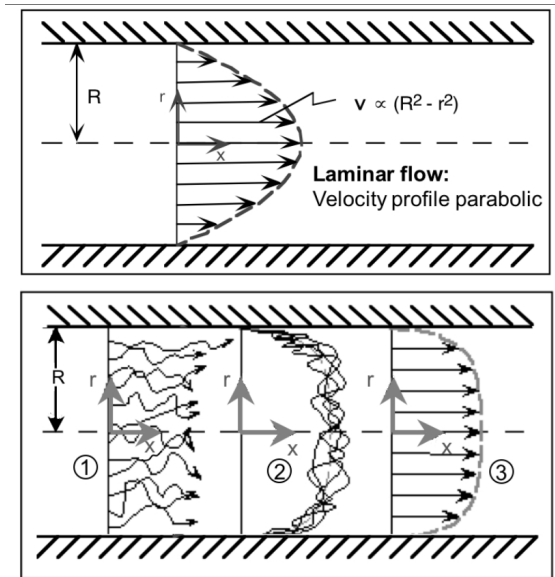
Figure 4.13: Laminar and turbulent flows in a pipe are presented respectively in the upper and lower panels. In laminar situation, the velocity profile has a parabolic shape in every instant. Inversely, the trajectories change every instant in the turbulent flow (1); therefore, the instantaneous velocity profile changes in accordance with (2). The average velocity profile (3) results to be more squeezed respect the parabolic in laminar flow.

- External forces (inertial forces):

$$| \vec{F_e} | \sim u \frac{\partial u}{\partial x} \propto \frac{U_*^2}{L_*} \qquad (4.1)$$

- Internal forces (molecular friction):

$$| \vec{F_{mf}} | \sim \nu \frac{\partial^2 u}{\partial x^2} \propto \nu \frac{U_*}{L_*^2} \qquad (4.2)$$

Hence, the ratio of two forces is:

$$Re =: \frac{U_* L_*}{\nu} \left(= \frac{U_*^2/L_*}{\nu U_*/L_*^2} \right) \qquad (4.3)$$

If $| \vec{F_e} |$ results dominant, the flow becomes turbulent. Contrarily, if $| \vec{F_{mf}} |$ keeps dominant, the flow remains laminar. The turbulence is a property of the flow (U_*, L_*), but the transition to turbulence depends by fluid property (ν).

Reynolds' research concluded that a flow is turbulent if $Re > 2000$. This value is the outcome of Reynolds' experiment (see Fig.4.14) and needs to be take into consideration using a wide approximation. Indeed, its accuracy is valid more narrowly inside a tube, but no generally. For example, external flow along a surface become a turbulent for $Re > 500.000$[11].

---

[11]Assuming water at 20°C flowing on a flat plate with the its kinematic viscosity equal to

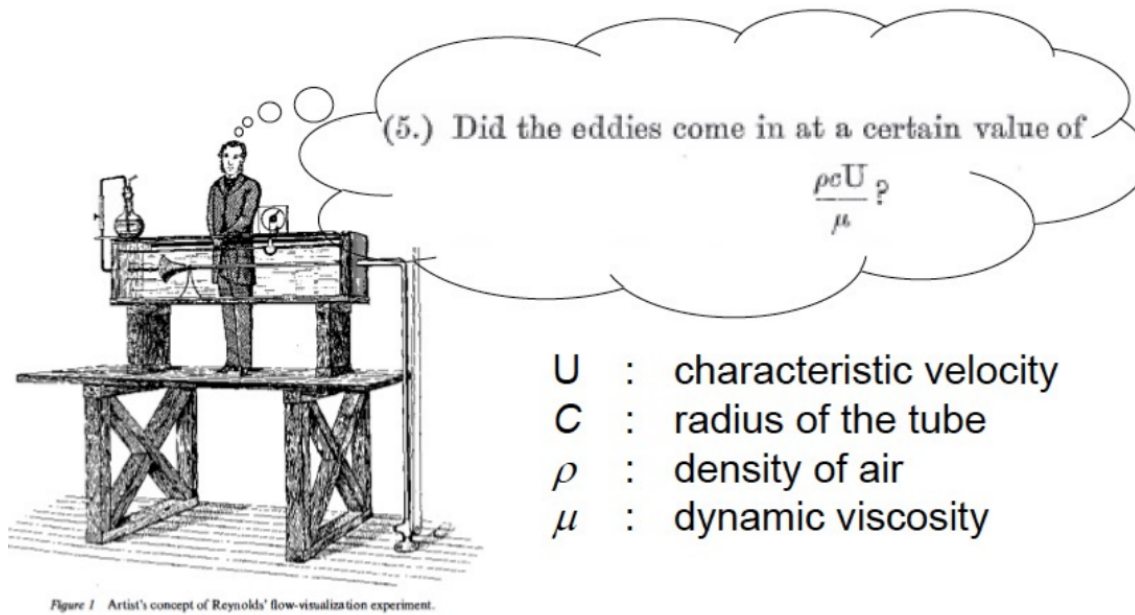Figure 1 Artist's concept of Reynolds' flow-visualization experiment.

Figure 4.14: In 1883, Reynolds conducted eddies experiment through a pipe looking for the starting transition point from laminar to turbulent flow.

The viscosity is the only fluid property, that plays role to determinate the type of motion is ongoing. The other indicators, velocity U_* and domain L_*, are completely decoupled to the fluid and depend only of boundary conditions. In case of wind turbines, Reynolds number is usually rewritten in the form $U_{rel}c\rho/\mu$, where the air viscosity can be considered constant in the operative range, U_{rel} is clearly the relative velocity, while the chord c express the length domain. Given a fixed U_{rel}, the optimisation procedure of c determines also the value of Re and therefore the type of turbulence the blade have to face off. As the turbulence conditions impact to the value of C_d, increasing it, even abruptly, this affect the glide ratio C_l/C_d and lastly the lift can be generated at design condition.

Turbulence transition

The sign that a flow starts transition from laminar to turbulent is the eddies arising (see Fig.4.15). The eddies are a sheet of vorticity inside the streamlines that are not parallel anymore. The eddies evolve with velocity field induced by itself and by all other vertical structures. During their evolution, the eddies remain localized for a certain time because vorticity can spread only by material movement of diffusion.

$110^{(-6)}m^2/s$ and its velocity $1m/s$.
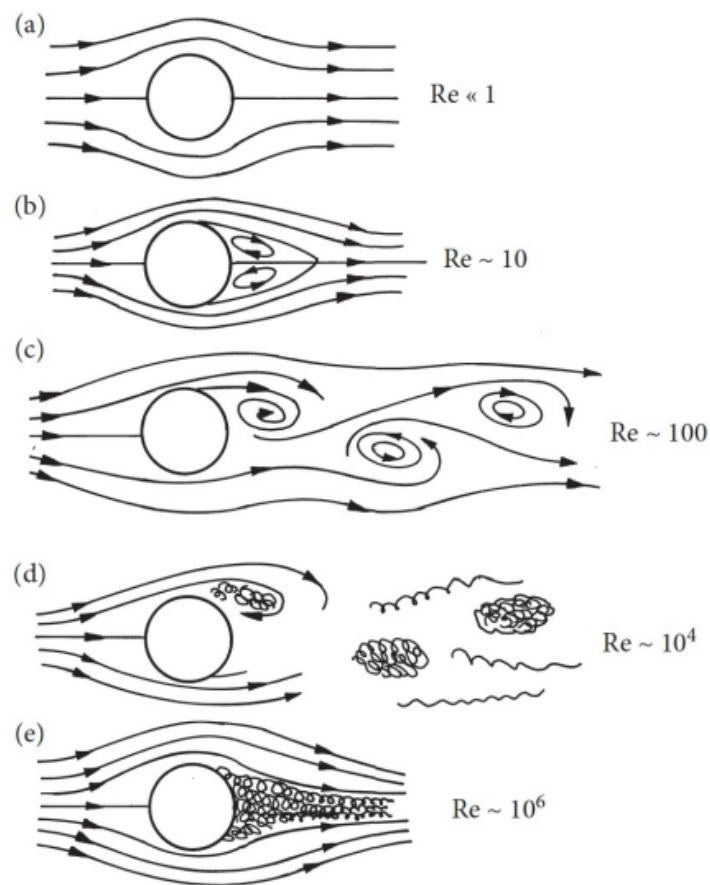
Figure 4.15: Transition of a flow wrapping a cylinder from laminar (a-c) to turbulent (d-e).

How to describe turbulence?

As turbulence has been described so far like a chaotic and irregular motion, there are not any practical advantages to describe each trajectory inside a turbulent flow. In addition, the current processing power is far from being able to solve problem like that. Indeed, the Direct Numerical Simulation (DNS), i.e. the calculation of each trajectory and therefore of the entire spectrum, requires very quicly enormous requirments of computing resources making this method impractical. Although theoretically, all turbulent flows can be resolved by numerical solution by full system of Navier-Stokes equations, pratically this is computational prohibitive and it has never been implemented in ANSYS even for the easiest flows, that have industrial interest. For this reason, the most widely used approach for calculating industrial flows follows probabilistic techniques looking for the average values of parameters and their statistical variance. In fact, "the random movement of air parcels, deviating from mean flow, is called turbulence. The mathematical notation of turbulence is typically done in terms of deviations from
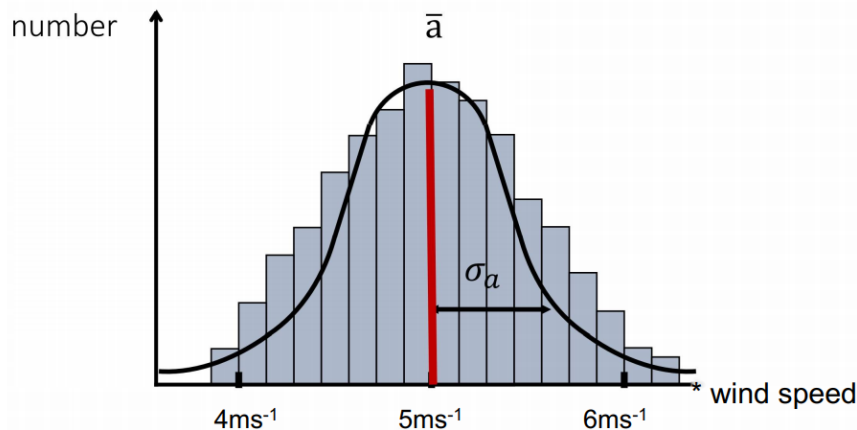
Figure 4.16: Histogram of a probability density function in case of turbulent wind speed

the mean state of a given variable."[12]

The statistical approach has previously brought a whole family of models, called Reynolds-Averaged Navier-Stokes (RANS), that are able to resolve for all length scales time-averaged Navier-Stokes equation.

The pivotal idea beyond the RANS models is rewriting the equations in accordance with *Reynolds decomposition and averaging*. A generic property of the flow (e.g. wind speed as expressed in Fig.4.16) becomes the sum of two contribution:

- mean value of *Probability Density Function* calculated by all the data, frozen frozen passing the sensor (Taylor's hypothesis): $\hat{a}$
- variance respect the mean value: $\sigma_a^2 = (a - \hat{a})^2$

The same interpretation can be used for all the variables involved in a turbulent flow, e.g. temperature, heat flux, etc.

The variance respect the mean value, calculated within a time step, can be called fluctuation and represents the flow turbulence. It could seem that the average value depends by the choice of time step, but if the choice has made appropriately (e.g. Reynolds proposed a pragmatic choice about timing) each variable become the sum of mean value and fluctuation:

$$a(t) = \overline{a} + a'(t) \tag{4.4}$$

The fig.4.17 shows the contribution of two terms, starting from the collection of signal data of a turbulent phenomenal.

More precisely, the average term is obtained calculating the mean value not only as a function of time, but also is the ensemble average of spatial coordinates.

---

[12](Holtslag2016).
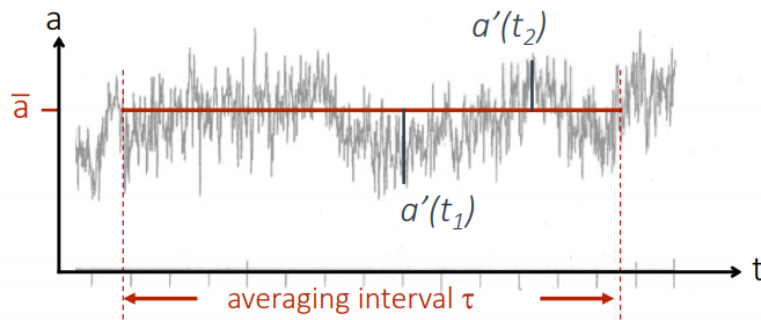
Figure 4.17: Reynolds decomposition of turbulent variable a within the generic time interval τ.

Indeed, the observations collect data of all the possible flow positions in space and time as the turbulence gives a chaotic trajectories spatially and temporarily[13].

$$\overline{a} = \frac{1}{N} \sum_{i=1}^{N} a_i(\vec{a}, t) \tag{4.5}$$

Hence,

$$a(x, t) = \overline{a}(x, t) + a'(x, t) \tag{4.6}$$

The Reynolds decomposition allows to separate the turbulence contribution from non-turbulent term.

Applying the Reynolds decomposition to the Navier-Stokes equations, the first order of Reynolds-averaged momentum equation is:

$$\frac{\partial \overline{u_i}}{\partial t} + \overline{u_j} \frac{\partial \overline{u_i}}{\partial x_j} + \frac{\partial}{\partial x_j}(\overline{u_i' u_j'}) = -\frac{1}{\rho} \frac{\partial \overline{p}}{x_i} + \nu \frac{\partial^2 \overline{u_i}}{\partial x_j^2} \tag{4.7}$$

written neglecting the gravity term and following the assumption of Boussinesq approximation [14], incompressible flow and Newtonian fluid. Clearly, i, j indicate unit vectors in x and y directions respectively.

Deriving the first order of conservation equation yields to unknown second order variables, owing to the presence of a covariance term regarding the divergence of the turbulent fluxes: $\frac{\partial}{\partial x_j}(\overline{u_i' u_j'})$. In fact, it can be shown that the higher the order of moment equations for which conservation equation are derived, the larger the number of unknowns variables becomes. Everyone, that tries to resolve the equations, has to deal with the dilemma, called *closure problem*. The dilemma consists that, regardless the order of moments for which conservation equations are taken into account, the number of unknowns is always larger than what can

---

[13]To simply, the following annotations show only one or two coordinates and time.

[14]The Boussinesq approximation means that the density fluctuations are negligible, i.e. $\rho'/\overline{\rho} \ll 1$

be resolved by the system. Therefore, the set of equations is never closed. Usually a *closure assumption* is imposed: the conservetion equation system is resolved up to order n. All the moments of order $n + 1$, that have more than $n + 1$ unknowns, are processed with parameterised terms.

The closure problem is resolved by ANSYS for the RANS models thanks to Eddy Viscosity Models, where the covariance term - $\rho\overline{u_i' u_j'}$ - is approximated by the equation:

$$\rho\overline{u_i' u_j'} \cong \mu_T f(\overline{u_i}, \overline{u_j}, \overline{u_k}) \tag{4.8}$$

The turbulent viscosity - μ_T - is yielded by time (or velocity) scale and length scale chosen and by the next parameters:

- Turbulent kinetic energy: $k = \overline{u_i' u_j'}/2 \quad [L^2/T^2]$

- Turbulence Dissipation Rate: $\epsilon = \nu\overline{\frac{\partial u_i'}{\partial x_j}}(\overline{\frac{\partial u_i'}{\partial x_j}} + \overline{\frac{\partial u_j'}{\partial x_i}}) \quad [L^2/T^3]$

- Specific dissipation rate: $\omega = \epsilon/k \quad [1/T]$

The turbulent viscosity is calculated differently by the models implemented in ANSYS and they are listed below in order of increasing computational requirement:

- **Spalart-Allmaras $[\mu_T = f(v)]$**
  The lowest-cost RANS model able to solve aerodynamic/turbomachinary applications with mild separation - such as flow over airfoils with high Ma number, boundary-layers, etc. Even if it has gained popularity for turbomachinary applications, it keeps to show doubts about applicability for all type of complex engineering flows.

- **$k - \epsilon$ Turbulence Models $[\mu_T = f(\frac{\rho k^2}{\epsilon})]$:**

  - *Standard $k - \epsilon$ (SKE) model* is the most widely-used engineering turbulence model for industrial application thanks the acknowledge of its accuracy and confidence. The greater limitations are that ϵ equation cannot be calculated at the wall without the help of dedicated function and generally has weak performance over flows with strong separation or large streamline curvature.

  - *Renomalization group (RNG) $k - \epsilon$ model* uses re-normalization techniques and performs better than the latter for more complex shear flows.

  - *Realizable $k - \epsilon$ (RKE) model*, where the realizable means that the model satisfies mathematical constrains on the covariance term. Neither the

standard $k-\epsilon$ model nor the RNG $k-\epsilon$ model is realizable. This feature provides better performance for flows involving rotation.

- **$k-\omega$ Turbulence Models** [$\mu_T = f(\frac{\rho k}{\omega})$] is an ensemble of models that have acquired notoriety because work well for a wide range of boundary layer flow with pressure gradient. Two variants of $k-\omega$ models are presented in ANSYS:

  - *Standard $k-\omega$ (SKW) model* is the most widely adopted in the aerospace and turbomachinery problems.
  - *Shear Stress Transport $k-\omega$ (SSTKW) model* uses a blending function to gradually transition from the standard $k-\omega$ model near the wall to high Re number version of the $k-\epsilon$ model in the outer portion of the boundary layer. In comparison with $k-\epsilon$ and its difficulties close to wall boundary, $k-\omega$ suits as better as possible close the wall and in free flow.

As the present discussion has shown that the Shear Strees Transport is one of the widely used model in turbomachinery projects with a rigorous background, it was preferred for all the simulations that have been computed.

4.2.3 Bundle Workbench

Workbench is the ANSYS interface tailored for collecting the entire simulation procedure: from the geometry up to CFX result analysis.

As Fig.4.18suggests, Workbench is organised in blocks; wherein each block represents a program for a specific step needed to operate, and the purple lines, that interconnect blocks, are an indication for ANSYS to transfer the output of one box in the input of next box. It is also possible to create new links to produce new simulations starting from the same block, with different operating conditions.

The following steps are necessary to prepare a simulation:

- **Geometry** works on the structure desired to simulate. The geometry can also be imported from other programs, like Solid Edge or SoldiWorks or created with the ANSYS built-in software DesignModeler.
- **Mesh** ICEM CFX program, which holds the scope to meshing the domains and generate the nodes where the equations will be solved during the next steps.
- **Setup** is needed mainly to define the boundary conditions, i.e. the characteristic of interfaces between domains, before running the solver. CFX Setup receives the geometry mesh and prepares the configuration for the solution.
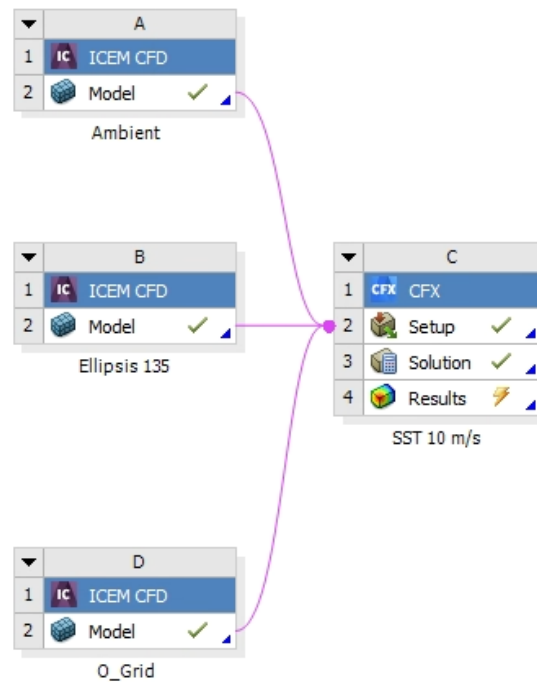
Figure 4.18: Screen of ANSYS workbench, in which all simulation steps are accessible and workable

Also, it defines which kind of parameters and physical quantities (i.e. force, pressure, etc.) has to be the simulation outcomes.

- **Solver**, managed by CFX Solver, defines the options regards the solution process, i.e. type of solver, the precision required, initial conditions, etc.
- **Post CFX** analyses simulation results and produce reports.

Although in Solid Edge assembly the file combines together all the volumes (*Ambient* around the DAWT, *Hub*, *Blades* and *Diffuser*) to produces one single file, the work in ICEM requires a different meshing procedure based on the specific characteristic of each volume, that have different mesh requirements,i.e. structured or unstructured meshing. For this reason, bundle Workbench manages different volumes separately: *Ambient*, *Ellipsis 135*,*O_Grid*; the mesh of which are then merged thanks to bundle PRE CFX.

In the box **A**, the geometry of volume *Ambient* is modelled and meshed. The box **B** of volume *Ellipsis 135* contains the blade and diffuser geometry coupled with the hub geometry. In the box **D**,referred to volume *O_Grid*, there is the geometry of the wrapping around the blades, required to increase considerably the mesh quality in the region where it is crucial having as more information as possible about fluid motion.

The three purple lines from the ICEM boxes to box **C** lead ANSYS to merge

the separated workflows in one single file ready for the setup.

4.2.4 Bundle ICEM

The bundle ANSYS ICEM CFX provides all the common tools to refine and mesh the geometry for exporting to CFX Setup. Meshing requires the following steps.

- Geometry definition: import the geometry from CAD software
- Domain definition

  - The whole geometry has to be sliced into different domains, associated with different boundary conditions. Each part corresponds to a surface or a volume, that has a different relationship with the boundary.
  - Every domain has to be named differently. It is important to pay attention to naming because the software autonomously links the domain designation to a specific boundary condition: e.g., the inlet (outlet) or inflow (outflow) is considered the cross-section where the fluid goes into (exits out) the control volume.

- Topology definition is correlated to which typology of structured mesh wants to be created. Indeed, the first step to creating a structured mesh is that the domain is enclosed roughly in a parallelepiped (single block). The parallelepiped is modified, cutting in multi-block and merging them, which are the domain logical representation. The computer resolves the equation block by block, therefore the blocks need to be distributed in such a way that have physical meaning, i.e. the block has to follow the same flow path.
- Mesh sizing: the number of nodes has an impact on the final result increasing the precision. At the same time, it weighs on the overall time to reach the solution. Therefore, it is important to balance the time consuming and the precision wished to obtain the convergence within a reasonable time and aligned with the computational power available.
- 3D mesh: The 2D mesh, just created, is extruded along the third dimension to occupy the entire domain volume.

ICEM uploads the geometry provided by a CAD software in generic format, like parasolid (file extension x_t).

Volume Ambient

The meshing procedure begins associating the following parts:

- AIR

- AMBIENT
- GEOM
- INFLOW_AMBIENT
- INLET_ELLIPSIS135
- OUTFLOW_AMBIENT
- OUTLET_ELLIPSIS135
- PERIOD_AMBIENT_01
- PERIOD_AMBIENT_02
- SHROUD_IN_AMBIENT
- SHROUD_OUT_AMBIENT
- SHROUD_UP_AMBIENT
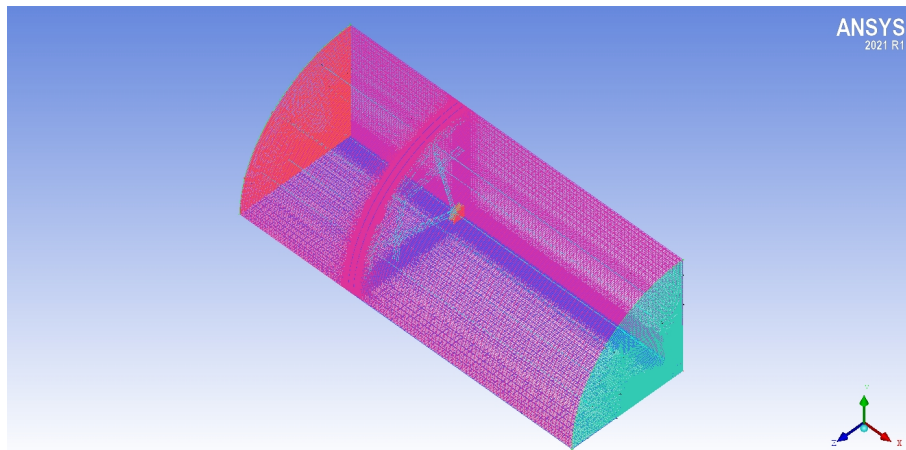
Figure 4.19: ICEM Ambient view

The quality of the ambient structured mesh is:
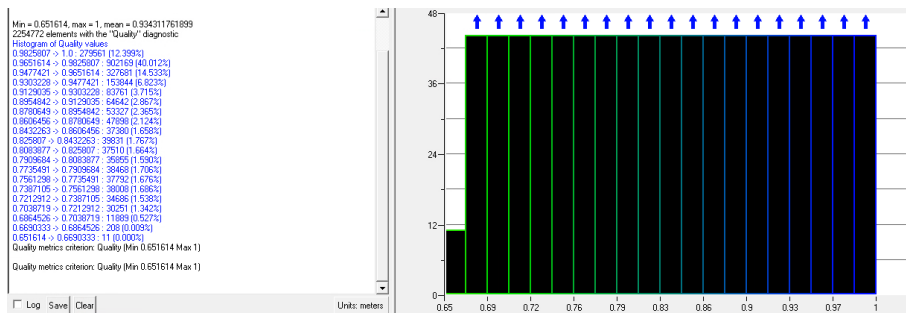
Figure 4.20: Mesh quality in Ambient

Volume Ellipsis 135

The chosen diffuser is as simpler as possible,e.g. it is designed without flange. This type of diffuser shape has been already used in previous works carried on by TES group.
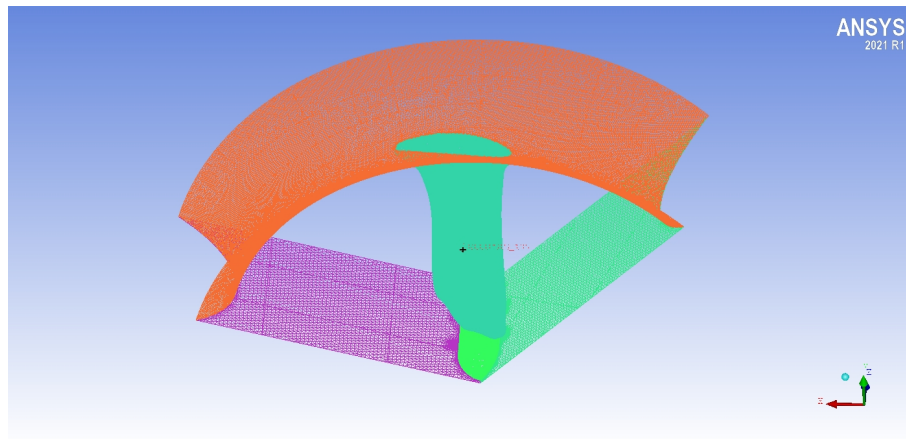
Figure 4.21: ICEM Ellipsis 135 view

Table 4.3: Diffuser Lengths

Diffuser Lengths	
D_{inlet}	0.92 m
D_{outlet}	1 m
D_{rotor}	0.8 m
L	0.24 m
L/D_{rotor}	0.3

hub, diffuser and the ORING grid. Therefore, the following parts are associated:

- ELLIPSIS_135
- HUB_135: the wall with the hub framework
- INLET_135: the surface of inlet flow
- OUTLET_135: the surface of outlet flow
- O_RING_135: the wall respect the O_RING grid
- PERIODIC_135_01
- PERIODIC_135_02
- SHROUD_135: the wall with the diffuser wall

The quality of the Ellipsis 135 structured mesh is:

Volume O-GRID

This volume has been create with the purpose to increase the number of nodes and also their geometric quality precisely in the region where more detail is required. Indeed, O-GRID packs the entire blade region, interfacing directly with blade, hub and diffuser. The O-GRID creates a higher quality unstructured
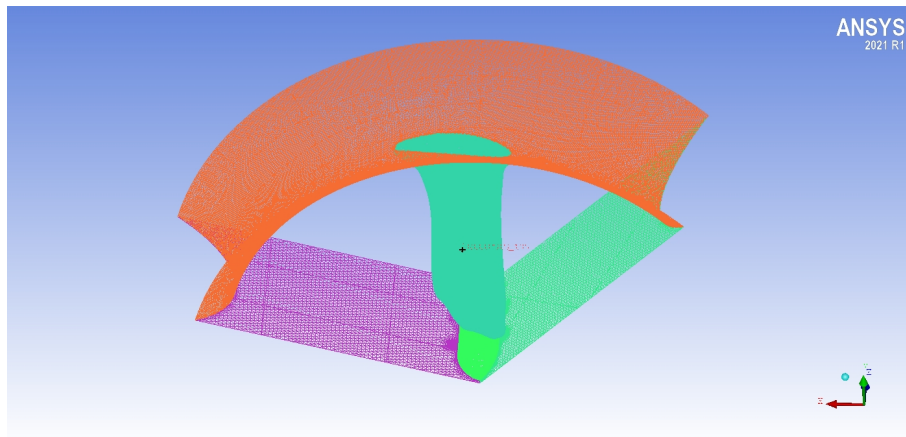
Figure 4.22: CEM Ellipsis 135 view
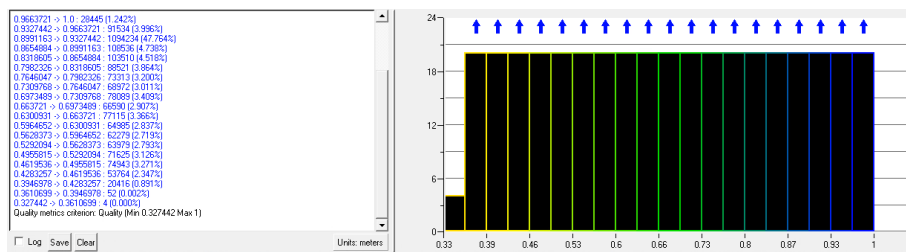
Figure 4.23: Screen of Ellipsis 135 quality mesh

mesh, that wraps the blade all around increasing the computational performance where more information needs. Also, the nodes, called O-RING due to their shape, gives output at highest quality.

The following parts are associated:

- BLADE
- GEOM
- HUB_O_GRID
- O_GRID
- O_GRID_DOMAIN
- SHROUD_O_GRID
- TIP_BLADE

The quality of the O-GRID structured mesh is:

The meshing procedure created mesh with this overall number of nodes and elements:
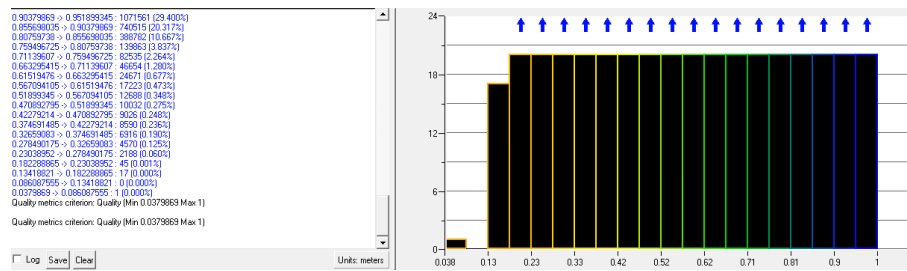
Figure 4.24: Screen of Ellipsis 135 quality mesh

Volume	*Elements*	*Nodes*	*Type*
Ambient	2.256.241	2.203.248	str.
Ellipsis 135	229.441	402.274	str.
O-GRID	3.650.250	3.548.637	str.
TOTAL	6.135.932	6.154.159	str.

4.2.5 Bundle CFX Solver

The CFX solver is essential to set the boundary conditions and indicate which parameters (i.e. forces) the operator wants as outcomes when the simulation ends. Moreover, it needs to associate the mesh parts with the physical flows and the real boundary conditions. In addition, periodic parts have to be associated with the rotating framework. The interfaces can be associated in a manner to allow the coupling of boundary conditions between adjacent parts. So far, work has been made only on a frame of 120°, which gathers one blade together with 1/3 of the hub and the diffuser. Now, it is possible to extend the frame at round angle to cover all three blades.

VOLUME AMBIENT

Domains:

- Air
- Ambient Interface (several sides)
- Inlet
- Inlet Ellipsis
- Outlet
- Outlet Ellipsis
- Shroud_in
- Shroud_out
- Shroud_up
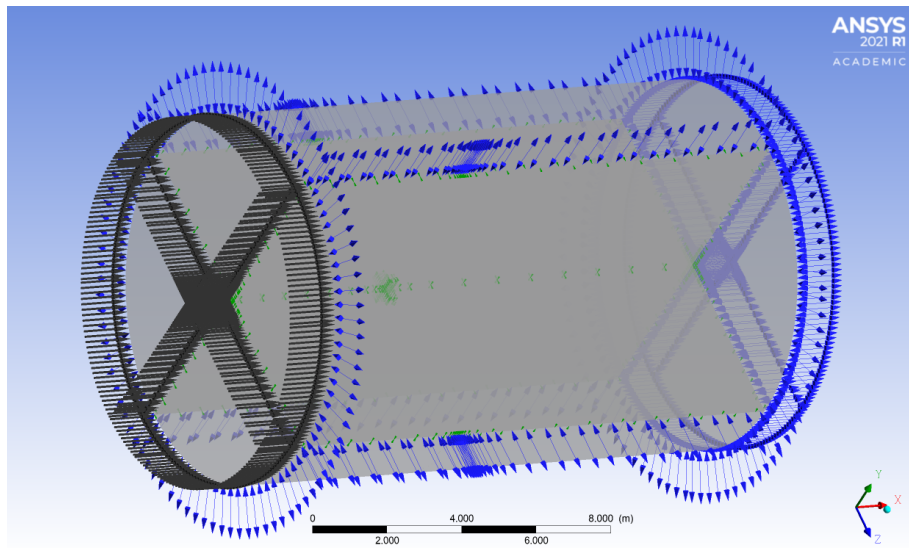
Figure 4.25: Screen of Ambient PRE-CFX

VOLUME ELLIPSIS

Domains:

- Hub_Ellipsis
- Inlet Ellipsis 2
- Interface O_Grid (several sides)
- Outlet Ellipsis
- Shroud_Ellipsis
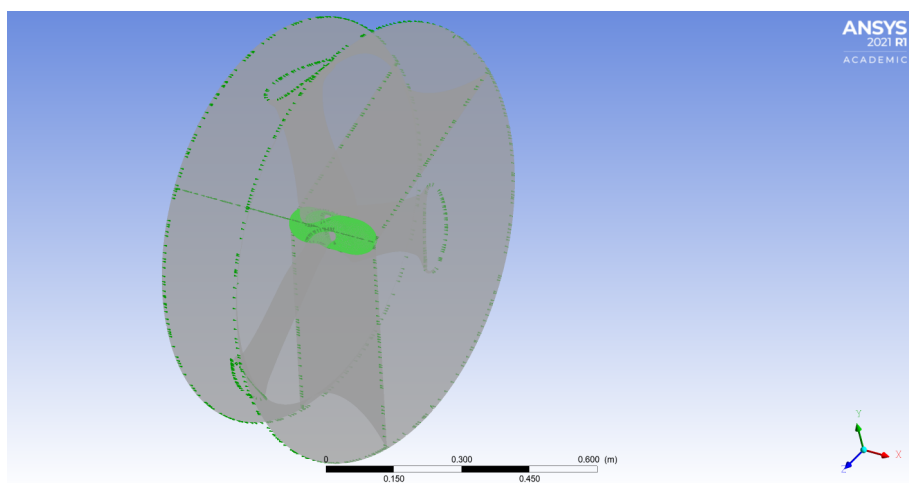
Figure 4.26: Screen of Ellipsis PRE-CFX

MAALAWI

Domains:

- Blade_01
- Blade_02
- Blade_03
- Hub_Malaawi
- Interface O_Grid (several sides)
- Shroud_Maalawi
- Tip_01
- Tip_02
- Tip_03
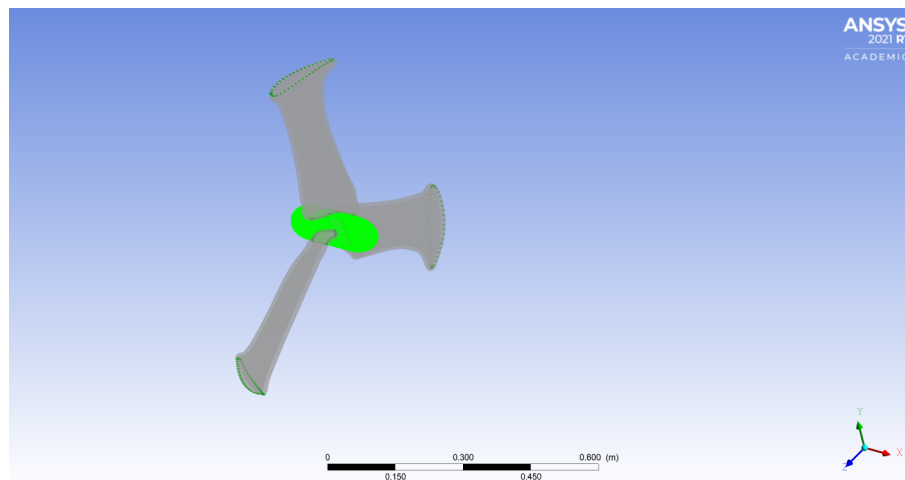
Figure 4.27: Screen of Maalawi PRE-CFX

In the initialisation details, U_∞ can be 8 m/s or 10 m/s according to BEM design velocity. In any case,the inlet velocity is not uniformly distributed, but the u and w components vary following a $\sin$ and $\cos$ functions, respectively. In contrast, the v component is set to 0 m/s. The static pressure is set at 1 Bar and a medium intensity is associated to turbulence, using SST method, as described Subsection:4.2.2.

4.3 CFX Outcomes Analysis

4.3.1 Tools for Analysis

A post processing analysis allows to extract the data from the simulation works and makes comparison. ANSYS provides a dedicated POST CFX soft-

ware for post processing. The software allows one to choose selected data and information, that can be exported via charts, for example.

The value of C_p along the polylines at the marked radius, decided in Tab. 4.1.2, can be chosen as a reasonable analysis tool. The polyline is a segment, that circles around the blade at constant marked radius. Fixed a polyline, a surface on the blade at certain radius can be created and, for example, velocity vectors can be drawn over the surface. Alternatively, i.e, a contour of pressure trend can be displayed.

The trend of C_p can be shown on a chart, using the length of polyline on x-axis and the corresponding C_p value on y-axis.

In the cited charts C_p is computed as a dimensionless ratio between the static pressure at the ambient, expressed in Bar, and the dynamic pressure at the rotational frame distinct for each radius, expressed in $Force/m^2$:

$$\frac{Pressure - 1}{\mathbf{ave}(Density)\mathbf{@Inlet} * (0.5\ \mathbf{massFlowAve}(Velocity\ u)\mathbf{@Inlet})^2 + (840\ \pi/30\ \mathbf{Radius})^2} \tag{4.9}$$

Thus, the trend C_p along the blade can be reproduced using the charts between polylines (x-axis) and C_p (y-axis) for all the marked radius. The trend, that is derivable by the charts, would be also confirmed by showing the contour surfaces along the blade (see Tabs. **??** -4.3.2), where the colour gradients show areas with positive or negative C_p values. Indeed, as theory results, the blade has two pressure sides: one located upstream have a positive pressure difference $\triangle p+$, the other, located downstream, shows a negative pressure difference $\triangle p-$. Ideally, an optimum outcome is that the pressure does not change the sign along each side of the blade.

Ideally, the C_p should not cross the zero line at any other point along the As the results show, c_p often changes the pressure sign moving along the polyline, especially close to the hub and tip regions. This unwanted behaviour is amplified when the charts are referred to simulation run for value of undisturbed velocity far from the correspondence design conditions (U_∞^8 and U_∞^{10}), i.e. close to cut-in or cut-off velocity, respectively 4 m/s and 16 m/s.

The same trend can be observed using the charts of polyline (x-axis) vs C_p (y-axis). Obviously, in one chart only the overview at fixed distance from the hub (z-axis) can be valuated, but the overall view for all the marked radius allow to see where the CFX suggests that the C_p diverges from expectations. Clearly, this is an indication about where there is room to improve the performance.

Another tools to make conclusions is to compare directly the C_p provided by BEM algorithm at the marked radius with the C_p, calculated via CFX, along the polyline at the same radius. Obviously, this comparison can be made only for CFX run set with the design velocities as BEM does not give off design output.

In Tab:4.3.2for U_∞^8 and in Tab:**??** for U_∞^{10}, it is presented a comparison along different selected marked radius for both type of designs.

In addition to a graphic overview, POST CFX owns the tools to calculate the force and the torque.[15] In this way, it has been possible to obtain easily the value of the torque on the rotation axis along a blade, yielding readily to the power outcome in set wind conditions:

$$P = n_b * Q * \Omega \tag{4.10}$$

In those simulations, the rotational speed is fixed at 840 rpm, equal to 87.95 rad/s and is kept constant due to the absence of any variable-speed control system. The charts of the power outcome respect the windspeed is called *Power Curve*. Knowing same reference power points, it is also possible calculated the C_p espressed as:

$$C_p = \frac{P}{1/2\rho U_\infty^3 \pi R^2} \tag{4.11}$$

and compering it respect λ on a chart.

4.3.2 Performance Curve Results
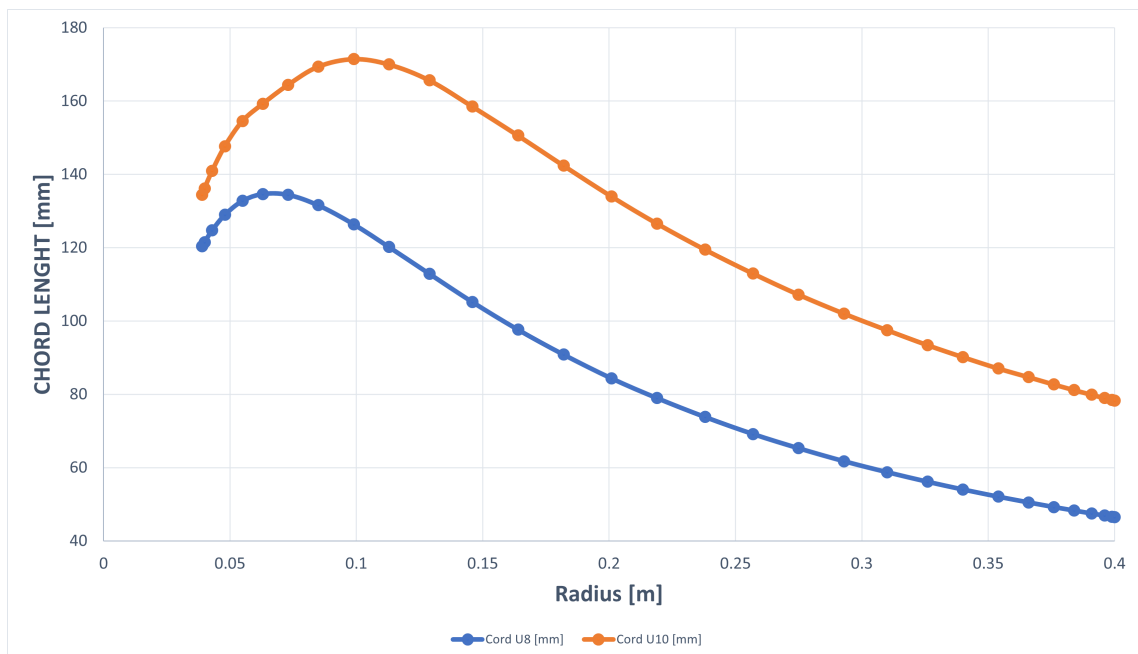
Figure 4.28: Comparison of chord length vs radius for integrated and Distinct Designs

The Fig.4.28shows that using an augmented wind speed for design velocity

---

[15]Obviously, other physical quantities, e.g. pressure and temperature, can be calculated via software) on a specific surface.
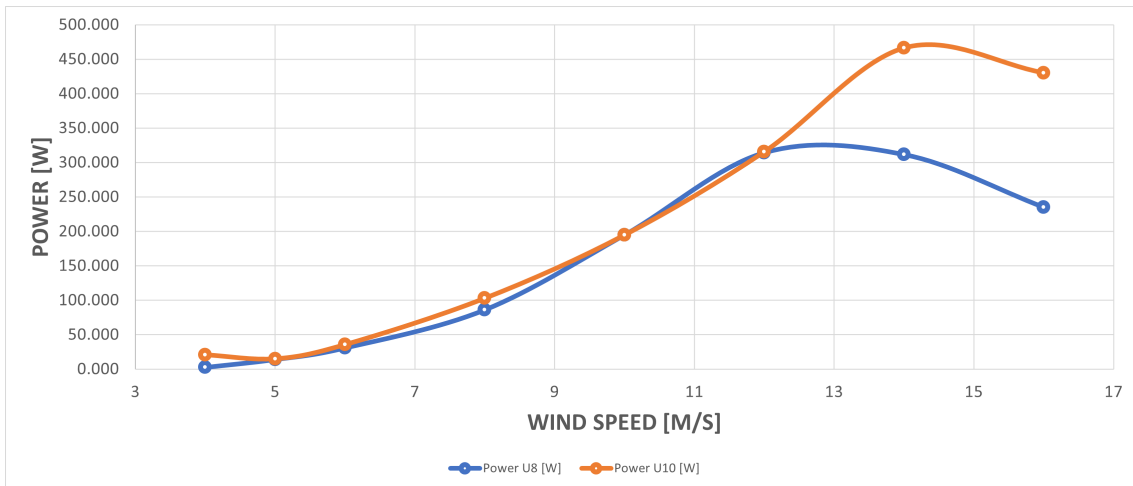
Figure 4.29: Power curve of simulated DAWTs

produces an increase in the chord lengths not only at the radius close to the hub, but also in the tip areas. Having fixes a speed-up in the design wind yields, via Maalawi's formulation of chord lengths, a thicker chord all along the blade. Indeed, an augmenting of design wind changes the angle of attach, suggesting a blade shape that diverges respect what is usually proposed.

At the same time the power curve is comparable with actually on the market open turbine, as Fig: **??**. However, the radius, excluding the diffuser, of DAWT is smaller.
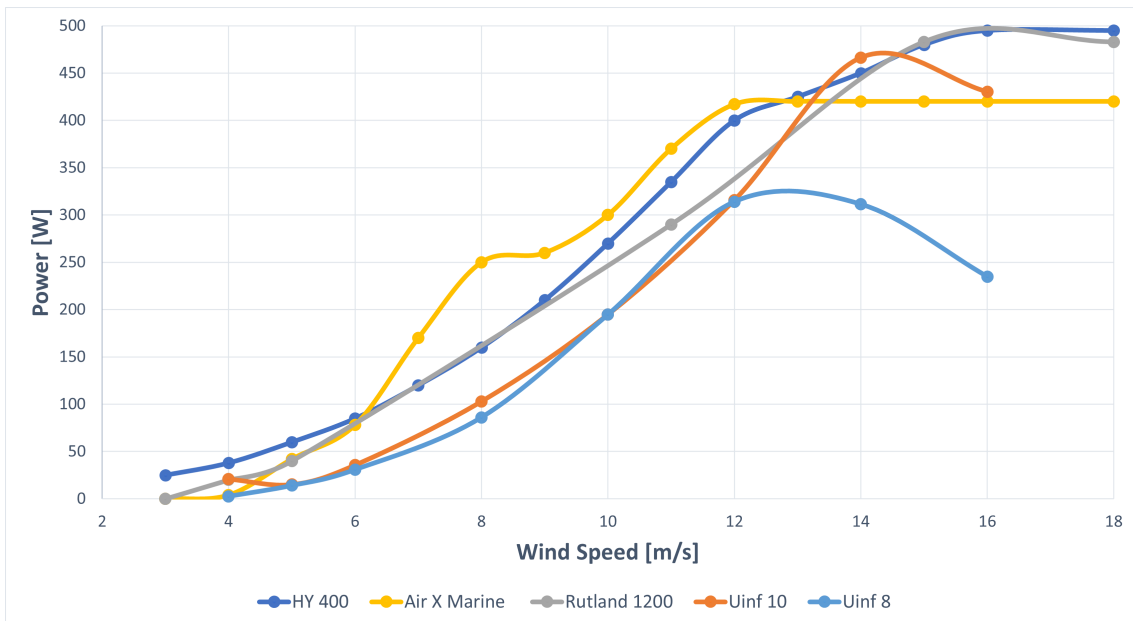
Figure 4.30: Chart of Power Curve for integrated and Distinct Designs compared to commercial turbines

The $C_p - \lambda$ curves in Fig.4.31 indicates that both solution are able to overcame

the Betz-limit, especially the integrate solution close to the design conditions: λ
between 4 and 5.
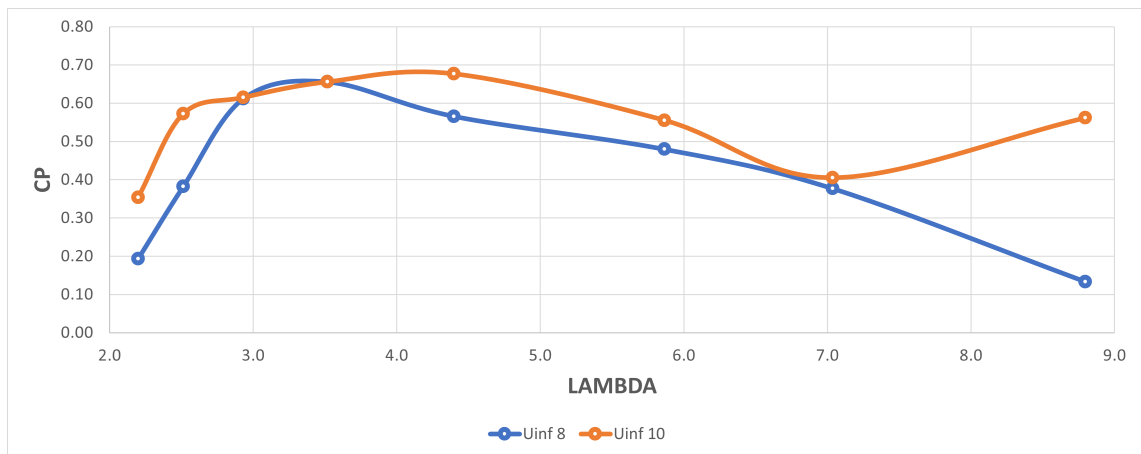
Figure 4.31: Chart of $C_p - \lambda$ Performance Curve for integrated and Distinct Designs
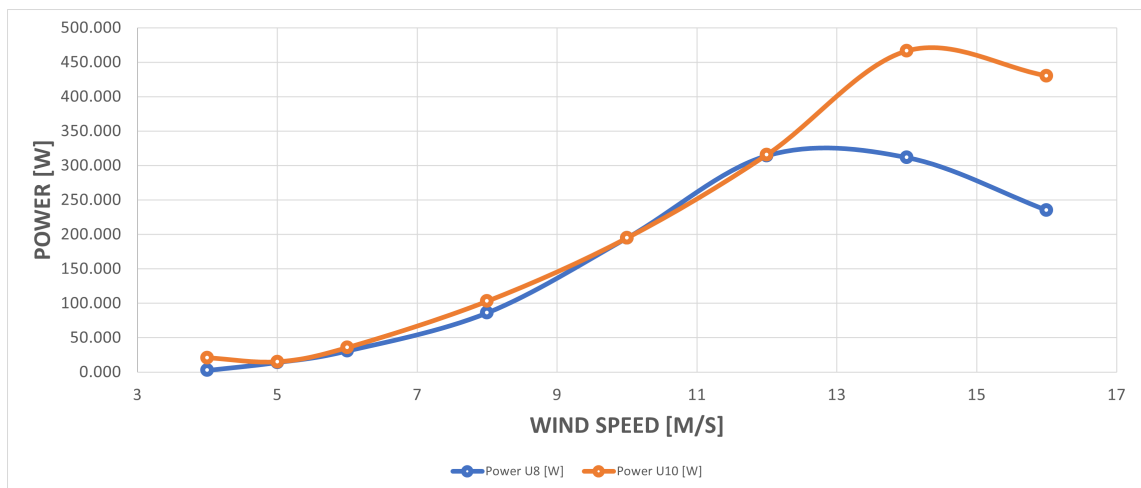
Figure 4.32: Chart of Power Curve for Integrate and Distinct Designs

Distinct Design
$$U_\infty^8$$

Table 4.4: CP CONTOUR U_∞^8 at 8m/s

PRESSURE SIDE
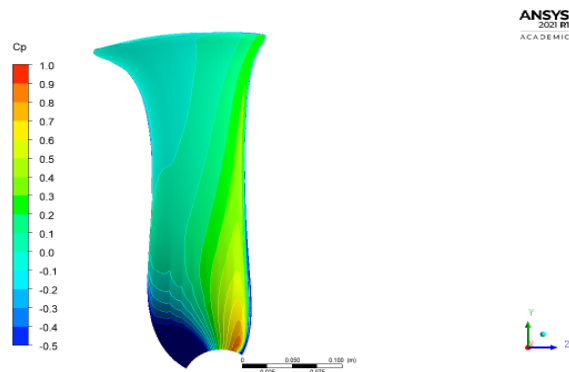
DEPRESSURE SIDE
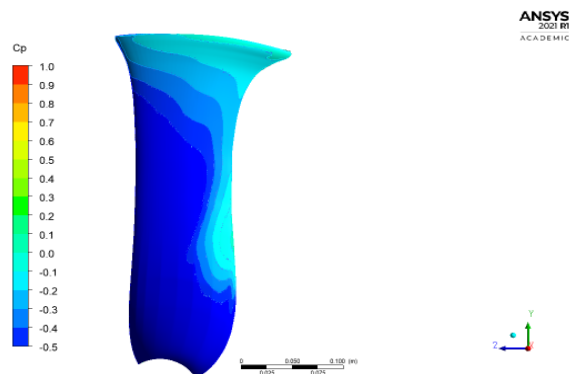
Table 4.5: C_p^{BEM} vs C_p^{CFX} at U_∞^8

C_p R 0.043 m
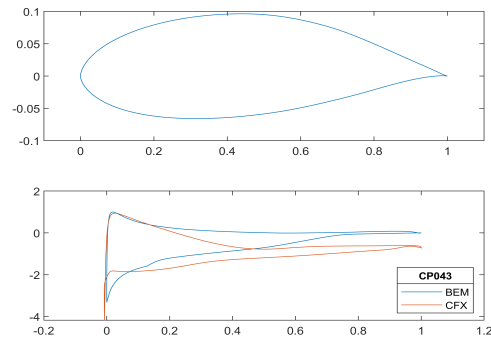
C_p R 0.129 m
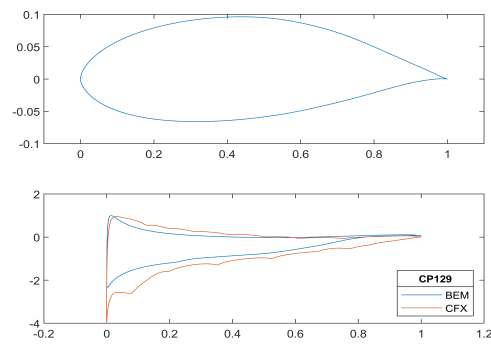
C_p R 0.293 m
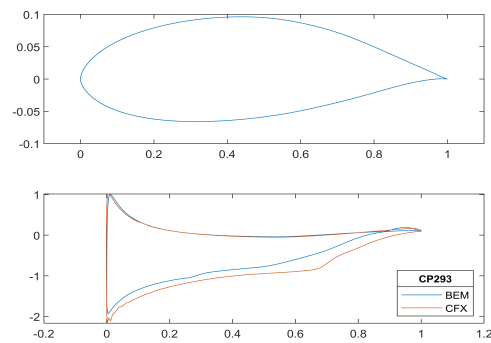
C_p R 0.391 m
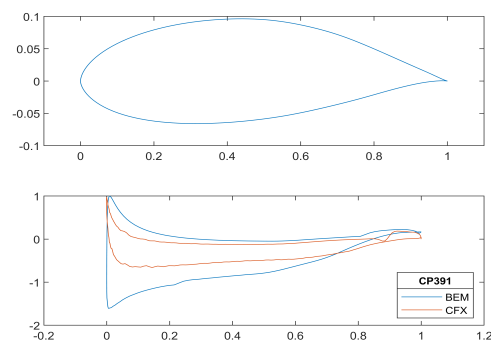
Table 4.6: C_p charts at R 0.201 m of U_∞^8 at several U_∞

U_∞ 5 m/s
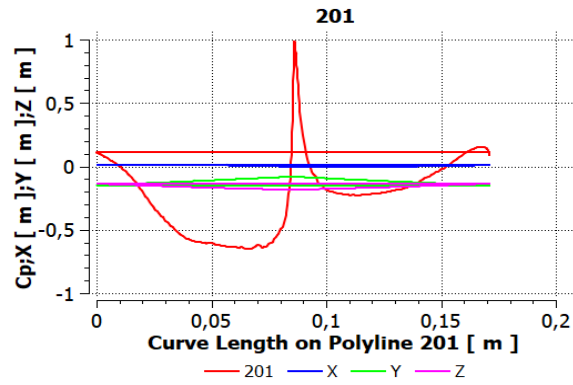
U_∞ 8 m/s
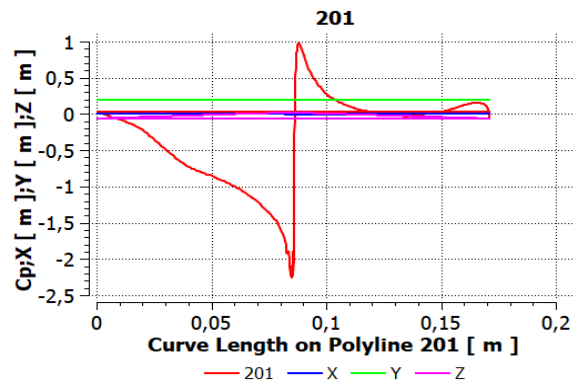
U_∞ 10 m/s
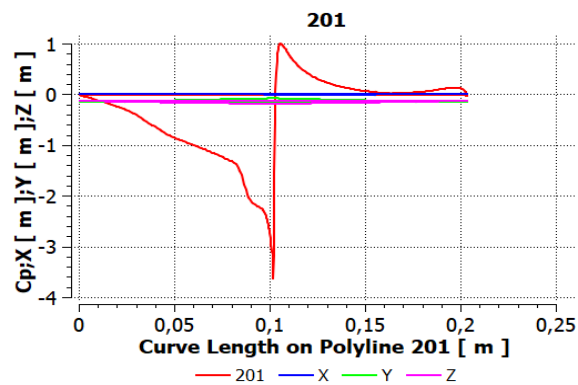
U_∞ 14 m/s
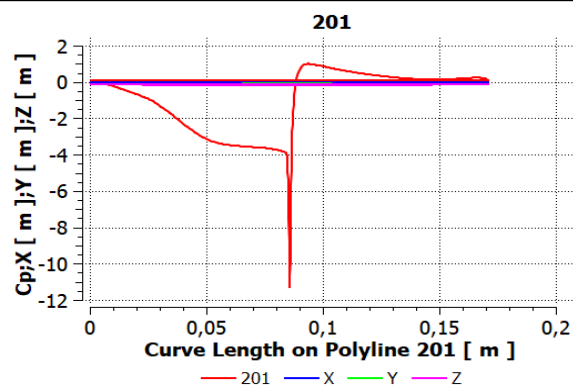
Table 4.7: C_p charts at R 0.384 m of U_∞^8 at several U_∞

U_∞ 5 m/s

U_∞ 8 m/s

U_∞ 10 m/s

U_∞ 14 m/s
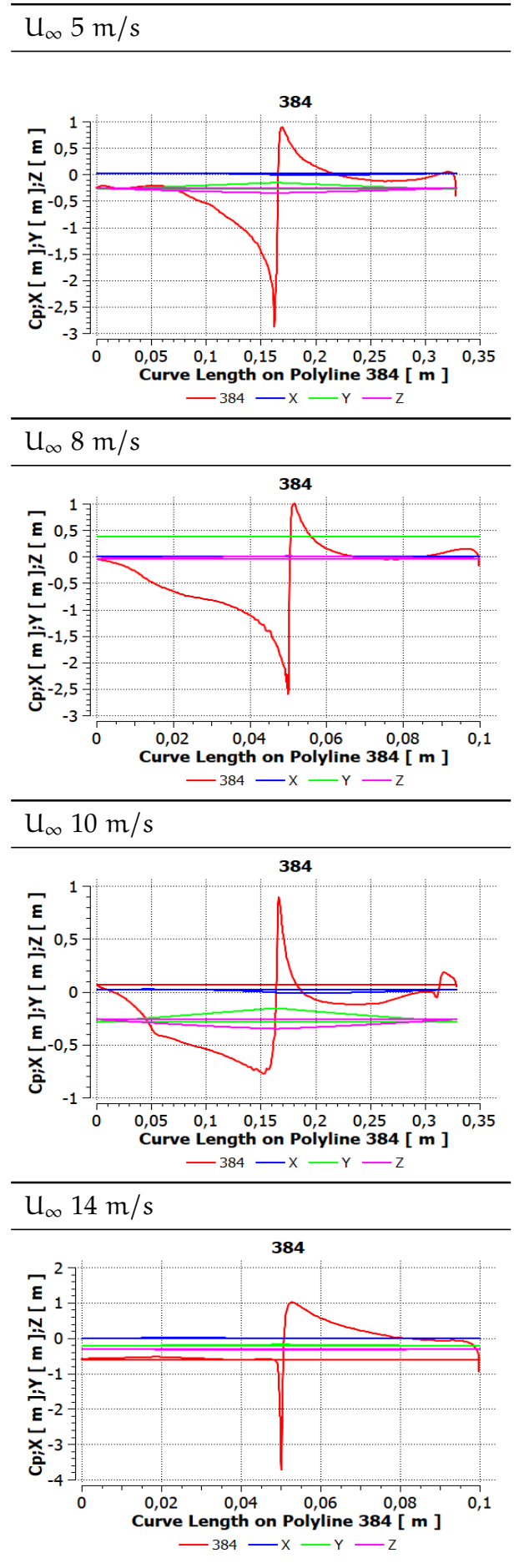
Integrate Design
$$U_\infty^{10}$$

Table 4.8: CP CONTOUR of U_∞^{10} at 10m/s

PRESSURE SIDE
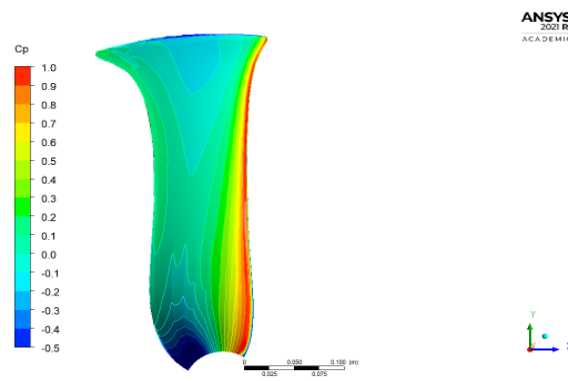
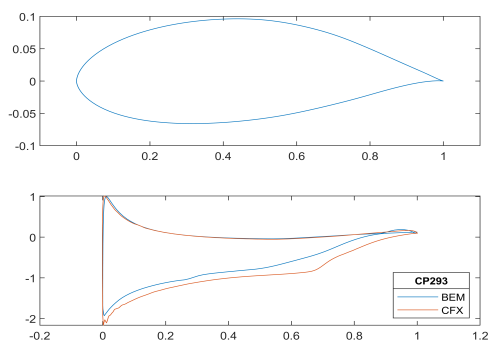## DEPRESSURE SIDE
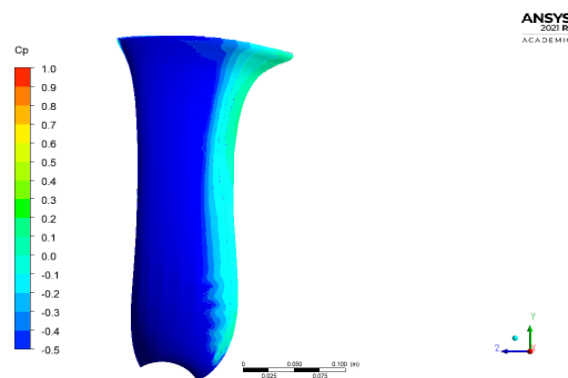
Table 4.9: C_p^{BEM} vs C_p^{CFX} at U_∞^{10}

C_p R 0.043 m
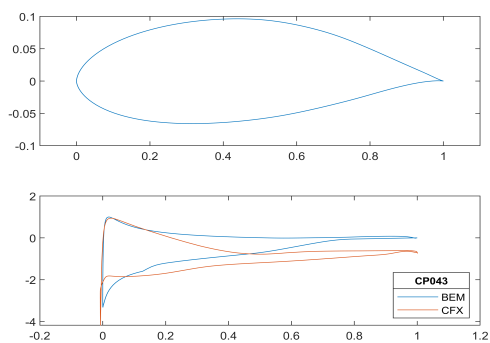
C_p R 0.129 m
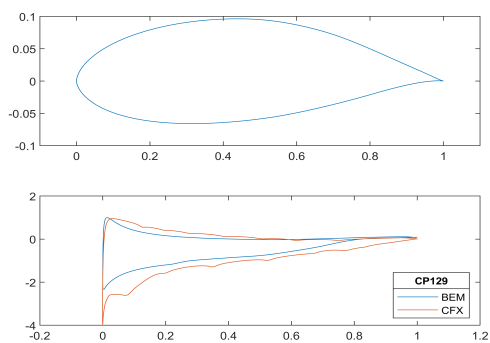
C_p R 0.293 m

C_p R 0.391 m
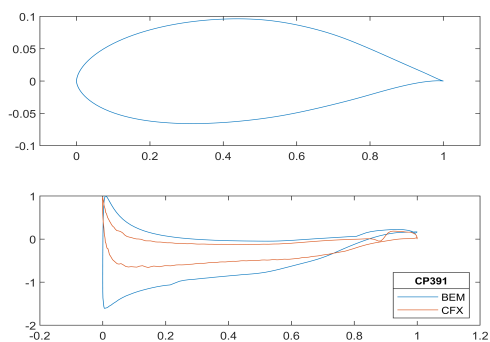
Table 4.10: C_p charts at R 0.201 m of U_∞^{10} at several U_∞

U_∞ 5 m/s
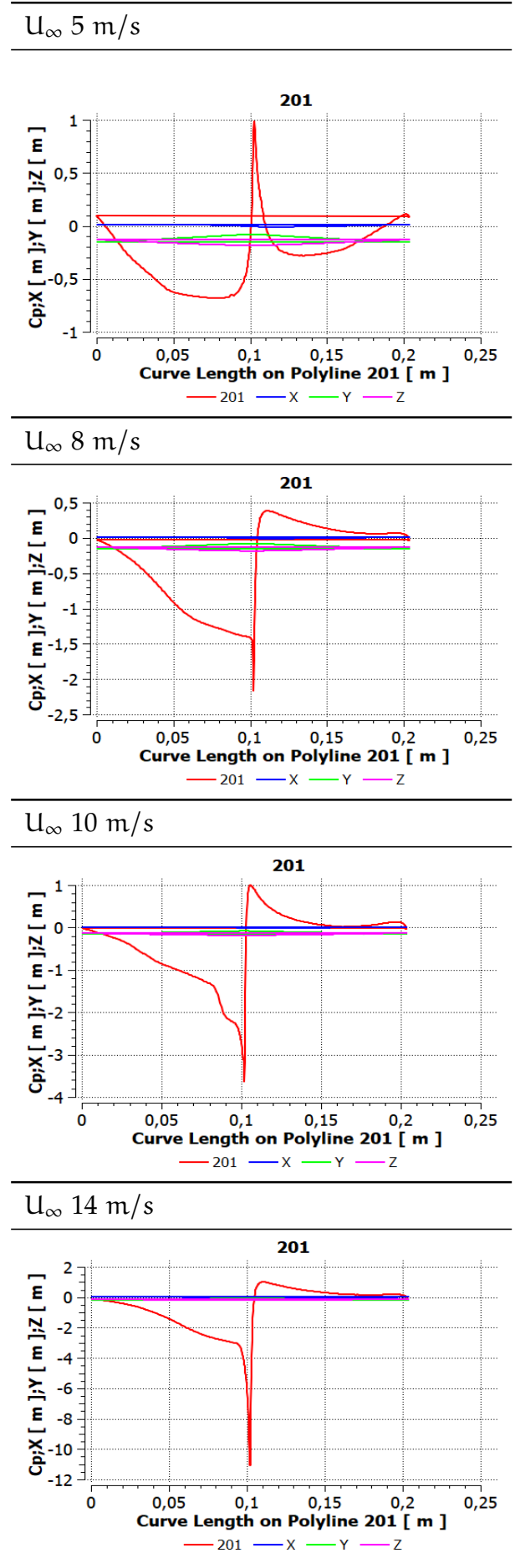
U_∞ 8 m/s

U_∞ 10 m/s

U_∞ 14 m/s

Table 4.11: C_p charts at R 0.384 m of U_∞^{10} at several U_∞

U_∞ 5 m/s
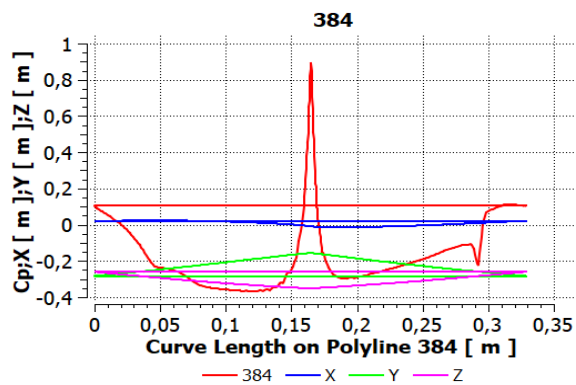
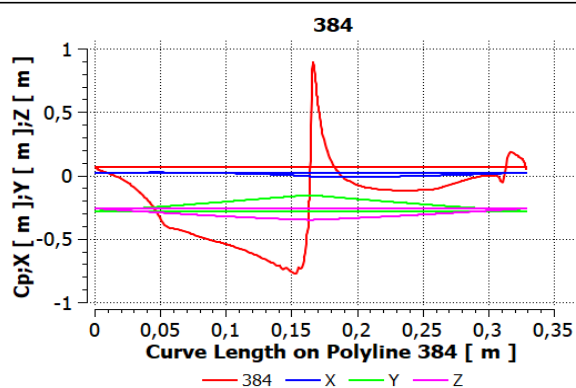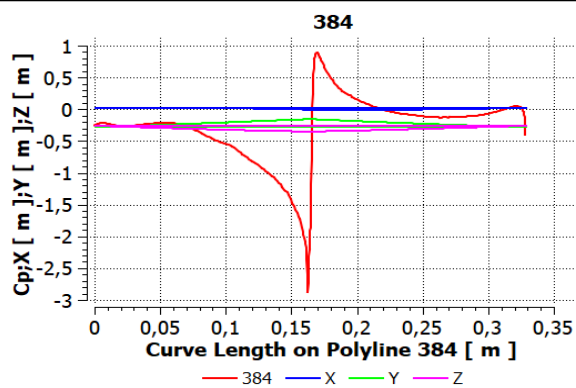| U_∞ 8 m/s |
| --- |
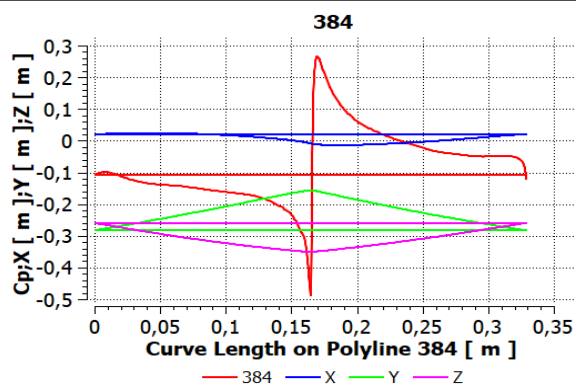
U_∞ 10 m/s

U_∞ 14 m/s

Chapter 5

Conclusions

The present work is subdivided into two main parts: the first theoretical, and the latter focused on operational project. Theoretically, a synthetic overview of the update development for optimising the design of a wind turbine, also in case of ducted support. It has been emphasised that the presence of the diffuser affects the induction factor a_d, that it is no longer radially constant as the back pressure gives a speed that reaches its maximum close to the tip. In addition, the factor is crucial to determine the Glauert's correction. Therefore, every further analysis addressed to obtain a function between the back pressure beyond the rotor and speed up γ is a good step towards a DAWT design optimisation. Indeed, the aim to this thesis about the chord distribution for DAWTs is to demonstrate that the research of the optimum chord length means simultaneously a research of the variation of wind profile, that flows undisturbed up to cross the diffuser. After that, a chaotic motion is developed and that has to be taken into account during the design procedure. So far, the design procedure for a DAWT has been made by choosing an already projected blade and coupled with a diffuser. Instead of, in the second part of the thesis, the operational one, the CFD analysis of two different DAWT blade profiles, generated by GUI BEM software with an integrated and distinct design have been compared. The figures have shown that the integrated design overperforms the distinct. Additionally, the integrated design is also more close to commercial micro wind turbines, presented as a benchmark. This aspect shows an other advantage of ducted turbine respect the comparable bare solution: they are able to provide the same amount of energy together with a size reduction.

The remaing open question, that could be a starting point for further research, regards the development of an algorithm able to taking into account the radial variation of induction factor. In the CFD sphere, it might be worthwhile to pay attention for repeating the design procedure to individuate a design velocity able to approximate the effective wind profile inside the diffuser better than $10 \, m/s$ and therefore suggests an improvement of chord length distribution.

Bibliography

Agha, A., H. N. Chaudhry, and F. Wang, 2018: Diffuser augmented wind turbine (dawt) technologies: A review. *undefined*.

Bak, C., 2013: *Aerodynamic design of wind turbine rotors*. Elsevier, doi:10.1533/9780857097286.1.59.

Batu, T. and H. G. Lemu, 2020: *Comparative Study of the Effect of Chord Length Computation Methods in Design of Wind Turbine Blade*, Vol. 634 LNEE. Springer, 106-115 pp., doi:10.1007/978-981-15-2341-0_14.

Betz, A., 1926: *Wind-Energie und ihre Ausnutzung durch Windmühlen*. Vandenhoeck u. Ruprecht.

Branlard, E., 2017: Wind turbine aerodynamics and vorticity-based methods. doi:10.1007/978-3-319-55164-7, URL http://www.springer.com/gp/book/9783319551630.

Burton, T., N. Jenkins, D. Sharpe, and E. Bossanyi, 2011: *Wind Energy Handbook*. John Wiley & Sons, Ltd, doi:10.1002/9781119992714.

Bussel, G., 1999: *An assessment of the performance of diffuser augmented wind turbines (DAWT's)*, 1–. ASME FED, American Society of Mechanical Engineers, United States, 1999 ASME Fluids Engineering Division Summer Meeting (FEDSM 1999), FEDSM '99 ; Conference date: 18-07-1999 Through 23-07-1999.

Bussel, G., 2007: The science of making more torque from wind: Diffuser experiments and theory revisited. *Journal of Physics: Conference Series*, **75**, 012 010, doi:10.1088/1742-6596/75/1/012010.

Drzewiecki, S., 1892: *Sur une méthode pour la détermination des éléments mécaniques des propulseurs hélicoïdaux*. Association technique maritime.

Duran, S., 2005: Computer-aided design of horizontal-axis wind turbine blades a thesis submitted to the graduate school of natural and applied sciences of middle east technical university.

Edon, M., 2007: Meter wind turbine blade design.

Fasullo, J. T. and K. E. Trenberth, 2008: The annual cycle of the energy budget. part ii: Meridional structures and poleward transports. *Journal of Climate*, **21**, 2313–2325, doi:10.1175/2007JCLI1936.1, URL https://journals.ametsoc.org/view/journals/clim/21/10/2007jcli1936.1.xml.

Fletcher, C. A., 1981: Computational analysis of diffuser-augmented wind turbines. *Energy Conversion and Management*, **21**, 175–183, doi:10.1016/0196-8904(81)90012-1.

Froude, W., 1878: On the mechanical principles of the action of propellers. *Trans. Inst. Nav. Archit.*, **19**.

Glauert, H., 1926: *The analysis of experimental results in the windmill brake and vortex ring states of an airscrew*. HMSO.

Glauert, H., 1935: *Airplane Propellers*, 169–360. Springer Berlin Heidelberg, Berlin, Heidelberg, doi:10.1007/978-3-642-91487-4_3.

Glauert, H., 1983: The elements of aerofoil and airscrew theory. *The Elements of Aerofoil and Airscrew Theory*, doi:10.1017/CBO9780511574481.

Goldstein, S., 1969: Fluid mechanics in the first half of this century. *Annual Review of Fluid Mechanics*, **1 (1)**, 1–29, doi:10.1146/annurev.fl.01.010169.000245.

Gundtoft, S., 2009: Wind turbines.

Hansen, M., 2008: *Aerodynamics of Wind Turbines: second edition*. 2d ed., Earthscan.

Hansen, M. O. L., N. N. Sørensen, and R. G. J. Flay, 2000: Effect of placing a diffuser around a wind turbine. *Wind Energy*, **3**, 207–213, doi:10.1002/WE.37.

Hau, E., 2013: *Wind Turbines*. Springer Berlin Heidelberg, doi:10.1007/978-3-642-27151-9.

Holtslag, M., 2016: Far offshore wind conditions in scope of wind energy. Ph.D. thesis, Delft University of Technology, doi:10.4233/uuid:3c66f401-6cff-4273-aa49-df4274ba767f.

Ingram, G., 2011: Wind turbine blade analysis using the blade element momentum method. version 1.1.

Jamieson, P., 2008: Generalized limits for energy extraction in a linear constant velocity flow field. *Wind Energy*, **11**, 445–457, doi:10.1002/WE.268.

Jamieson, P., 2011: Innovation in wind turbine design. *Innovation in Wind Turbine Design*, doi:10.1002/9781119975441, URL https://onlinelibrary.wiley.com/doi/book/10.1002/9781119975441.

Kulunk, E., 2011: *Aerodynamics of Wind Turbines*. InTech, doi:10.5772/17854.

Liu, Y. and S. Yoshida, 2015: An extension of the generalized actuator disc theory for aerodynamic analysis of the diffuser-augmented wind turbines. doi:10.1016/j.energy.2015.09.114, URL http://dx.doi.org/10.1016/j.energy.2015.09.114.

Maalawi, K. Y. and M. T. S. Badawy, 2001: A direct method for evaluating performance of horizontal axis wind turbines. *Renewable and Sustainable Energy Reviews*, **5**, 175–190.

Manwell, J. F., J. G. McGowan, and A. L. Rogers, 2009: *Wind Energy Explained*. John Wiley & Sons, Ltd, doi:10.1002/9781119994367.

Markowski, P. and Y. Richardson, 2010: *Mesoscale Meteorology in Midlatitudes*. John Wiley & Sons, Ltd, doi:https://doi.org/10.1002/9780470682104.fmatter, https://onlinelibrary.wiley.com/doi/pdf/10.1002/9780470682104.fmatter.

Marshall, J. and R. A. Plumb, 2008: *Atmosphere, Ocean, and climate dynamics:an introductory text.* Elviser Academic Press.

McCosker, J., 2012: Design and optimization of a small wind turbine.

Ohya, Y. and T. Karasudani, 2010: A shrouded wind turbine generating high output power with wind-lens technology. *Energies*, **3 (4)**, 634–649, doi:10.3390/en3040634, URL https://www.mdpi.com/1996-1073/3/4/634.

Okda, Y. M. E., 2015: Design methods of horizontal axis wind turbine rotor blades. *International Journal of Industrial Electronics and Drives*, **2**, 135, doi:10.1504/IJIED.2015.072789.

Pavesi, G., 2013: *Wind Energy System. Notes for Students*.

Presz, W. M. J. and M. J. Werle, 2009: *Wind turbine with mixers and ejectors.* US20090087308A2.

Raju, S., 2011: Design optimization of a wind turbine blade.

Schaarup, J. and T. Krogh, 2001: Guide lines for design of wind turbines.

Schubel, P. J. and R. J. Crossley, 2012: Wind turbine blade design. **5**, 3425–3449, doi:10.3390/en5093425, URL www.mdpi.com/journal/energies.

Spera, D. A., 2009: *Wind Turbine Technology: Fundamental Concepts in Wind Turbine Engineering, Second Edition*. ASME Press, doi:10.1115/1.802601, URL https://doi.org/10.1115/1.802601.

Sørensen, J. N., 2016: *General Momentum Theory for Horizontal Axis Wind Turbines*, Vol. 4. Springer International Publishing, doi:10.1007/978-3-319-22114-4.

Tavares Dias do Rio Vaz, D. A., A. L. Amarante Mesquita, J. R. Pinheiro Vaz, C. J. Cavalcante Blanco, and J. T. Pinho, 2014: An extension of the blade element momentum method applied to diffuser augmented wind turbines. *Energy Conversion and Management*, **87**, 1116–1123, doi:https://doi.org/10.1016/j.enconman.2014.03.064, URL https://www.sciencedirect.com/science/article/pii/S0196890414002659.

Vaz, J. R. and D. H. Wood, 2016: Aerodynamic optimization of the blades of diffuser-augmented wind turbines. *Energy Conversion and Management*, **123**, 35–45, doi:10.1016/J.ENCONMAN.2016.06.015, URL http://dx.doi.org/10.1016/j.enconman.2016.06.015.

Wald, Q. R., 2006: The aerodynamics of propellers. *Progress in Aerospace Sciences*, **42**, 85–128, doi:10.1016/J.PAEROSCI.2006.04.001.

Wang, T., 2012: A brief review on wind turbine aerodynamics. *Theoretical and Applied Mechanics Letters*, **2**, 062 001, doi:10.1063/2.1206201.

Wood, D. H., 2015: Maximum wind turbine performance at low tip speed ratio. *Journal of Renewable and Sustainable Energy*, **7**, 053 126, doi:10.1063/1.4934805, URL https://aip.scitation.org/doi/abs/10.1063/1.4934805.

Acknowledgments

Innazitutto desidero rigraziare il Prof. Pavesi come relatore per il benevolo aiuto nello sviluppo della tesi e per avermi trasmesso la passione nelle turbine eoliche.

Nessun lavoro tesistico dovrebbe essere considerato come la propria torre d'avorio, ma ha valore solo se diventa anche un frammento di vita condiviso con gli altri.

In particolar modo, ringrazio:

- *Marco Mosti* perchè con sincera amicizia ci si intende al primo sguardo fin dai tempi del Liceo.
- *Stefano Campogrande* per la stima e la fiducia sempre ricambiati.
- *Sara Sanseverinati* perchè è la migliore e più rassicurante organizzatrice che io conosca, ma soprattutto per la sua amicizia, che non viene meno neanche a grande distanza.
- *Giulia Segatto* perchè mi ha ricordato che troppo spesso ci dimentichiamo di ricercare la bellezza nel mentre si vive; infatti, alla fine 'la bellezza salvarà il mondo' (Dostoevskij, l'idiota).
- *Ilaria Montanari* per le risate in amicizie e, detto tra noi, per avermi fatto leggere in anteprima i suoi promettenti romanzi gialli.
- *Irene Ceretti* perchè è una amicizia profonda e sentita.
- *Alessandro ed Eleonora* perchè sia come archeologi che come amici sono una coppia fantastica, a parte quando si coalizzano a *Bang!*

Senza voler far dimenticanza a nessuno, ricordo tutti gli altri amici con cui ho condiviso gioe e dolori di questo lungo viaggio.

Impossibile non voler bene alle Associazioni che mi hanno arrichito di compagnia e sorrisi in questi anni:

- *METIS VELA* per essere stati dei veri amici nel far assaporare la passione per la vela e per gli airfoils.
- *LEDS* perchè alzano il livello della vita universitaria padovana ed... anche il gomito!
- *ELIES* perchè ha aperto a nuovi orizzonti e conoscenze.

- *EYEN* perchè la culla di tutti i grandi progetti è un gruppo di amici.

Infine, ringrazio la mia famiglia e tutti gli amici di famiglia che mi sono sempre stati vicini.